

First image-guided treatment of a mouse tumor with radioactive ion beams

Daria Boscolo^{1,§}, Giulio Lovatti^{2,§}, Olga Sokol^{1,§}, Tamara Vitacchio¹, Francesco Evangelista², Emma Haettner¹, Walter Tinganelli¹, Christian Graeff^{1,3}, Uli Weber^{1,4}, Christoph Schuy¹, Munetaka Nitta², Martina Moglioni¹, Daria Kostyleva¹, Sivaji Purushothaman¹, Peter G. Thirolf², Jonathan Bortfeldt², Christoph Scheidenberger^{1,5,6}, Katia Parodi^{2,#} and Marco Durante^{1,7,8,#,*}

1. GSI Helmholtzzentrum für Schwerionenforschung, Darmstadt, Germany
2. Department of Medical Physics, Ludwig-Maximilians-Universität München (LMU), Munich, Germany.
3. Department of Electrical Engineering and Information Technology (ETIT), Technische Universität Darmstadt, Darmstadt, Germany
4. Life Science Engineering Faculty, Technische Hochschule Mittelhessen, Gießen, Germany
5. Institute of Physics, Justus-Liebig-Universität Gießen, Gießen, Germany
6. Helmholtz Research Academy Hesse for FAIR (HFHF), GSI Helmholtz Center for Heavy Ion Research, Campus Giessen, 35392 Giessen, Germany
7. Institute of Condensed Matter Physics, Technische Universität Darmstadt, Darmstadt, Germany
8. Department of Physics „Ettore Pancini“, University Federico II, Naples, Italy

§: these authors contributed equally

#: these authors contributed equally

*Corresponding author: m.durante@gsi.de

Abstract

Radioactive ion beams (RIB) are a key focus of current research in nuclear physics. Already long ago it was proposed that they could have applications in cancer therapy. In fact, while charged particle therapy is potentially the most effective radiotherapy technique available, it is highly susceptible to uncertainties in the beam range. RIB are well-suited for image-guided particle therapy, as isotopes that undergo β^+ -decay can be precisely visualized using positron emission tomography (PET), enabling accurate real-time monitoring of the beam range. We successfully treated a mouse osteosarcoma using a radioactive ^{11}C -ion beam. The tumor was located in the neck, in close proximity to the spinal cord, increasing the risk of radiation-induced myelopathy from even slight variations in the beam range caused by anatomical changes or incorrect calibration of the planning CT. We managed to completely control the tumor with the highest dose while minimizing toxicity. Low-grade neurological side effects were correlated to the positron activity measured in the spine. The biological washout of the activity from the tumor volume was dependent on the dose, indicating a potential component of vascular damage at high doses. This experiment marks the first instance of tumor treatment using RIB and paves the way for future clinical applications.

Main

Nuclear physics methods have been instrumental in improving cancer radiotherapy using accelerated charged particles (protons or heavier ions). Charged nuclei have indeed a favorable depth-dose distribution in the human body thanks to the Bragg peak¹. Therapy with accelerated ¹²C-ions is currently ongoing in fourteen centers worldwide² and, even if more expensive than proton therapy, adds biological advantages to the physical benefit of the Bragg peak³. Particle therapy is, however, much more sensitive to uncertainties in the beam range than conventional X-rays, exactly because of the high dose deposited in the Bragg peak⁴. Several techniques are available to monitor the beam range exploiting the nuclear interactions of the ions in the tissue⁵, including PET⁶. PET in carbon ion therapy exploits β^+ -emitting isotopes ¹¹C and ¹⁰C produced by the nuclear fragmentation of the therapeutic stable ¹²C beam in the patient's body. The method was extensively tested during the carbon ion therapy pilot trial at GSI in Darmstadt⁷, then at HIT in Heidelberg⁸ and more recently at CNAO in Pavia⁹. However, the counting rate from projectile fragments is low, the activity peak is largely shifted with respect to the Bragg peak because the particle range of the isotopic fragments of ¹²C depends on their mass, and the image analysis has been mainly performed off-line. Therefore, PET in ¹²C-ion therapy remains marginal and is not really able to reduce the range uncertainty as desired.

Most of these problems can be overcome using RIB rather than stable beams for therapy. RIB are generally acknowledged as the main tool to address the most important modern questions in nuclear physics, as they allow the study of nuclei at extreme conditions¹⁰⁻¹². In cancer radiotherapy, RIB have the same biological effectiveness of the corresponding stable ions beams^{13,14} but can increase the PET signal/noise ratio by approximately an order of magnitude, reduce the shift between the activity and dose peaks, and mitigate the washout image blur with short-lived isotopes (e.g. ¹⁰C) and in-beam acquisition^{15,16}. The reduced uncertainty in range allows a shrinkage of the tumor margins around the clinical target volume (CTV), and this can lower toxicity for both serial or parallel organs-at-risk (OAR)¹⁷. Attempts to use RIB in cancer therapy started already in the 80s during the heavy ion therapy pilot project at the Lawrence Berkeley Laboratory (CA, USA)¹⁸, but they were always hampered by the low intensities of the secondary beams produced by fragmentation of the primary ions used for therapy (for an historical review see ref.¹⁹). Research at modern high-intensity accelerators that can produce RIB with intensity sufficient for therapeutic treatments²⁰ would pave the way to PET-guided heavy ion treatments. One of these facilities is GSI/FAIR in Darmstadt (Germany)²¹, where we started the BARB (Biomedical Applications of Radioactive Ion Beams) project whose goal was to perform the first in vivo tumor treatment with RIB¹⁵.

Within BARB, we have already reported the RIB imaging resolution in phantoms^{22,23} and transported the beam from the fragment separator (FRS) to the medical vault (Cave M, where animal experiments are possible) at the GSI accelerator facility²⁴ ([Extended Data Fig. 1](#)). In Cave M we have then enabled the reproducible installation of the portable small-animal SIRMIO in-beam PET scanner²⁵, built by the Ludwig-Maximilian-University (LMU) group in Munich for in vivo range verification in pre-clinical particle therapy experiments. The SIRMIO PET scanner is based on 56 scintillator blocks of pixelated LYSO crystals. The

crystals are arranged providing a pyramidal-step shape to optimize the geometrical coverage in a spherical configuration²⁶. Inside the detector it is possible to accommodate an anesthetized mouse in vertical position using a custom 3D-printed holder for simultaneous irradiation and real-time PET imaging, also developed at LMU. The mouse model used in this study is a syngeneic LM8 osteosarcoma implanted in the C3H mouse neck²⁷. Osteosarcoma is a very radioresistant tumor²⁸ and for this reason it is a typical candidate for treatment with accelerated ¹²C-ions²⁹. Fig. 1A shows μ CT images of the tumor growth and the actual visible tumor in the neck. In Fig. 1B we show the contouring of the individual gross tumor volumes (GTV) of the different mice used in the experiments. By summing up all the tumor profiles and smoothing the resulting outline, we have contoured a universal CTV applied to all mice in this study. The proximity of the CTV to the spinal cord makes high precision and online guidance necessary to avoid radiation myelopathy³⁰. Measured endpoints were tumor growth, spinal cord toxicity, and washout rate of the radioactive signal from the tumor. We elected to use ¹¹C projectile even if our previous experiments^{22,23} show that the highest range resolving power can be achieved with short-lived isotopes such as ¹⁰C or ¹⁵O. We preferred to use carbon, which is already used in many clinical facilities, rather than oxygen, and the intensity of *N*-2 isotopes such as ¹⁰C is too low for very high-dose single-fraction treatment. The goal of the experiment was to demonstrate for the first time the ability to use a ¹¹C-ion radioactive beam to achieve full tumor control of a radioresistant tumor, such as osteosarcoma, proximal to an OAR, while maintaining low toxicity thanks to real-time PET image guidance.

The BARB beamline

Fig. 2 shows the full BARB beamline prepared in Cave M at GSI and photographs of different components. The secondary beam of ¹¹C comes from the FRS³¹ (Extended Data Fig. 1). The primary intensity of the ¹²C-ion beam in the SIS18 at 300 MeV/u was $1.6 \cdot 10^{10}$ particles/spill and the intensity of ¹¹C-ions in Cave M entrance was $2.5 \cdot 10^6$ particles/spill. To allow a longer online PET acquisition time, we used a short spill duration of 200 ms and a relatively low duty cycle with a repetition rate of 3 s (see Extended Data Table 1 for a summary of all the parameters).

Measured pristine ¹¹C-ion Bragg curve is shown in Extended Data Fig. 2. To cover the full CTV, the pristine Bragg peak has to be extended to produce a Spread-Out-Bragg-Peak (SOBP). The measured SOBP is shown in Extended Data Fig. 3. The SOBP was formed by a 3D-printed range modulator (Extended Data Fig. 4A) from a 2D scan of the monoenergetic pencil beam.

The distal field contour was modulated to the tumour CTV (Fig. 1B) by a 3D-printed plastic compensator collar (Extended Data Fig. 4B). We measured a dose-rate around 1 Gy/min in the tumor that was covered by the SOBP at the same dose. A total of 32 mice were irradiated with either 20 or 5 Gy.

Activity maps

In BARB we use real-time PET imaging to monitor the RIB dose delivery. A FLUKA³² Monte Carlo simulation of the beam reaching the tumor inside the SIRMIO PET scanner is

shown in [Fig. 3 A-B](#) along with the activity distribution image measured online ([Fig. 3C](#)) with ^{11}C -ions by the PET scanner and overlaid on the μCT scan of the animal under irradiation. Measured activity and calculated positron annihilation profiles, integrated along the x-axis and displayed along the beam direction (z-axis), are shown in [Fig. 3D](#) along with the 1D dose profile in the z-direction. Even if the dose and the activity are deposited by the same ion in this experiment, the ^{11}C beam momentum spread shifts the activity beyond the dose fall-off. A shift of approximately 2 mm is observed between the measured activity and simulated positron annihilation map peaks, with measured values closer to the actual dose fall-off. The depth at 80% dose fall-off matches the simulated activity peak. [Supplementary video 1](#) shows the build-up of the measured PET signal vs. irradiation time in sagittal and transversal views. Individual images of all mice are shown in [Supplementary Fig. 1](#). The tumour is very close to the spinal cord, and in-beam PET image was used to check that the SOPB was not covering the spine. For all animals ([Supplementary Fig. 1](#)) the peak activity was not inside or beyond the spinal cord, so no range correction by adjusting the degrader thickness ([Fig. 2](#)) had to be applied.

Tumor control

Tumor sizes of irradiated and control tumor-bearing animals were measured for four weeks after the day of irradiation using caliper or μCT . Results shown in [Fig. 4](#) demonstrate complete tumor control after 20 Gy and prolonged tumor growth delay after 5 Gy, with evidence of recurrence after 2 weeks. Full tumor control was also achieved with 20 Gy X-rays ([Extended Data Fig. 5](#)). The data are compatible with a complete coverage of the tumor target for all animals. Recurrence at the lower dose is expected considering the high radioresistance of the osteosarcoma.

Toxicity

Skin toxicity scoring in the tumor-bearing controls was complicated by the growth of the tumor that caused superficial lesions. In irradiated animals, all of them bearing small tumors post-irradiation, skin toxicity was radiation-induced as shown in [Extended Data Fig. 6](#). No animals showed skin toxicity grade > 3.

Being the tumor very close to the cervical area of the spinal cord, main expected toxicity was radiation-induced myelopathy. However, none of the animals exposed to ^{11}C -ions presented severe morbidity such as forelimb paralysis or pronounced kyphosis. [Extended Data Fig. 5](#) and [Supplementary video 2](#) show the toxicity after X-rays, which is much more severe than for ^{11}C -ions. Animals suffered severe weight loss due to impaired feeding, ostensibly caused by damage to the esophagus, and grade 3 kyphosis, caused by cervical myelopathy as expected from previous experiments³⁰. This toxicity is related to the X-ray dose that, unavoidably, was received by the organs behind the tumor in the neck region.

For animals exposed to ^{11}C -ions, the lack of severe toxicity demonstrate that online PET measurement ([Fig. 3](#)) correctly predicted the position of the SOPB. However, since the tumor is close to the spine, some activity was inevitably observed in the spinal cord, corresponding to the dose fall-off ([Fig. 3](#)). We checked the impact of this residual dose on low-grade toxicity by measuring grip strength performance, a common test to assess cervical spinal

injury³³ (Extended Data Fig. 7). All results of the bi-weekly grip strength performance for individual mice are reported in Supplementary Fig. 2. A wide inter-individual variability is noted in those curves. However, by pooling the data in Fig. 5A-B we show that the strength of the mice is reduced after irradiation compared to controls, indicative of a minor deficit in neuromuscular function. Correlation of integral PET counts in the spine with individual grip performance is shown in Fig. 5C-D. Despite the wide scatter in the grip test data, there is a significant correlation between activity in the spine and decreased mouse forelimb strength. We therefore clearly demonstrated that the beam online visualization allowed sparing of the OAR and strongly reduced toxicity compared to X-rays.

Washout

The activity in a plastic target decreases after irradiation because of the physical decay of the ¹¹C (T_{1/2}=20.34 min) projectile and nuclear fragments (¹⁰C, T_{1/2}=19.3 s; ¹⁵O, T_{1/2}=2.04 min). We have previously modelled the radioactive decay with exponential functions that include all fragments produced²³. In this experiment, the radioactive decay is overlapped with an unknown biological decay due to the blood flow in the tumor that removes the radioactive isotopes from the site of decay. The degree of vascularization in our tumor model was estimated by perfusion to opacify microvasculature structure in μ CT. Supplementary video 3 shows that our osteosarcoma in the neck is highly vascularized, so a strong biological washout is expected. The total washout data for all animals are reported in Supplementary Fig. 3. Studies in Japan in a rat glioma model point to a double-exponential model for the biological washout³⁴, which was also applicable to our data based on the results of the Fisher's test on fitting parameters. We therefore used the following equation to fit the activity data measured after the irradiation was stopped:

$$A(t) = A_{phys} \cdot A_{bio} = A_0 \sum_i w_i e^{-\frac{\ln 2}{T_{1/2i}} t} \cdot [W_s e^{-k_s t} + (1 - W_s) e^{-k_f t}]$$

where A_0 is the activity at the end of the irradiation, W_s - the relative weight of the slow component, and k_s and k_f are the slow and fast time constants, respectively. $T_{1/2i}$ is the half-life of the i -th contributing radioisotope and w_i is its fraction in the total number of fragments. Based on the FLUKA simulation, we have considered 96% ¹¹C, 3% ¹⁰C, and 0.5% ¹⁵O ions. Fig. 6 shows the pooled analysis of the animals exposed to 5 or 20 Gy (individual curves are reported in Supplementary Fig. 3). The results clearly show a significant difference between the low- and high-dose experiments. The fast component, very well visible at 5 Gy, essentially disappears at 20 Gy. This suggests a quick vascular injury at high doses that delays the washout process in the first half an hour after the irradiation.

Discussion

The goal of the BARB project was to provide a first demonstration of tumor treatment with RIB with real-time range verification by PET. The results in Fig. 4 are in fact the first example of successful tumor control with RIB. We used a very high dose of 20 Gy in a single fraction, expecting tumor control based on our own previous X-ray experiment in the same murine osteosarcoma model. However, while X-rays caused severe toxicity at that dose

(Extended data Fig. 5, Supplementary video 2), this was not the case with ^{11}C -ions, where we observed minor toxicity only, correlated to the residual activity measured in the spine (Fig. 5). Therefore, we conclude that image-guided particle therapy with RIB is feasible, safe and effective.

The results on washout (Fig. 6) are intriguing and deserve further experiments. One of the main tenets of radiotherapy is that tumor control can only be achieved when all cancer stem cells are killed³⁵. However, already 20 years ago, it has been shown that at high doses microvascular endothelial apoptosis can contribute to tumor sterilization³⁶. Later studies showed that the tumor damage at high doses induce vascular damage³⁷ and can be mediated by an ischemic-reperfusion mechanism³⁸. This idea has been already translated in clinics with the single-dose radiotherapy (SDRT)³⁹, that uses single fractions of 24 Gy rather than fractionation in small malignancies, achieving excellent clinical results⁴⁰. However, the concept is controversial. In fact, according to the classical linear-quadratic model, single fractions are much more effective than fractionated doses, and therefore the benefits of SDRT may simply be attributed to the high biological effectiveness of single doses^{41,42}. The available experimental data are not conclusive⁴³. Dynamic contrast-enhanced MRI in rats shows increased permeability after high doses of X-rays or C-ions⁴⁴, but those studies look at the effects weeks after irradiation, whereas our results cover the initial 30 minutes after exposure. This time frame is crucial, as other studies reported ischemic stress following SDRT within a few minutes³⁸ or hours⁴⁵. Biological washout provides a direct measurement of the vascular perfusion in tumor, and therefore we believe that this technique can clarify the vascular engagement after radiotherapy. Our results are consistent with an ischemic stress occurring very early after high doses. Although reperfusion was not observed within the measured time interval, we cannot rule out the possibility that it may occur at a later time.

Outlook

What are the next preclinical steps in RIB research? We will test short-lived isotopes such as ^{10}C or ^{15}O , which are expected to provide a higher PET imaging resolution. For ^{10}C , it will be necessary to use the new Super-FRS⁴⁶ at FAIR, which will be able to provide much higher intensities of secondary beams.

One issue to be solved is the shift between physical dose and activity that is significant even with RIB because of the momentum spread (Fig. 3D). The dependence of the shift from the momentum acceptance had been previously observed in PMMA phantoms⁴⁷ and our simulations confirm previous calculations suggesting that the simulated activity peak predicts the position of the 80% Bragg peak fall-off⁴⁸. However, our measured activity is also shifted compared to simulations (Fig. 3D). The rationale of real-time image-guidance is indeed that there are unavoidable uncertainties in the actual mouse position, anatomy and composition deduced from a pre-treatment μCT , and these uncertainties are not predicted by the Monte Carlo simulation but are visible in the measurement. For instance, μCT was acquired with mice in horizontal position in the SIRMIO PET holder, while irradiation was always performed with mice in vertical position (Fig. 2). In addition, the discrepancies may arise from the omission of specific detector details in the simulation, which only approximates the activity with the

positron annihilation distribution and a 1-mm Gaussian filter. A machine learning algorithm is in preparation to allow online transformation of the image and the profile from activity to dose, so that an online dose-map can be displayed.

For the washout studies, future experiments should investigate a wider range of doses and extended post irradiation time-points, alongside tumor histology to better assess vascular changes following irradiation.

Can these successful results lead to a clinical translation of RIB? The MEDICIS-Promed^{49,50} project at CERN proposed an ISOL production of a ¹¹C beam that can then be injected directly into medical synchrotrons currently used for ¹²C-ion therapy. Moving the isotope production to the low-energy injecting area can indeed be an excellent cost-saving solution where RIB can be used at least for an initial test of the range before a full treatment course. The Open-PET scanner⁵¹ developed at QST in Japan or the INSIDE in-beam PET^{9,52} installed at CNAO can be excellent detectors for clinical applications of RIB. Finally, washout can also have an important prognostic value in the clinics as it should be correlated to the tumor vasculature state and eventually to the level of hypoxia, a notorious negative prognostic factor in therapy^{34,53}. Our preclinical results show for the first time the feasibility of RIB radiotherapy and support these ongoing efforts for clinical translation.

Methods

RIB production

The ^{11}C beam was produced via in-flight separation. A 300 MeV/n ^{12}C primary beam from the SIS18 synchrotron impinges on a 8.045 g/cm² thick beryllium target at the FRS³¹ and undergoes peripheral nuclear reactions, so that one or more nucleons are stripped-off, leading to a variety of lighter isotopes from carbon and other elements from boron down to hydrogen. Via a combined magnetic rigidity analysis and energy loss, which is induced in a so-called wedge-shaped degrader that is located at the central focal plane of the fragment separator, an isotopic clean ^{11}C beam is achieved. This beam was used at the FRS for a variety of basic nuclear and atomic physics studies (such as reaction cross sections of the ^{11}C ions, their range and range straggling, basic PET studies etc.)^{22,23,54} in preparation of the present experiment. Via the connecting beamline to the target hall²⁴, the isotopic clean beam is transported to the Cave M, where the present irradiation has been accomplished. The FRS and its three branches are shown in [Extended Data Fig. 1](#) and exact parameters of the beam used in the present experiments are reported in [Extended Data Table 1](#).

Dosimetry

The ^{11}C beam from the FRS reached the experimental room with an intensity of $2.5 \cdot 10^6$ particles per spill. To minimize irradiation and allow for extended PET image acquisition, a beam cycle of 0.2 s ON and 3 s OFF was used. Once in the experimental room the beam was monitored with large parallel plate ionization chambers⁵⁵. The beam was characterized in terms of beam spot size and 1D and 3D depth dose distributions in water by means of a PTW Peakfinder and a water phantom equipped with an OCTAVIUS 1600 (PTW)⁵⁶. The latter setup allows to acquire 2D dose distributions at different water depth which can be processed to generate 3D dose maps distributions.

A range modulator was used to generate a 1.2 cm Spread-Out Bragg Peak (SOBP) in water. This modulator was 3D-printed on a 3D Systems ProJet MJP 2500 Plus using VisiJet M2S-HT250 as the printing material and VisiJet M2 SUP as the support material. The printing material has a water-equivalent density of 1.162 g/cm³ and a physical density of 1.1819 g/cm³.

The measured pristine and SOBP curves are shown in [Extended Data Figs. 2 and 3](#), respectively. The Bragg peak position in water for the pristine depth dose distribution was measured at 80.5 mm. By comparison with Monte Carlo simulation it was then possible to estimate beam parameters such as the beam energy and momentum spread. All measured and estimated beam parameters, also used for the Monte Carlo simulations, are reported in the [Extended Data Table 1](#).

A system of modulator, degraders, collimator and compensator was then used to passively modulate and optimize the beam for the animal irradiation. A schematic of the complete setup for mice irradiation is shown in [Fig. 2A](#). The SIRMIO PET scanner was mounted on the beamline with the isocenter aligned to the tumor's center. The initial beam energy is high to increase the efficiency of the FRS but has to be reduced for a small-animal experiment. The

beam was indeed attenuated using a 28.37 mm thick aluminum degrader. Fine adjustments to the Bragg peak position were made using a range shifter equipped with polyethylene plates. Two large brass shielding elements were also included in the beam line to protect the SIRMIO detector from stray radiation damage. A brass collimator with a 15×12 mm elliptical aperture was used to shape the beam laterally. It was positioned as close as possible to the SIRMIO detector aperture to minimize lateral scattering effects. Finally, the distal part of the SOBPs was shaped to the tumor CTV using a specially designed compensator, which was placed around the neck of the mice and secured on the mice bed. These compensators, produced using the same technology as the range modulator, also served for immobilization and mice positioning. Dosimetry at the target position was conducted using a small volume pinpoint ionization chamber (PTW TM31023) placed inside a custom-designed holder, ensuring the sensitive volume of the detector matched the tumor depth.

Animal model

All experiments were performed using 11-12-week-old female C3H/He mice (Janvier Labs, France) according to German Federal Law under the approval of the Hessen Animal Ethics Committee (Project License DA17/2003). Mice were divided into five groups: 20 Gy ^{11}C irradiation (17 animals, followed up for 6 months after the irradiation); 20 Gy and 5 Gy ^{11}C irradiation followed by additional 30 minutes of PET signal acquisition (8 and 7 animals, respectively, followed up for four weeks after the irradiation); tumor-bearing sham-irradiated controls (11 animals, followed up for four weeks after the irradiation day); and tumor-free controls (8 animals, followed up for 6 months after the irradiation day). Mice were housed at GSI in a conventional animal facility (non-SPF) at 22°C, 12-hour light-dark cycle, with unrestricted access to water and a standard diet (Ssniff, Germany). Fourteen days before irradiation, 10^6 mouse Dunn osteosarcoma LM8 cells (originating from C3H/He mice, purchased from Riken BioResource Center, Japan) were injected in 20 μl of PBS buffer solution subcutaneously in the neck area of the mouse, above the cervical area of the spine. To maintain the consistency of injections, during the procedure animals were anaesthetized with 2% isoflurane, which was inhaled via a face mask. After two weeks, most tumors were palpable and measurable at least with the μCT .

μCT

To collect the data on the tumor growth, we performed μCT measurements with VivaCT 80 scanner (SCANCO Medical AG, Switzerland). To ensure the reproducible positioning of the mice as during the ^{11}C irradiation, we have used the custom-made bed imitating the geometry of the SIRMIO bed. Additionally, animals were immobilized using the compensator collar, so that the scans can be utilized for the later Monte Carlo calculations. During the scan, animals were anesthetized with isoflurane (3% for the induction, 1.5-2% for maintenance during the scan). Neck regions of 31 mm were scanned for approximately 5 minutes at tube voltage and current of 45 kVp and 177 μA , respectively, adding a 0.1 mm aluminum filter, acquiring 250 projections per 180° with 45 ms integration time. The resulting images had a voxel size of 97.1 μm . After the scan, animals were allowed to recover before being transferred to the original cage. The scans performed at 14 days after the tumor cells injection into the animals used to establish the tumor model were used to contour the generalized CTV for the treatment planning.

The contouring of the visible tumor mass was done manually with the 3D Slicer software⁵⁷ for every animal, then the individual GTV contours were added up and the final CTV segmentation was smoothed up and made symmetrical. The animals selected for ¹¹C irradiation were scanned one day before the irradiation (13 days after the tumor induction) and then scanned weekly during a month after the irradiation; the animals remaining after the 28-days timepoint were scanned monthly afterwards until the sacrifice timepoint.

Tumour vascularization

To assess the tumor vascularization, animals were sacrificed and perfused ex vivo with VascupaintTM contrast agent (yellow colloidal bismuth suspension, MediLumine, Canada). After allowing the compound to polymerize for 24 hours, tumors were extracted and scanned at a high resolution (10 micron) with the following scanner settings: tube voltage and current of 55 kVp and 145 μ A, respectively, 0.5 mm aluminum filter, 1500 projections per 180° with 600 ms integration time. The 3D reconstruction of the tumor vasculature was done using the scanner's built-in software 'Bone morphology' function following the approach of another study with a contrast agent⁵⁸.

X-ray experiment

The primary goal of the X-ray experiment was to assess tumour control and the toxicity of high doses of radiation to mouse skin and to the spinal cord. We used the in-house X-ray generator (Isovolt DS1, Seifert, Ahrensberg, Germany) operated at 250 kVp and 16 mA, with 7 mm beryllium, 1 mm aluminum, and 1 mm copper filtering. Animals were positioned inside an isoflurane-filled plastic container, directly under the 2 mm thick lid. The setup height was adjusted to the dose rate of 5 Gy/min at the tumor position, which was confirmed by the ionization chamber measurement (PTW, Freiburg, Germany). Brass collimators of 2.5 cm thickness with 1.5×1.2 cm oval openings were used to shield the animal bodies, only exposing the tumor-bearing neck areas. Five animals each were irradiated with 20 or 15 Gy.

Monte Carlo

An extensive FLUKA Monte Carlo simulation study was conducted to support both the experiment design and its data analysis. The simulations assisted in designing beamline components, including the 2D range modulator, collimator, and mouse compensator, and in developing shielding strategies to protect the SIRMIO PET scanner from radiation damage. As in our previous BARB dosimetry study FLUKA simulations were also used to verify dosimetry measurements and support beam model characterization⁵⁴.

Expected dose and positron annihilation maps inside the mice body were simulated by importing the μ CT scans with their original resolution in a voxel FLUKA geometry. We applied a Gaussian filter with a 1 mm standard deviation (σ) to the resulting images, reported in [Fig. 3A-B](#), and compared them with the measured PET images, in [Fig. 3C](#). For this purpose the full experimental setup was implemented into the FLUKA geometry. A customized USRMED routine was used to simulate the range modulator. Dose and positron annihilation map distributions were simulated on mice μ CTs, which were also used for PET image co-registration and irradiation planning ([Fig. 3A-B](#)). For greater accuracy, specific calibration,

including the mouse bed and compensator, was applied to all simulated μ CTs.

In-beam PET

A novel spherical, high resolution PET scanner developed at LMU in the framework of the SIRMIO project was used to measure the RIB implantation in-beam during irradiation. The SIRMIO PET scanner features 56 3-layer depth-of-interaction (DOI) detectors arranged in a spherical shape with an inner diameter of 72 mm. Each DOI PET detector consists of a LYSO scintillator block with a pixel size of 0.9 mm readout by an 8×8 SiPM array. A charge division circuit and a custom-made amplifier circuit board developed at National Institutes for Quantum Science and Technology (Chiba, Japan) are used to reduce the 64 signals from the SiPM array to 4 signals. The data are then acquired by a customized DAQ software using two R5560 digitizers (CAEN, Italy). In order to enable image-guided irradiation for the BARB project, the data acquisition and reconstruction software were tailored to stream out and reconstruct the list mode data with user-defined time intervals, set in this experiment to cycles of 60 seconds. This feature enables visualizing the reconstructed stopping position of the beam almost “real-time” during the irradiation, along with the monitoring of the irradiation build up and decay through a graphical user interface. For this specific on-the-fly application, the image reconstruction was based on an in-house developed ordered subset expectation maximization (*OSEM*) algorithm, with a reduced number of iterations and limited size of the field of view for the sake of computational speed during the experiment. However, the 3D activity maps and washout analyses used for the reported results were based on a more time-consuming 3D maximum likelihood expectation maximization (MLEM) with relevant corrections for sensitivity and random coincidences.

Tumor growth

Starting one week after the injection, tumor dimensions were measured with a caliper twice per week for 28 days after the irradiation. Assuming the ellipsoid shape of the tumor, the volume was calculated as

$$V = \frac{4}{3} \pi abc$$

where a and b are the measured length and width of the tumor, respectively, and c (depth) is assumed to be the average of a and b .

Toxicity assays

Skin toxicity scoring. The toxicity of the skin in the irradiated area was scored using a simplified grading system of the Gesellschaft für Versuchstierkunde (GV-SOLAS) guidelines, divided by five grades (0: no effect; 1: redness; 2: dry skin and desquamation; 3: closed, healing wound; 4: open wound, not healing; 5: necrosis). Grade 5 was never observed during the experiment, and the termination criteria was reached when the animals showed a grade 4 and did not heal after the application of a topical treatment (Bepanthen®, Bayer). The treatment healed successfully the animals with a grade 3 after irradiation.

Grip test. The grip test was performed to measure the strength of the animals' forelimbs after

irradiation. Animals were acclimatized to refined handling techniques to reduce stress and optimize the data collection. We used the Grip Strength Meter-47200 (Ugo Basile®) equipped with a T-bar. The animals were lifted by the tail and suspended over the bar, then lowered to reach a horizontal position and gently pulled back until the grasp was released. Upon release, the peak force (in newton) was recorded. To get consistent data and avoid habituation to the task, the first three measurements in which the animal successfully grabbed the bar with both forelimbs were recorded and averaged.

Kyphosis scoring. To score the overall appearance and health status of the animals, videos were recorded in a house-made setup consisting of a starting box, a transparent-walled corridor, and a loop structure at the end, where the animals could enter and go back to the corridor. The animals were observed for spontaneous walking, grooming behavior and posture during stationary and movement phases. To evaluate the kyphosis, we used the scoring system from Yerger *et al.*⁵⁹ where in grade 0 there is no persistent kyphosis and the mouse can always straighten the spine; 1: mild kyphosis exhibited during stationary phase, but the spine is straightened during locomotion; 2: persistent mild kyphosis even during movement, the spine cannot be straightened completely; 3: the kyphosis is always maintained and well pronounced.

References

1. Durante, M. & Paganetti, H. Nuclear physics in particle therapy : a review. *Reports Prog. Phys.* **79**, 096702 (2016).
2. PTCOG. Particle therapy facilities in operation. (2024). Available at: <https://www.ptcog.ch/>. (Accessed: 2nd September 2024)
3. Durante, M., Debus, J. & Loeffler, J. S. Physics and biomedical challenges of cancer therapy with accelerated heavy ions. *Nat. Rev. Phys.* **3**, 777–790 (2021).
4. Lomax, A. J. Myths and realities of range uncertainty. *Br. J. Radiol.* **93**, 20190582 (2020).
5. Parodi, K. & Polf, J. C. In vivo range verification in particle therapy. *Med. Phys.* **45**, e1036–e1050 (2018).
6. Parodi, K., Yamaya, T. & Moskal, P. Experience and new prospects of PET imaging for ion beam therapy monitoring. *Z. Med. Phys.* **33**, 22–34 (2023).
7. Enghardt, W. *et al.* Charged hadron tumour therapy monitoring by means of PET. *Nucl. Instruments Methods Phys. Res. Sect. A Accel. Spectrometers, Detect. Assoc. Equip.* **525**, 284–288 (2004).
8. Bauer, J. *et al.* Implementation and initial clinical experience of offline PET/CT-based verification of scanned carbon ion treatment. *Radiother. Oncol.* **107**, 218–226 (2013).
9. Kraan, A. C. *et al.* In-beam PET treatment monitoring of carbon therapy patients: Results of a clinical trial at CNAO. *Phys. Medica* **125**, 104493 (2024).
10. Jenkins, D. G. Recent advances in nuclear physics through on-line isotope separation. *Nat. Phys.* **10**, 909–913 (2014).
11. Blumenfeld, Y., Nilsson, T. & Van Duppen, P. Facilities and methods for radioactive ion beam production. *Phys. Scr.* **T152**, 014023 (2013).
12. Bertulani, C. A. & Gade, A. Nuclear astrophysics with radioactive beams. *Phys. Rep.* **485**, 195–259 (2010).
13. Chacon, A. *et al.* Experimental investigation of the characteristics of radioactive beams for heavy ion therapy. *Med. Phys.* **47**, 3123–3132 (2020).
14. Chacon, A. *et al.* Monte Carlo investigation of the characteristics of radioactive beams for heavy ion therapy. *Sci. Rep.* **9**, 6537 (2019).
15. Boscolo, D. *et al.* Radioactive Beams for Image-Guided Particle Therapy: The BARB Experiment at GSI. *Front. Oncol.* **11**, (2021).
16. Mohammadi, A. *et al.* Range verification of radioactive ion beams of ^{11}C and ^{15}O using in-beam PET imaging. *Phys. Med. Biol.* **64**, 145014 (2019).
17. Sokol, O. *et al.* Potential benefits of using radioactive ion beams for range margin reduction in carbon ion therapy. *Sci. Rep.* **12**, 21792 (2022).
18. Chatterjee, A., Alpen, E. L., Tobias, C. A., Llacer, J. & Alonso, J. High energy beams of radioactive nuclei and their biomedical applications. *Int. J. Radiat. Oncol.* **7**, 503–507 (1981).

19. Durante, M. & Parodi, K. Radioactive Beams in Particle Therapy: Past, Present, and Future. *Front. Phys.* **8**, 00326 (2020).
20. Durante, M., Golubev, A., Park, W.-Y. & Trautmann, C. Applied nuclear physics at the new high-energy particle accelerator facilities. *Phys. Rep.* **800**, 1–37 (2019).
21. Durante, M. *et al.* All the fun of the FAIR: fundamental physics at the facility for antiproton and ion research. *Phys. Scr.* **94**, 033001 (2019).
22. Kostyleva, D. *et al.* Precision of the PET activity range during irradiation with 10 C, 11 C, and 12 C beams. *Phys. Med. Biol.* **68**, 015003 (2023).
23. Purushothaman, S. *et al.* Quasi-real-time range monitoring by in-beam PET: a case for 15O. *Sci. Rep.* **13**, 18788 (2023).
24. Haettner, E. *et al.* Production and separation of positron emitters for hadron therapy at FRS-Cave M. *Nucl. Instruments Methods Phys. Res. Sect. B Beam Interact. with Mater. Atoms* **541**, 114–116 (2023).
25. Gerlach, S. *et al.* Beam characterization and feasibility study for a small animal irradiation platform at clinical proton therapy facilities. *Phys. Med. Biol.* **65**, 245045 (2020).
26. Lovatti, G. *et al.* Design study of a novel geometrical arrangement for an in-beam small animal positron emission tomography scanner. *Phys. Med. Biol.* **68**, 235005 (2023).
27. Asai, T. *et al.* Establishment and characterization of a murine osteosarcoma cell line (LM8) with high metastatic potential to the lung. *Int. J. Cancer* **76**, 418–422 (1998).
28. Prudowsky, Z. D. & Yustein, J. T. Recent Insights into Therapy Resistance in Osteosarcoma. *Cancers (Basel)*. **13**, 83 (2020).
29. Shiba, S. *et al.* Impact of Carbon Ion Radiotherapy on Inoperable Bone Sarcoma. *Cancers (Basel)*. **13**, 1099 (2021).
30. Lo, Y.-C., McBride, W. H. & Rodney Withers, H. The effect of single doses of radiation on mouse spinal cord. *Int. J. Radiat. Oncol.* **22**, 57–63 (1992).
31. Geissel, H. *et al.* The GSI projectile fragment separator (FRS): a versatile magnetic system for relativistic heavy ions. *Nucl. Instruments Methods Phys. Res. Sect. B Beam Interact. with Mater. Atoms* **70**, 286–297 (1992).
32. Böhlen, T. T. *et al.* The FLUKA Code: Developments and Challenges for High Energy and Medical Applications. *Nucl. Data Sheets* **120**, 211–214 (2014).
33. Anderson, K. D., Abdul, M. & Steward, O. Quantitative assessment of deficits and recovery of forelimb motor function after cervical spinal cord injury in mice. *Exp. Neurol.* **190**, 184–191 (2004).
34. Toramatsu, C. *et al.* Measurement of biological washout rates depending on tumor vascular status in 15 O in-beam rat-PET. *Phys. Med. Biol.* **67**, 125006 (2022).
35. Baumann, M., Krause, M. & Hill, R. Exploring the role of cancer stem cells in radioresistance. *Nat Rev Cancer* **8**, 545–554 (2008).
36. Garcia-Barros, M. *et al.* Tumor response to radiotherapy regulated by endothelial cell

- apoptosis. *Science* **300**, 1155–9 (2003).
37. Fuks, Z. & Kolesnick, R. Engaging the vascular component of the tumor response. *Cancer Cell* **8**, 89–91 (2005).
 38. Bodo, S. *et al.* Single-dose radiotherapy disables tumor cell homologous recombination via ischemia/reperfusion injury. *J. Clin. Invest.* **129**, 786–801 (2019).
 39. Greco, C. *et al.* Safety and Efficacy of Virtual Prostatectomy With Single-Dose Radiotherapy in Patients With Intermediate-Risk Prostate Cancer. *JAMA Oncol.* **7**, 700 (2021).
 40. Zelefsky, M. J. *et al.* Phase 3 Multi-Center, Prospective, Randomized Trial Comparing Single-Dose 24 Gy Radiation Therapy to a 3-Fraction SBRT Regimen in the Treatment of Oligometastatic Cancer. *Int. J. Radiat. Oncol.* **110**, 672–679 (2021).
 41. Shuryak, I., Carlson, D. J., Brown, J. M. & Brenner, D. J. High-dose and fractionation effects in stereotactic radiation therapy: Analysis of tumor control data from 2965 patients. *Radiother. Oncol.* **115**, 327–334 (2015).
 42. Brown, J. M., Brenner, D. J. & Carlson, D. J. Dose escalation, not ‘new biology,’ can account for the efficacy of stereotactic body radiation therapy with non-small cell lung cancer. *Int. J. Radiat. Oncol. Biol. Phys.* **85**, 1159–1160 (2013).
 43. Park, H. J., Griffin, R. J., Hui, S., Levitt, S. H. & Song, C. W. Radiation-Induced Vascular Damage in Tumors: Implications of Vascular Damage in Ablative Hypofractionated Radiotherapy (SBRT and SRS). *Radiat. Res.* **177**, 311–327 (2012).
 44. Bendinger, A. L. *et al.* High Doses of Photons and Carbon Ions Comparably Increase Vascular Permeability in R3327-HI Prostate Tumors: A Dynamic Contrast-Enhanced MRI Study. *Radiat. Res.* **194**, (2020).
 45. Jani, A. *et al.* High-Dose, Single-Fraction Irradiation Rapidly Reduces Tumor Vasculature and Perfusion in a Xenograft Model of Neuroblastoma. *Int. J. Radiat. Oncol.* **94**, 1173–1180 (2016).
 46. Kalantar-Nayestanaki, N. & Scheidenberger, C. Experiments at the Interface of Nuclear, Atomic, and Hadron Physics with FRS at GSI and Super-FRS at FAIR. *Nucl. Phys. News* **34**, 21–26 (2024).
 47. Mohammadi, A. *et al.* Influence of momentum acceptance on range monitoring of 11 C and 15 O ion beams using in-beam PET. *Phys. Med. Biol.* **65**, 125006 (2020).
 48. Hamato, A. *et al.* Dose estimation using in-beam positron emission tomography: Demonstration for 11C and 15O ion beams. *Nucl. Instruments Methods Phys. Res. Sect. A Accel. Spectrometers, Detect. Assoc. Equip.* **1066**, 169643 (2024).
 49. Penescu, L. *et al.* Technical Design Report for a Carbon-11 Treatment Facility. *Front. Med.* **8**, (2022).
 50. Augusto, R. S. *et al.* New developments of 11C post-accelerated beams for hadron therapy and imaging. *Nucl. Instruments Methods Phys. Res. Sect. B Beam Interact. with Mater. Atoms* **376**, 374–378 (2016).
 51. Tashima, H. *et al.* A single-ring OpenPET enabling PET imaging during radiotherapy. *Phys. Med. Biol.* **57**, 4705–4718 (2012).

52. Moglioni, M. *et al.* In-vivo range verification analysis with in-beam PET data for patients treated with proton therapy at CNAO. *Front. Oncol.* **12**, (2022).
53. Toramatsu, C. *et al.* Tumour status prediction by means of carbon-ion beam irradiation: comparison of washout rates between in-beam PET and DCE-MRI in rats. *Phys. Med. Biol.* **68**, 195005 (2023).
54. Boscolo, D. *et al.* Depth dose measurements in water for 11C and 10C beams with therapy relevant energies. *Nucl. Instruments Methods Phys. Res. Sect. A Accel. Spectrometers, Detect. Assoc. Equip.* **1043**, 167464 (2022).
55. Luoni, F. *et al.* Beam Monitor Calibration for Radiobiological Experiments With Scanned High Energy Heavy Ion Beams at FAIR. *Front. Phys.* **8**, (2020).
56. Schuy, C., Simeonov, Y., Durante, M., Zink, K. & Weber, U. Technical note: Vendor-agnostic water phantom for 3D dosimetry of complex fields in particle therapy. *J. Appl. Clin. Med. Phys.* **21**, 227–232 (2020).
57. Kikinis, R., Pieper, S. D. & Vosburgh, K. G. 3D Slicer: A Platform for Subject-Specific Image Analysis, Visualization, and Clinical Support. in *Intraoperative Imaging and Image-Guided Therapy* 277–289 (Springer New York, 2014). doi:10.1007/978-1-4614-7657-3_19
58. Downey, C. M. *et al.* Quantitative Ex-Vivo Micro-Computed Tomographic Imaging of Blood Vessels and Necrotic Regions within Tumors. *PLoS One* **7**, e41685 (2012).
59. Yerger, J. *et al.* Phenotype assessment for neurodegenerative murine models with ataxia and application to Niemann–Pick disease, type C1. *Biol. Open* **11**, (2022).

Acknowledgements

The BARB experiments are supported by European Research Council (ERC) Advanced Grant 883425 BARB to M.D. The construction of the SIRMIO PET scanner was partly supported by the ERC Consolidator Grant 725539 SIRMIO to K.P. The measurements described here are performed within the experiments B-22-00046-Durante at SIS18/FRS/Cave-M at the GSI Helmholtzzentrum für Schwerionenforschung, Darmstadt (Germany) in the frame of FAIR Phase-0. The authors are grateful to: the SIS18 accelerator crew for their excellent support in the beam preparation and delivery; R. Chowdhury, L. Hartig, M. Ibáñez-Moragues, J. Oppermann, A. Puspitasari-Kokko, and C. Vandevoorde for their assistance in handling the animals during irradiations and follow-up; C. Galeone, R. Kumar Prajapat, G. Li, M.C. Martire and L. Volz for their assistance during the beamtime shifts; S. Kumar Singh prepared the settings for ^{11}C ; A.L. Gera, C. Hartmann-Sauter, T. Wagner and R. Khan for the beamline setup realization and installation; E. Rocco refurbished the grids needed for beam alignment; A. Noto for working on the SIRMIO PET during the irradiation; A. Bückner for his support with μCT and calibrations; B. Franczak for the optical calculations that make possible the transfer of the RIB in Cave M; K. Zink for providing the PeakFinder tool used in our dosimetry measurements; T. Yamaya, H.G. Kang, A. Zoglauer and C. Gianoli for their collaboration on the SIRMIO PET scanner and image reconstruction. This paper is dedicated to the memory of Prof. Dr. Hans Geissel (1950-2024), whose unwavering support, encouragement, and insightful suggestions were invaluable to this research.

Author information

D.B. prepared the physics protocol and performed the dosimetry; G.L. is the primary responsible for PET data acquisition and analysis; O.S. linked biology and physics protocols, performed all μCT and performed a large part of the data analysis; T.V. worked on the animals, tumor growth and performed all toxicity tests; F.E., M.N. and P.G.T. worked on the PET detector and data acquisition; E.H., S.P., and D.K. were responsible of the secondary beam production at FRS; W.T. supervised the animal model and participated in the experiments; C.G. provided essential conceptual input and participated in the experiments; U.W. and C. Schuy performed the beam dosimetry; M.M. performed the FLUKA simulations; J.B. prepared the animal holder; C. Scheidenberger supervised all FRS activities and is responsible for production, separation and identification of the RIB; K.P. conceived and supervised the realization of the SIRMIO PET scanner, participated in all experiments and supported the interpretation and analysis of the PET data; M.D. conceived and supervised the BARB project, participated in every phase of the experiments, analyzed part of the data and wrote the first draft of the paper; all authors read and revised the manuscript.

Ethics declarations

Competing interests

The authors declare no competing interests.

Figure captions

Figure 1. Mouse model and μ CT. **A.** LM8 osteosarcoma as visible by eye or at the μ CT at different times after cell inoculation. For the irradiation, a two-weeks timepoint was chosen. **B.** Contours of the individual mice tumor GTVs (green) near the OAR (spinal cord). The “universal CTV” contour (purple) was applied to all animals.

Figure 2. Experimental beamline. **A.** Drawing of the different elements along the experimental beamline. **B.** Animal holder with the anesthesia tubes and a mouse in position. **C.** Animal holder aligned in the beamline while the SIRMIO PET is raised. **D.** SIRMIO is then lowered to surround the animal. **E.** Lateral view of the full beamline.

Figure 3. RIB imaging. **A.** FLUKA simulation of the beamline in [Fig.2](#) shows the expected ^{11}C -ion dose (in Gy) distribution in the mouse on a z-y plane parallel to the beam. The universal CTV contour ([Fig. 1](#)) is highlighted with red line. **B.** FLUKA simulation of the integrated positron annihilation map in the same animal in panel A. **C.** Real-time SIRMIO PET image of the integrated activity distribution deposited after 3 min ^{11}C -irradiation in the same mouse. **D.** For the same mouse, measured activity (blue) and simulated positron annihilation map (red) activity integrated along the x-axis plotted with the dose profile along the beam direction (z) in green. The tumor and spine regions are highlighted by pink and red bands, respectively, while the collar is depicted in yellow and the dimple (see [Extended Fig. 4B](#)) in light blue.

Figure 4. Tumor growth. **A.** Estimated volume from 2D caliper measurements of the visible tumor (see Methods). Asterisks indicate statistical significance using the ANOVA test. **B.** Measurements of the volumes using μ CT. Data are more precise than caliper measurements, but they are less frequent than external measurements. **C.** Zoom of the data points for irradiated groups shows the recurrence of the tumor irradiated with 5 Gy. Bars are standard errors of the mean values from the different animals.

Figure 5. Toxicity vs. activity in the spinal cord. Animals exposed to ^{11}C -ions shows a lower forelimb strength in the grip test ([Extended data Fig. 7](#)) compared to controls. Individual data are shown in [Supplementary Fig. 2](#). Data for irradiated animals were only considered from week 6, assuming no radiation effect in the first month post-irradiation. **A.** Median grip strength values in the control (8 animals) and irradiated (13 animals) groups. Bars are standard errors of the median values ($= 1.2533 \cdot \sigma / \sqrt{n}$). Median strength in the control group is significantly higher than in the irradiated group (Mood’s median test, $p=0.0152$). **B.** Fraction of time points ([Supplementary Fig. 2](#)) where the measured peak force F was lower than 100 N. Bars are standard errors of the mean. The fraction is significantly higher in irradiated animals (Mann-Whitney test, $p=0.00024$). **C.** Correlation between median grip strength values in single irradiated animals and total PET counts in the spinal cord. **D.** Correlation between fraction of tests with $F < 100$ N in individual irradiated animals and total PET counts in the spinal cord. Each point represents a single animal. The grey area is the 95% CI around the regression line, r is

the correlation coefficient and significance of the correlation was evaluated by Pearson's test both in **C** and **D** panels.

Figure 6. Radioactive washout. Individual activity data recorded after the end of irradiation in [Supplementary Fig. 3](#) are grouped in the upper panel (left: 5 Gy, middle: 20 Gy, right: comparison of fit functions assuming the physics decay of the beam containing 96% ^{11}C , 3% ^{10}C , and 0.5% ^{15}O ions). As a fit function, a double-exponential decay function was chosen over a single-exponential decay following the results of the F-test (ratio of the fit χ^2 with 1 or 2 parameters) with number of degrees of freedom $df > 100$. $F(5\text{ Gy}) = 1126 (\gg 1)$, $F(20\text{ Gy})=63 (\gg 1)$. Double-exponential decay rates and the weight of the slow component are shown in the bottom panel for 5 Gy and 20 Gy. Significance of the differences is assessed by t-test, and p -values are shown.

Extended data

Extended data Fig. 1. Fragment separator at GSI. A schematic view of the FRS is shown.

A primary beam of ^{12}C -ions from the SIS-18 synchrotron was incident on a beryllium target to produce ^{11}C -ions, separated using the $B\rho\text{-}\Delta E\text{-}B\rho$ method. An achromatic degrader was placed at the mid-focal plane of the FRS. The FRS has three experimental branches for delivering the separated radioactive ion beam. The branch directed to Cave-M is indicated in the figure. The elements between the last dipole of the FRS and Cave-M belong to the high-energy beam transport line of GSI, designed for primary beams and therefore having smaller apertures than the FRS magnetic elements, leading to reduced transmission efficiency of secondary beams to the Cave-M.

Extended data Fig. 2. Dosimetry of the monoenergetic ^{11}C beam. Laterally integrated depth dose profile in water (top left), 2D dose distribution of the beam spot at the entrance of the water phantom (bottom left), vertical and horizontal 2D dose distributions in the central plane along the beam direction (top right and bottom right) for the pristine Bragg peak.

Extended data Fig. 3. Dosimetry of the SOBP. Laterally integrated depth dose profile in water (top left), 2D dose distribution of the beam spot at the entrance of the water phantom (bottom left), vertical and horizontal 2D dose distributions in the central plane along the beam direction (top right and bottom right) for the SOBP.

Extended Data Fig. 4. Cave M beamline components. The scheme of the beamline is shown in Fig. 2A. A. Range modulator used to generate the SOBP from a monoenergetic pencil beam scan. B. Plastic compensator to shape the lateral and distal edges of the irradiation field to the CTV. The length is 25 mm to shield the base of the skull and the rest of the animal spine. Top: inner side with an anatomical cut for fixing the animal neck area Bottom: outer side with a dimple corresponding to the distal edge of the CTV calculated in water-equivalent thickness.

Extended data Fig. 5. Treatment of the mouse osteosarcoma with 20 Gy X-rays. A. Tumour growth curve, showing full tumor control after 20 Gy (5 mice, bars are standard errors of the mean values). B. Image of a mouse 6 months after exposure to 20 Gy X-rays suffering severe weight loss and kyphosis (see also [Supplementary video 3](#)). C. Pooled weights of tumor-bearing animals after receiving X-rays (orange circles, 15 and 20 Gy) or ^{11}C treatment (blue squares; 20 Gy). Lines represent the linear fit of the data from each group. The slope coefficients are 0.215 ± 0.046 and 0.525 ± 0.019 for the X-ray and ^{11}C groups, respectively and they are significantly different (t-test, $p<0.0001$). According to the ethical protocol, animals losing $>10\%$ of the weight have to be sacrificed, and for this reason some data acquisition is stopped early. The weight loss and myelopathy in these mice is due to the high dose to spine and esophagus of the X-ray beam that goes through the tumor.

Extended data Fig. 6. Skin toxicity in animals exposed to 5 and 20 Gy ^{11}C -ions. The Table shows the severity scale, and the images gives examples of the observed toxicities in the irradiated area. Grade 4 was only observed in control animals and was caused by

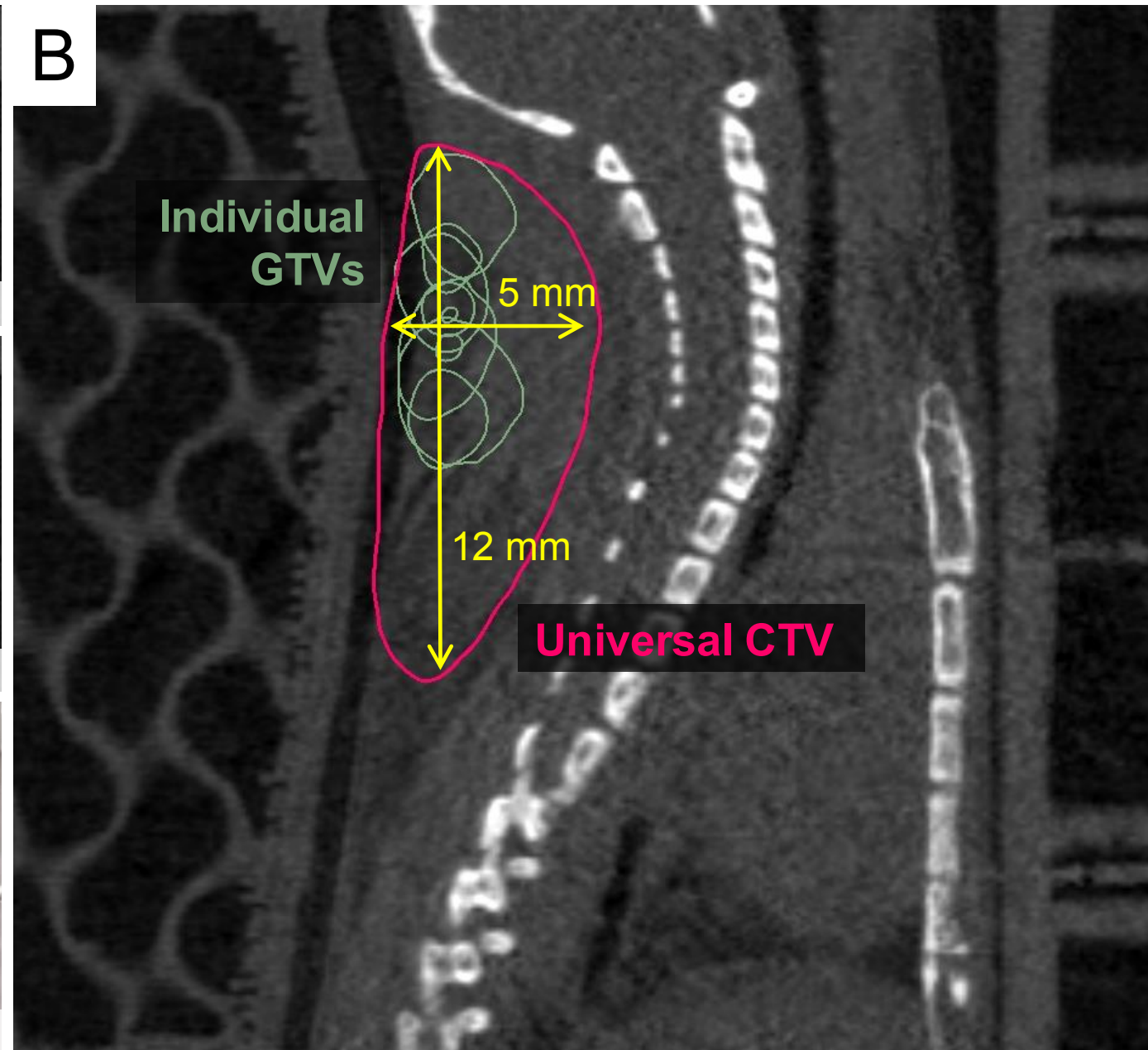
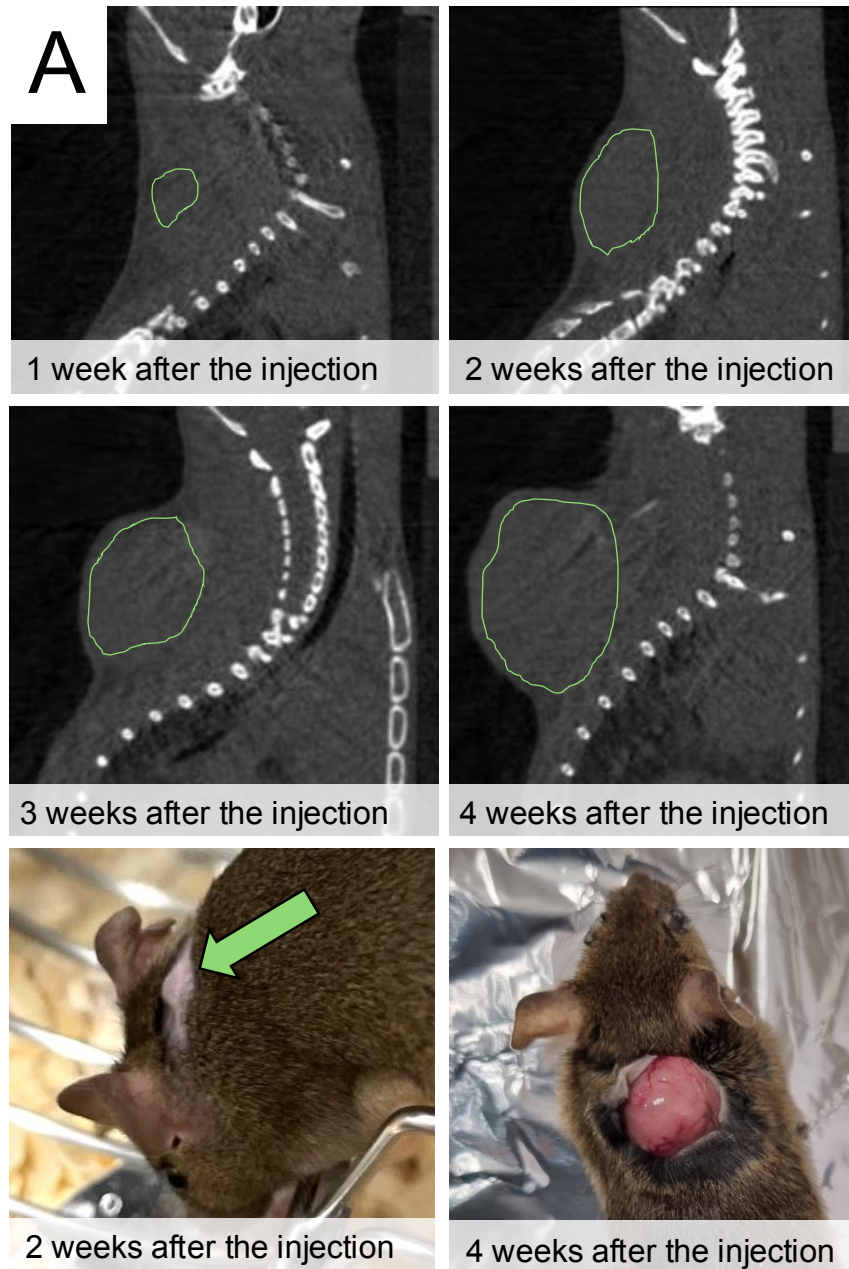
excessive tumour growth. Those animals had to be scarified as specified in the ethical protocol.

Extended data Fig. 7. Grip strength test used to estimate the cervical myelopathy. **A.** In this quantitative test the animal is pulled by the tail and the strength of the grip on the bar is measured in newton (N). **B.** Control mouse during the test (lateral view). **C.** 20 Gy irradiated mouse during the test. The area behind the head is shaved prior to the tumor inoculation, and after the irradiation only some white fur grows back.

Extended Data Table 1. Summary of the beam parameters used in the experiments.

Spill length	200 ms
Duty cycle	6.25%
¹² C beam energy	300 MeV/u
¹¹ C beam energy	209 MeV/u
¹² C intensity in SIS18	$1.6 \cdot 10^{10}$ particles/spill
¹¹ C intensity in Cave M	$2.5 \cdot 10^6$ particles/spill
Beamspace shape	Horizontal direction: 2.335 cm FWHM Vertical direction: 1.415 cm FWHM
Momentum spread	60% Gaussian – FWHM=0.011 GeV/c·u 40% flat distribution: FWHM=0.018 GeV/c·u

Fig.1



A

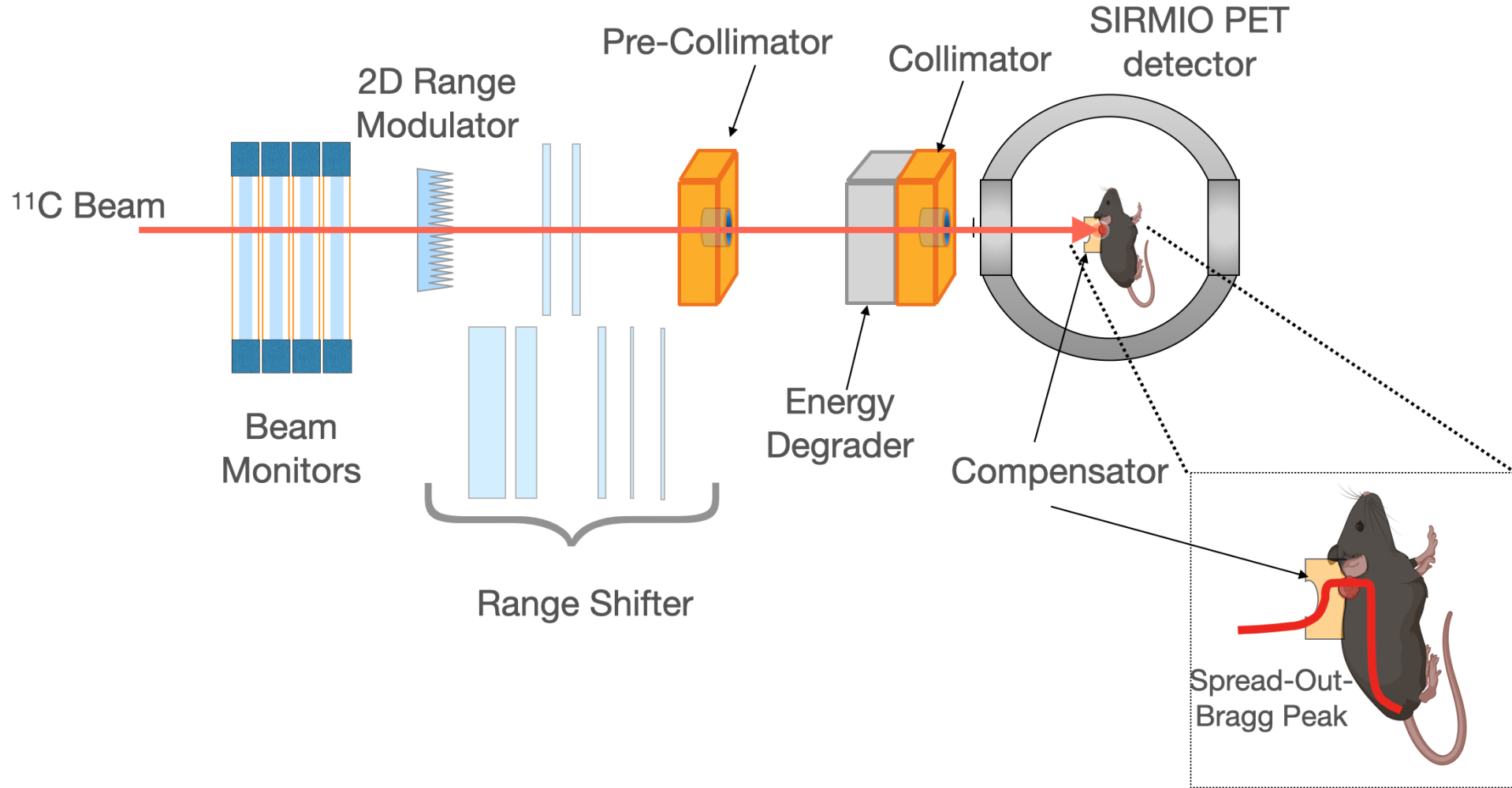


Figure 2A

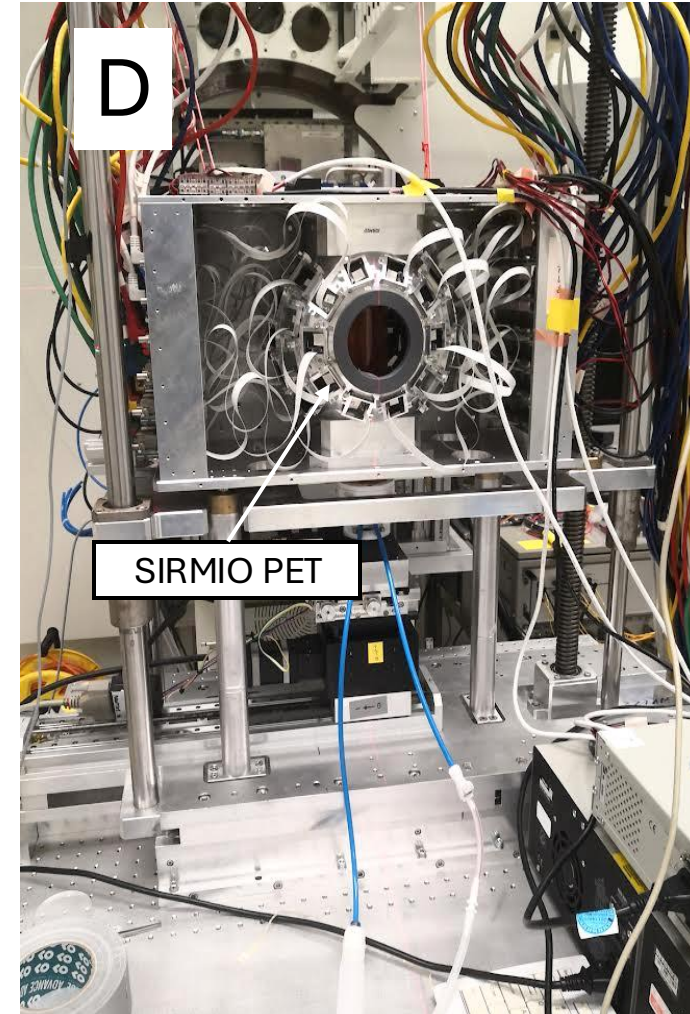
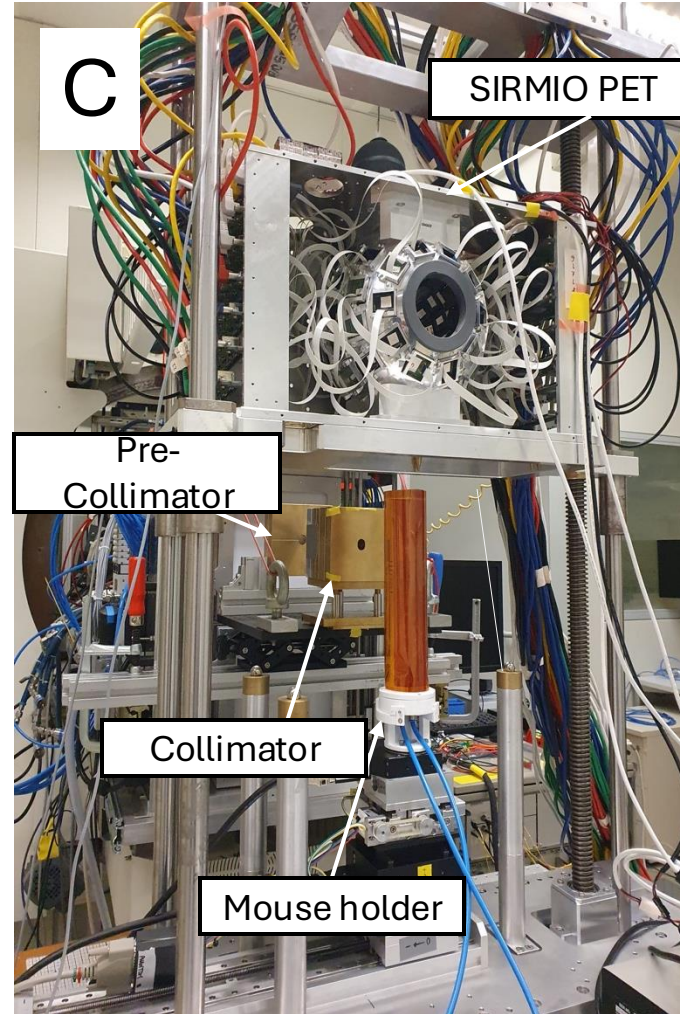


Figure 2B-D

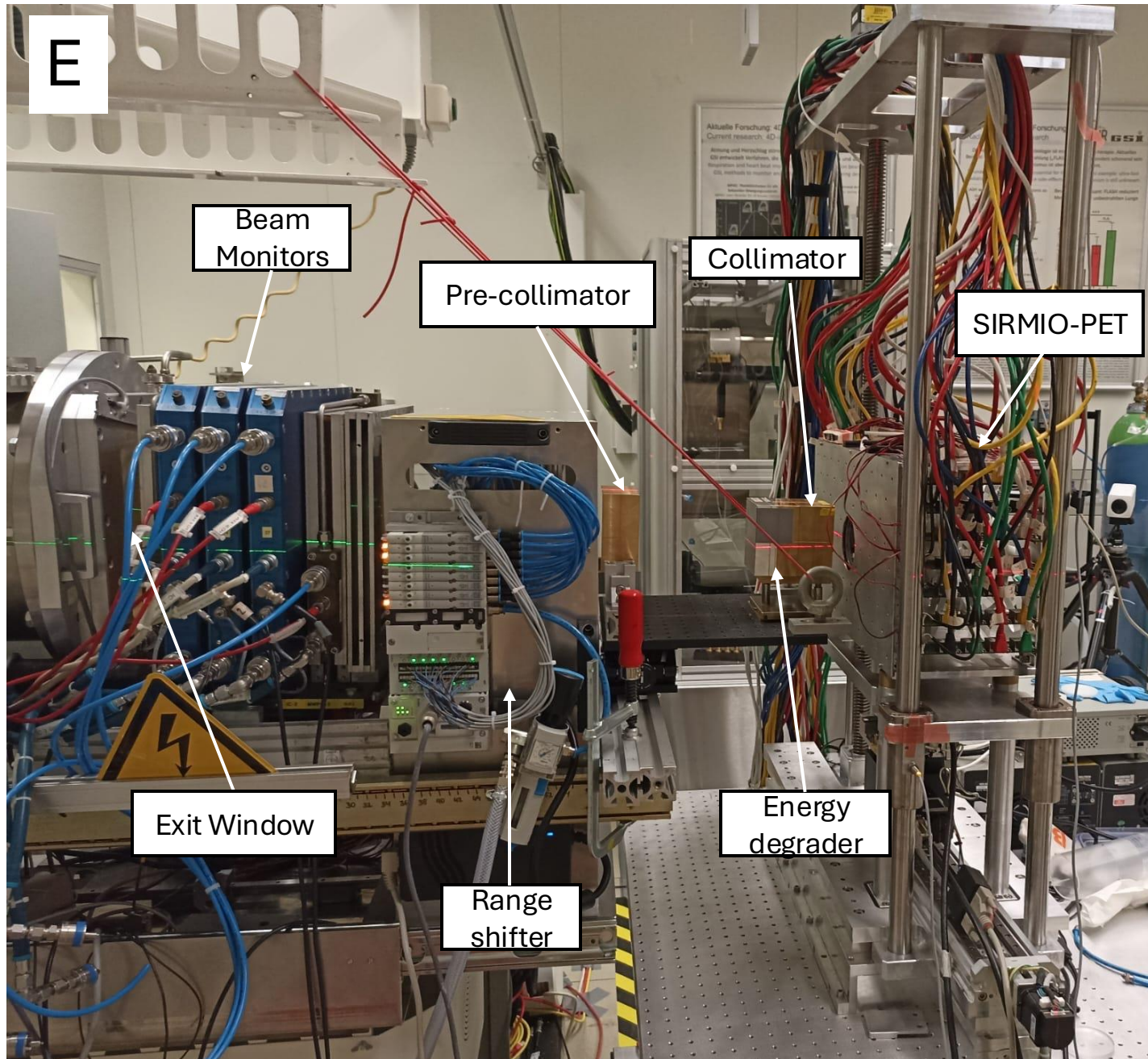
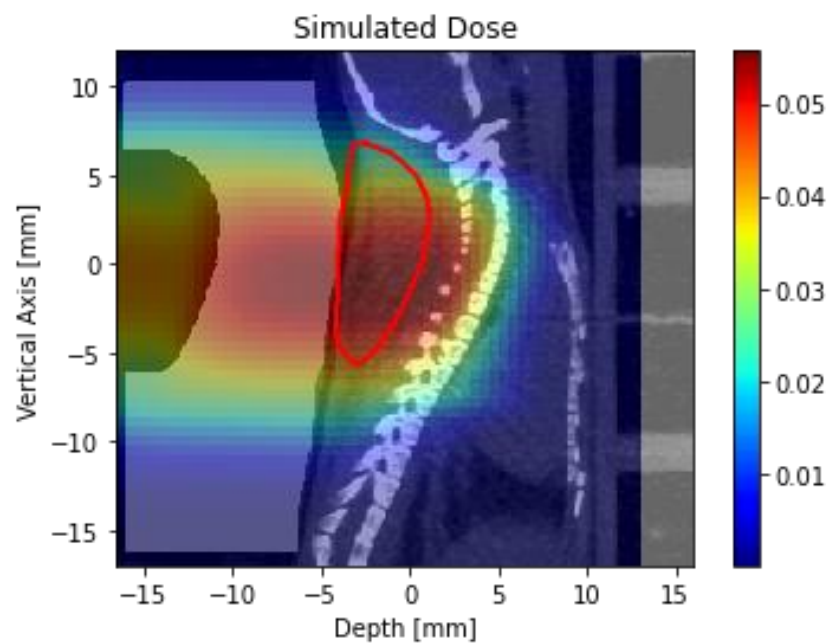
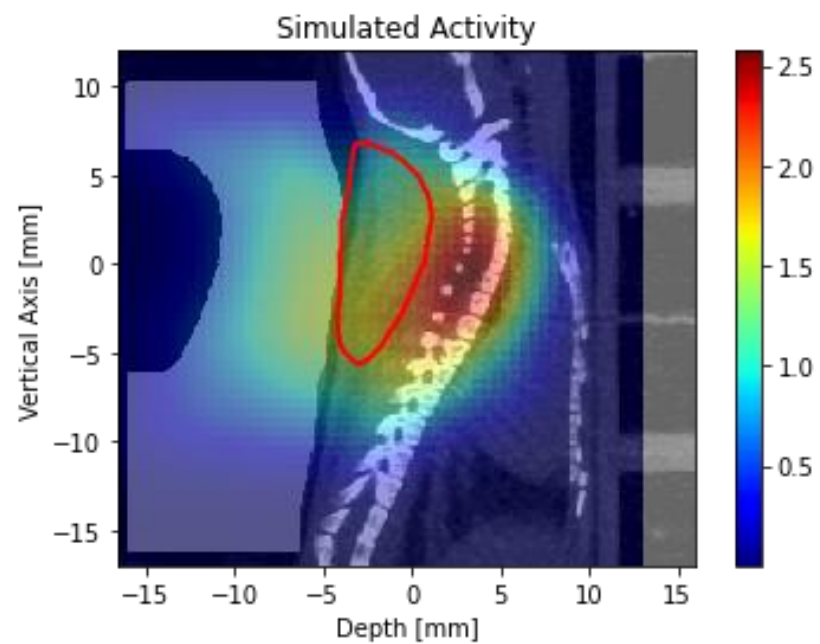
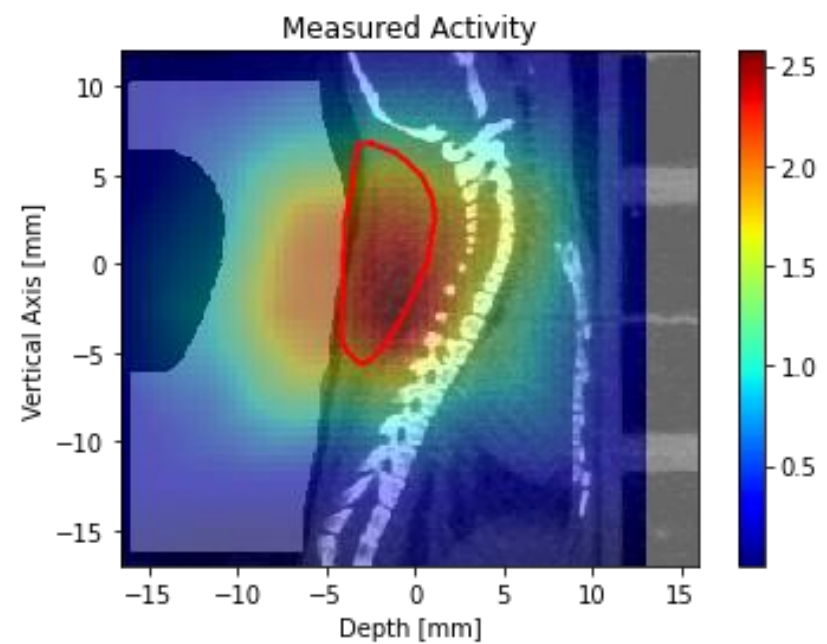


Figure 2E

A**B****C****Figure 3 A-C**

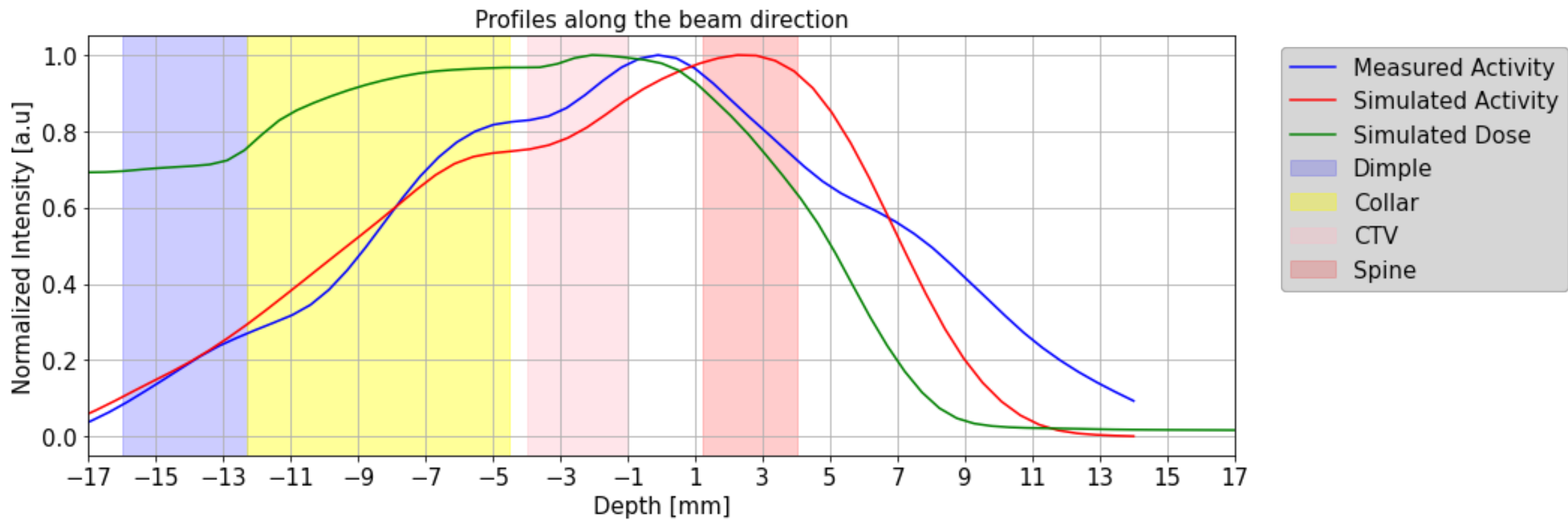


Figure 3 D

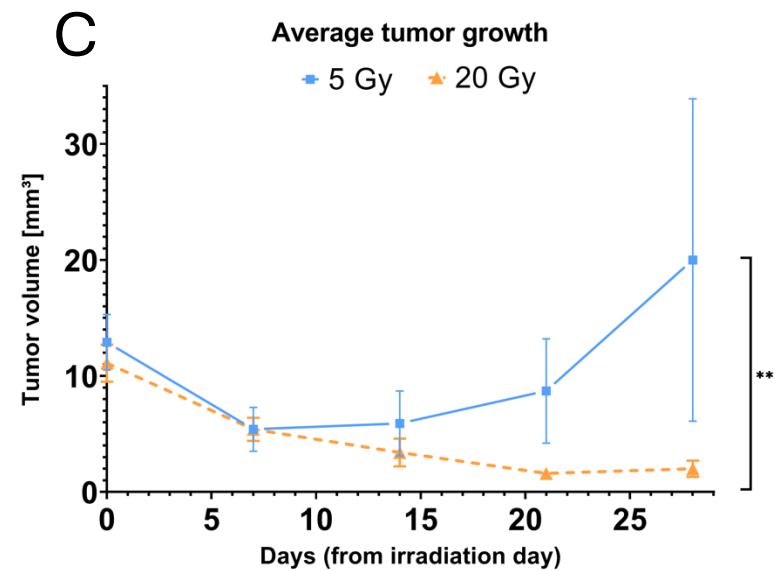
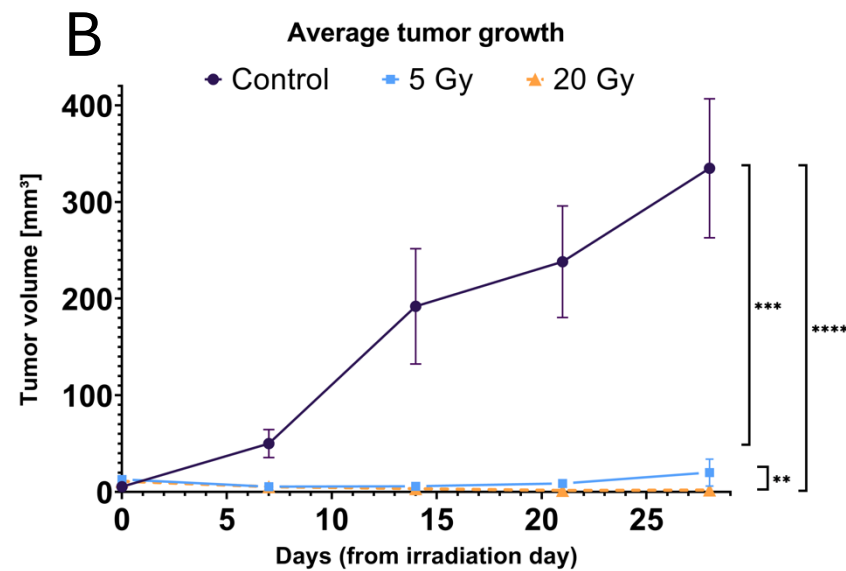
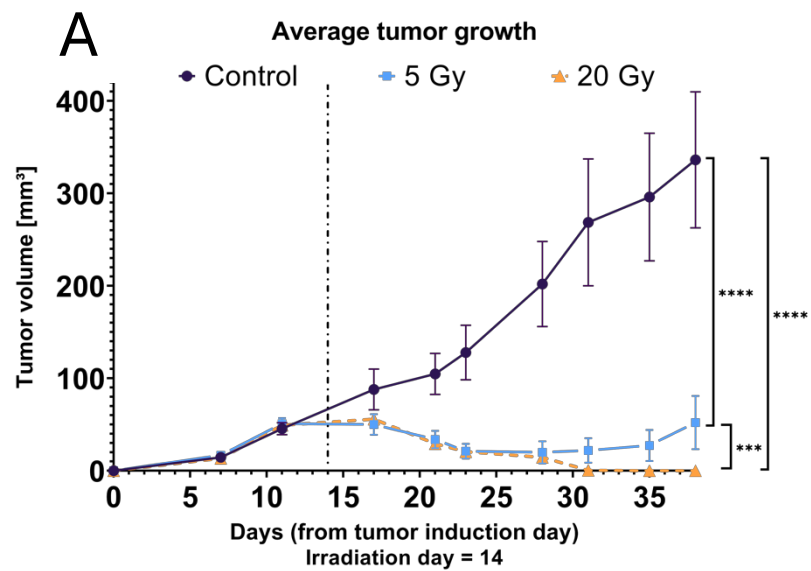


Figure 4

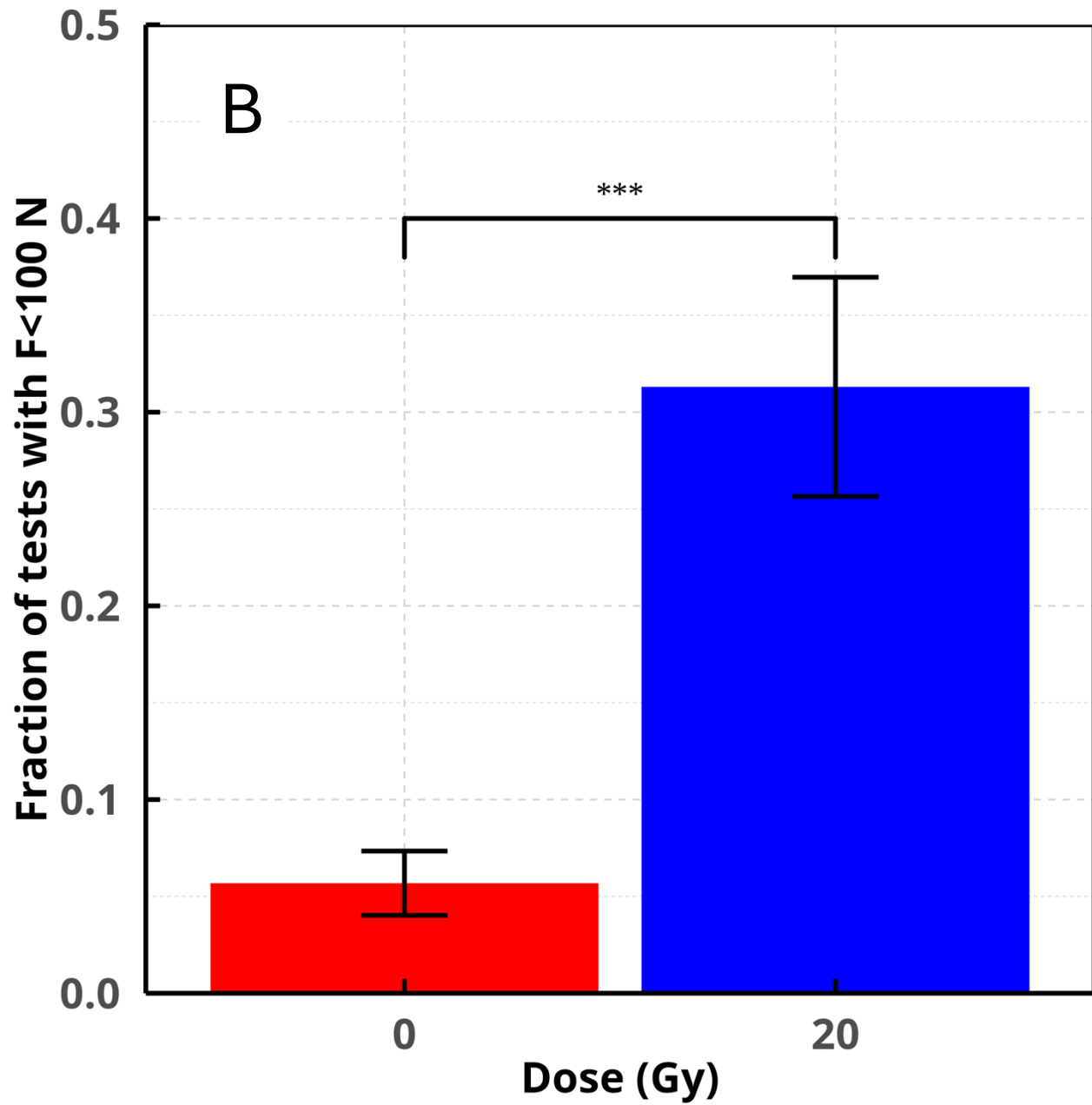
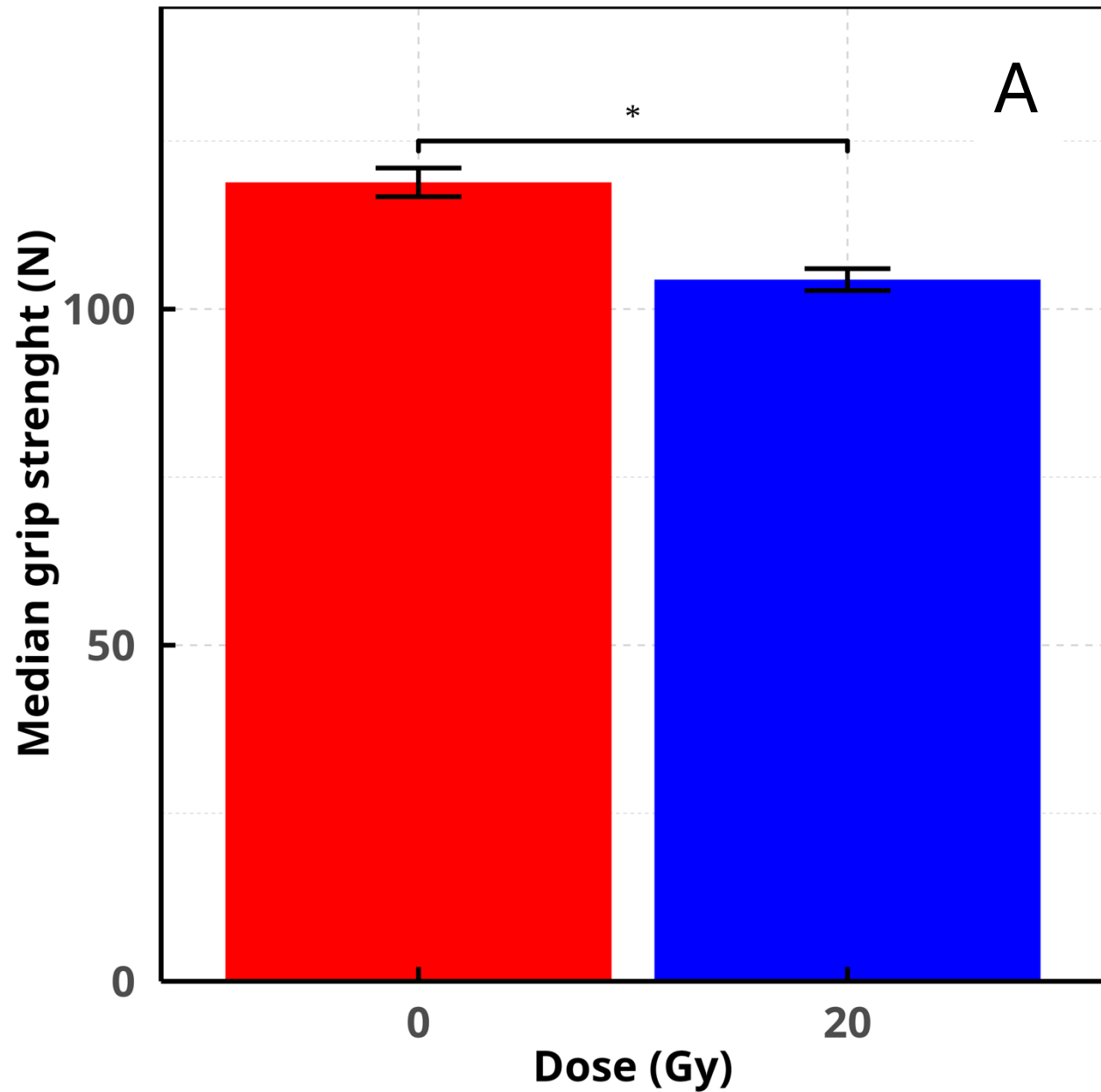


Figure 5 A-B

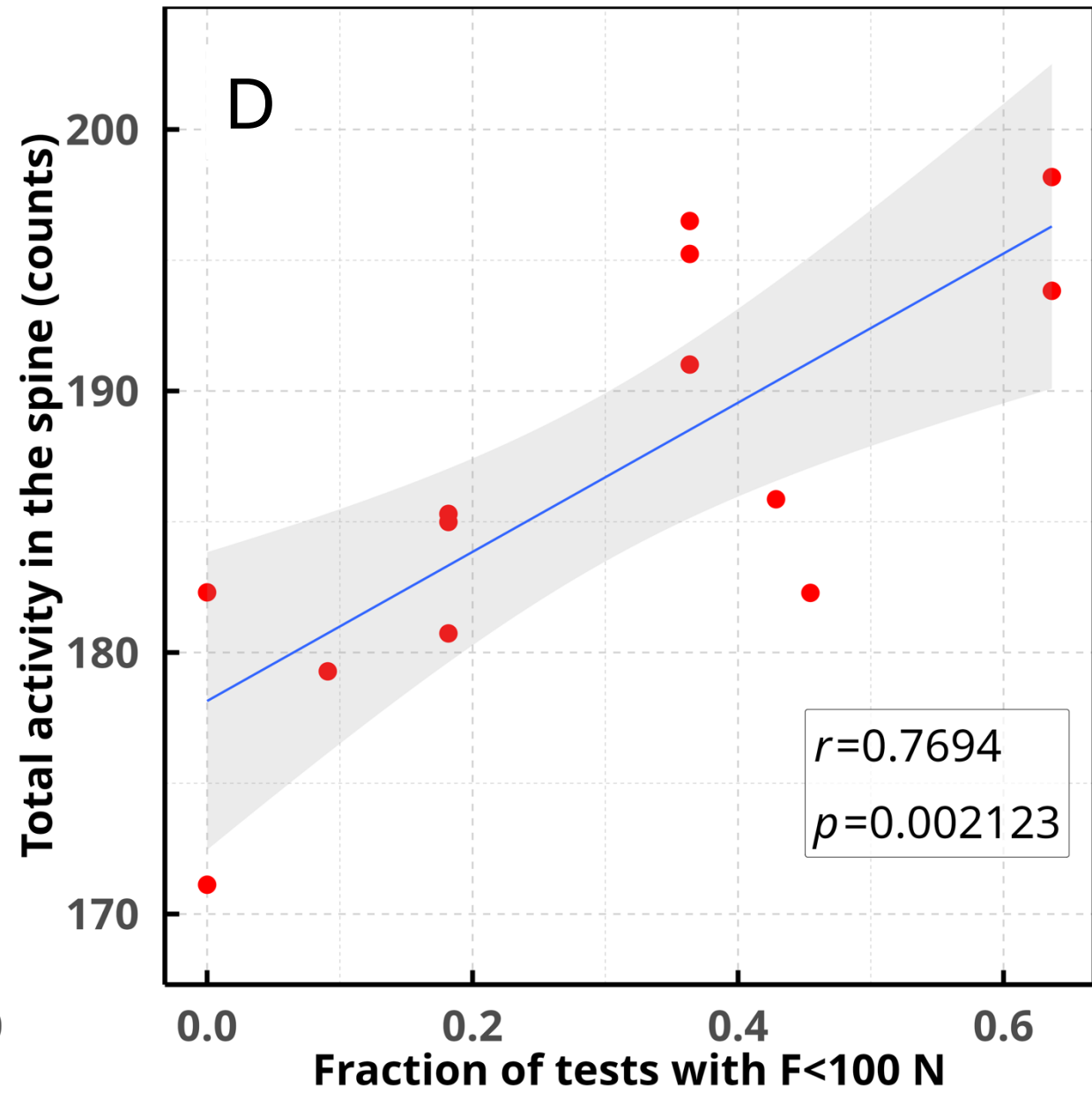
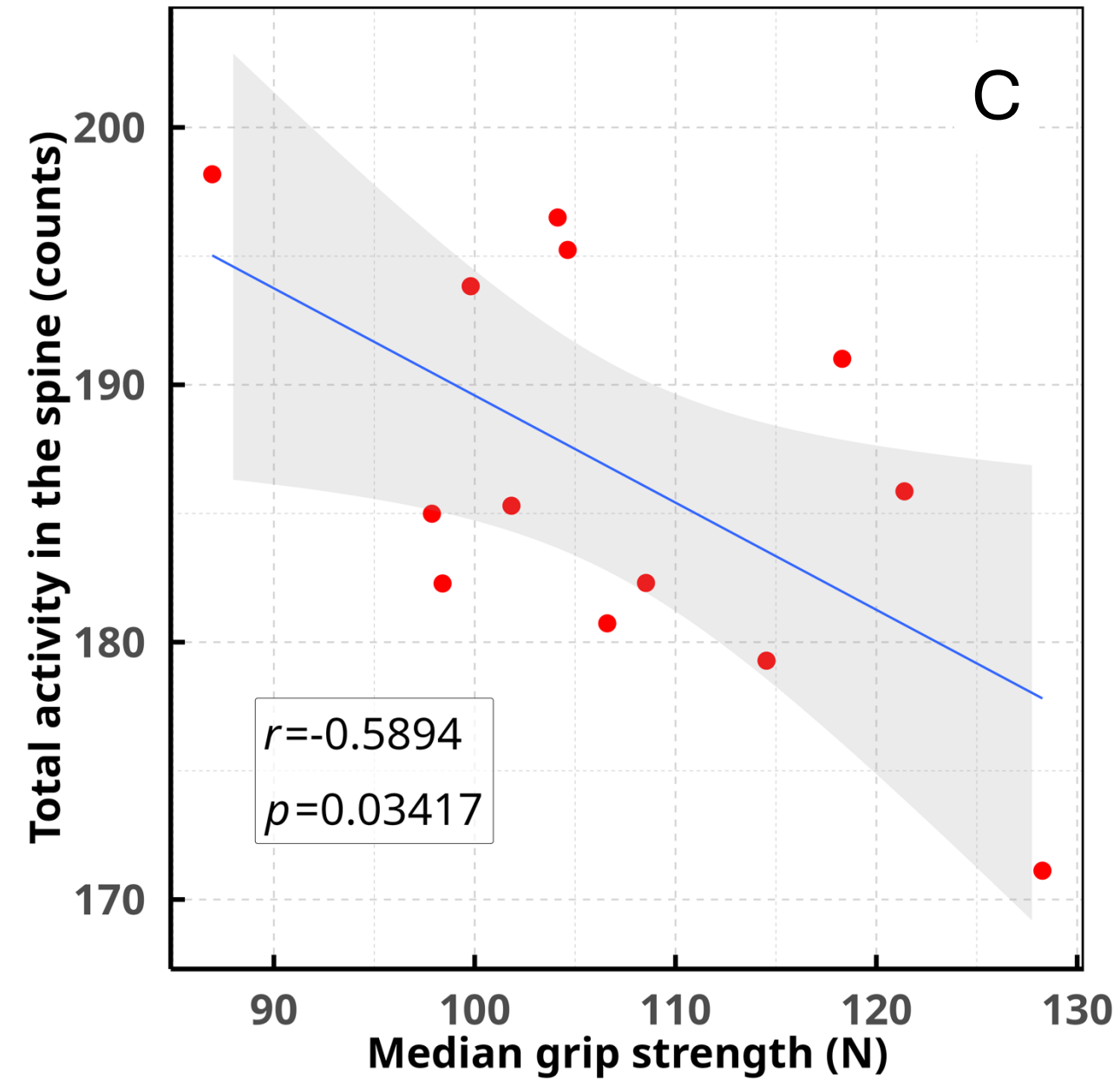


Figure 5 C-D

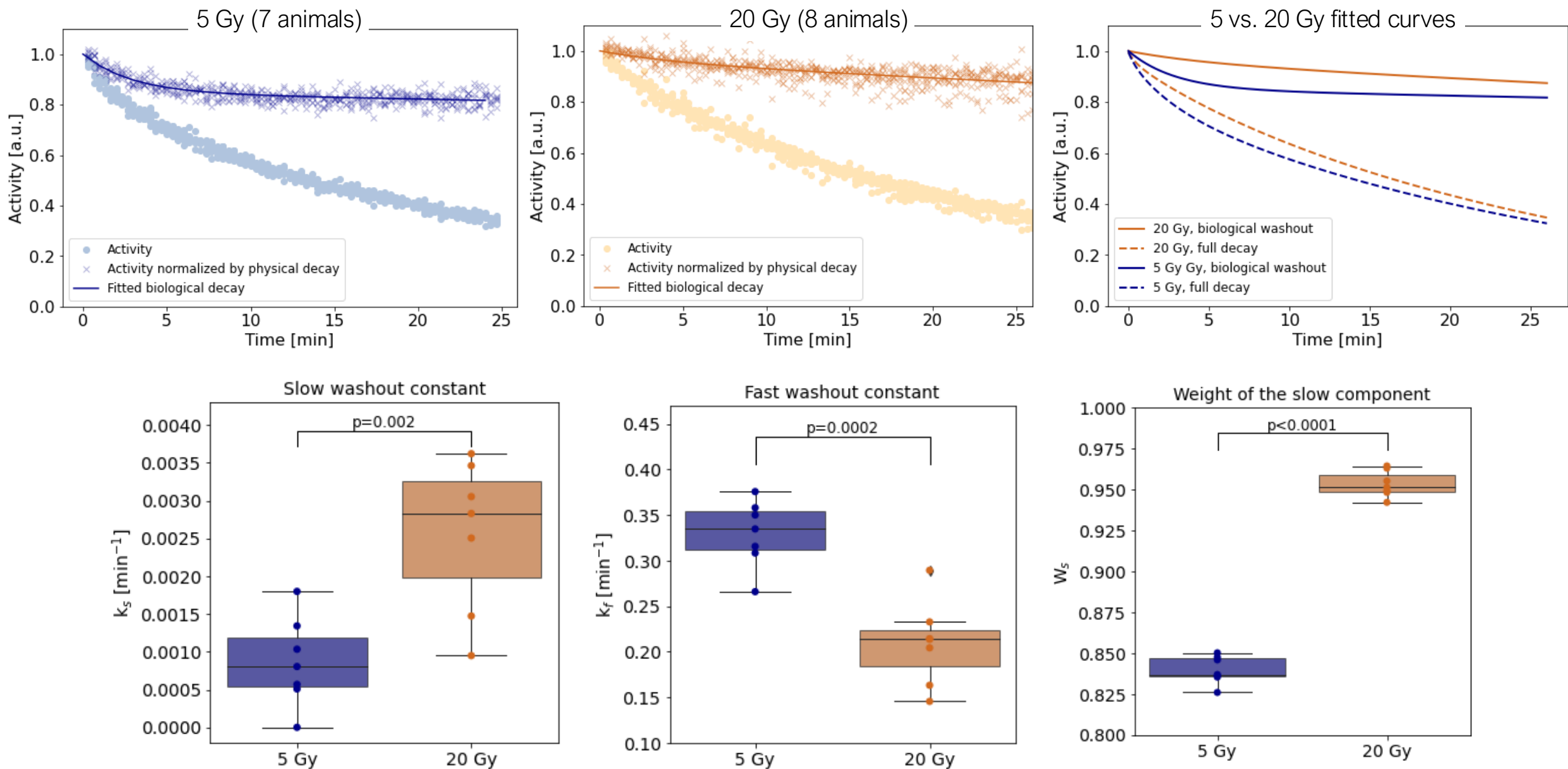
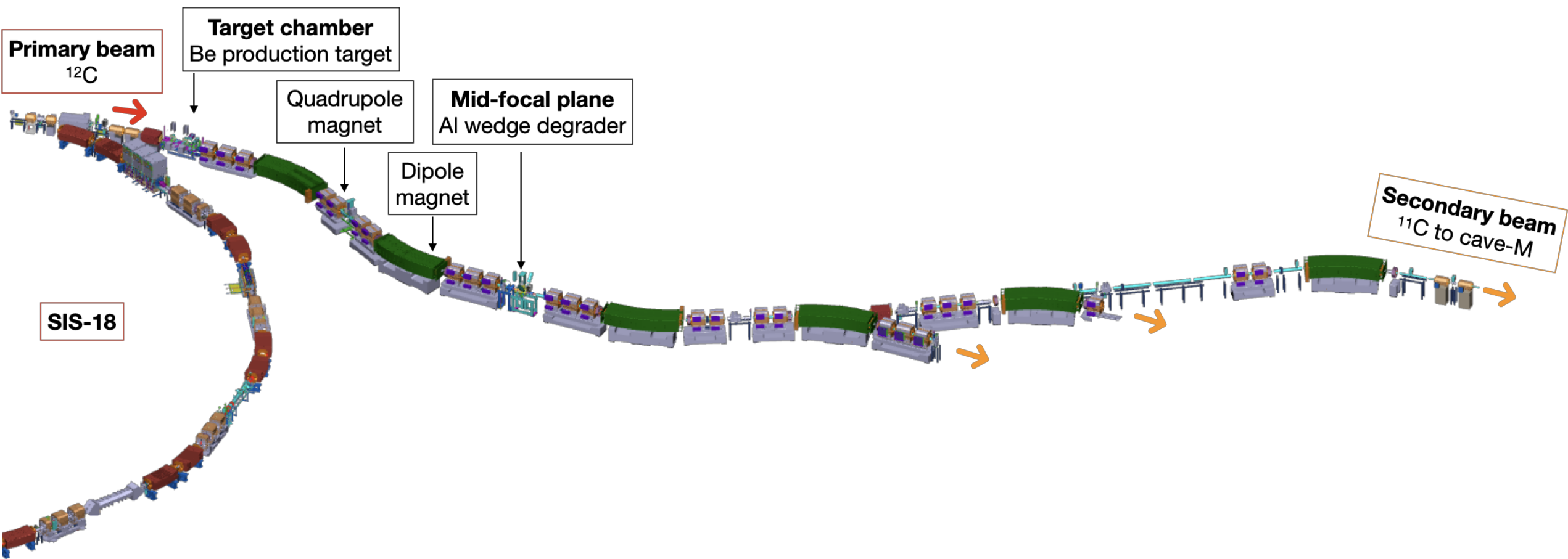
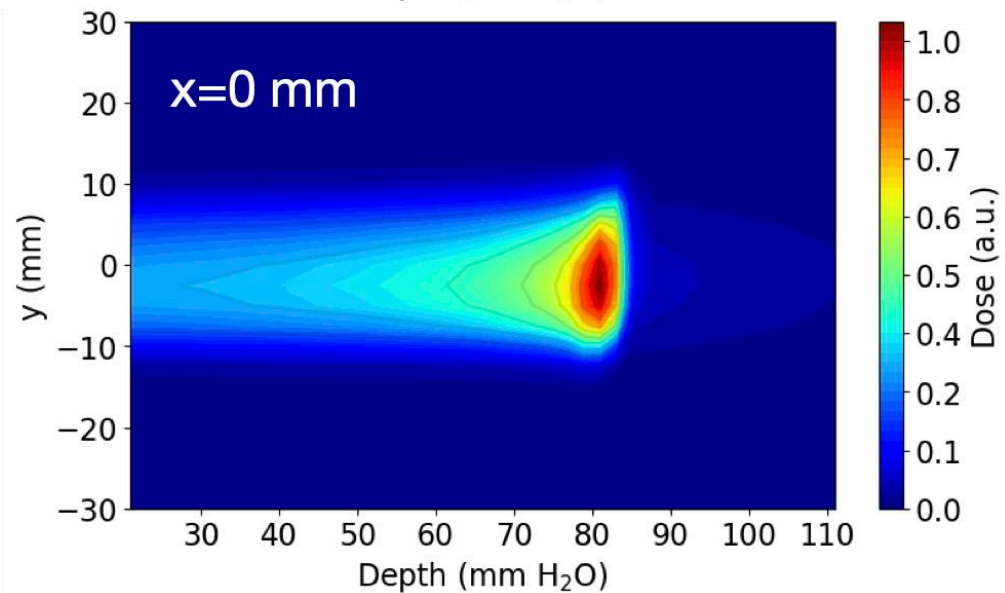
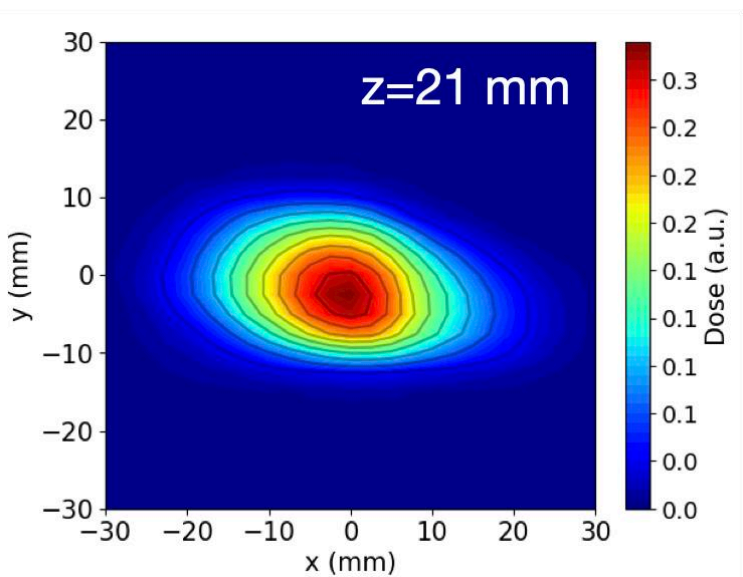
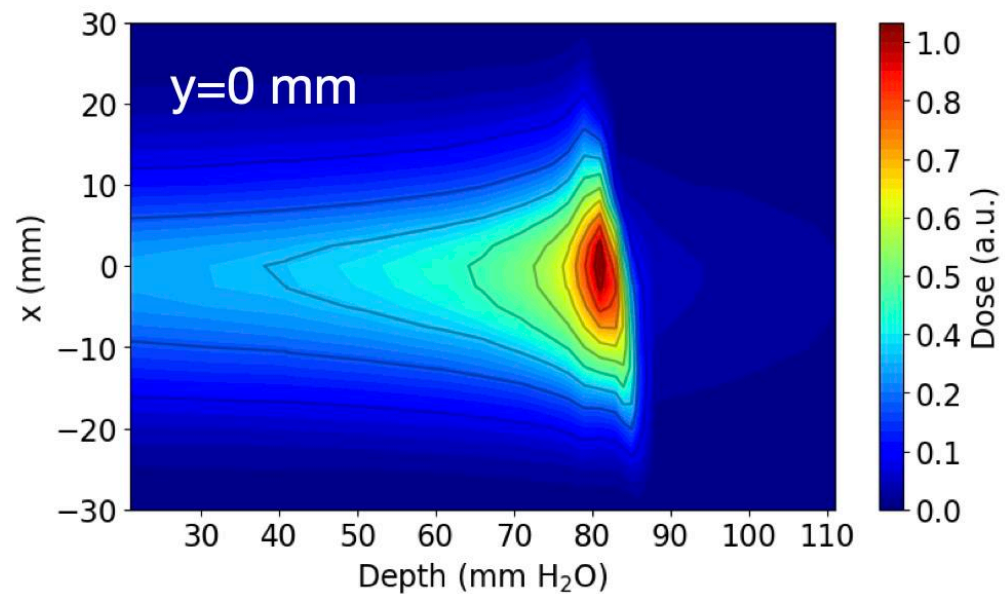
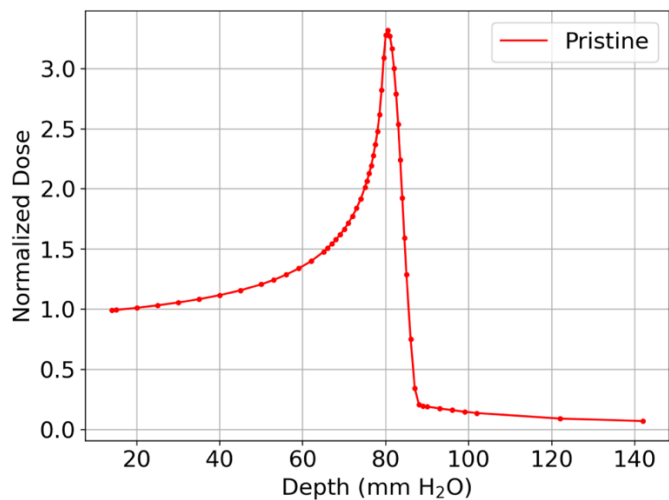


Figure 6

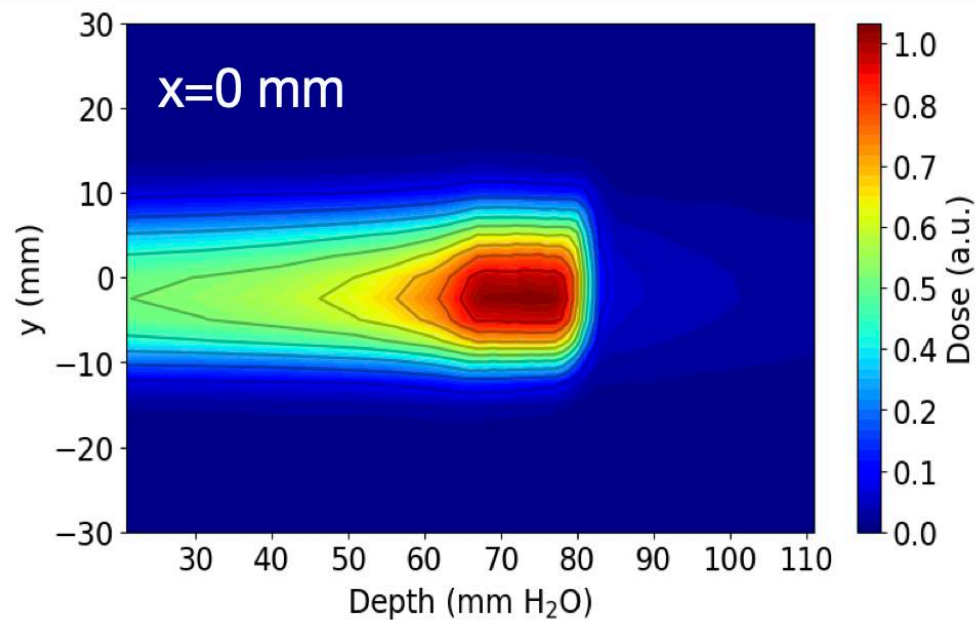
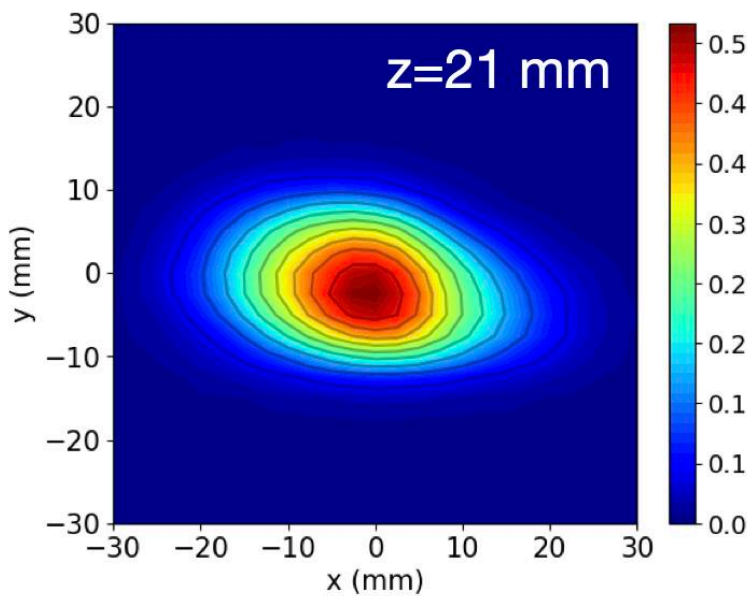
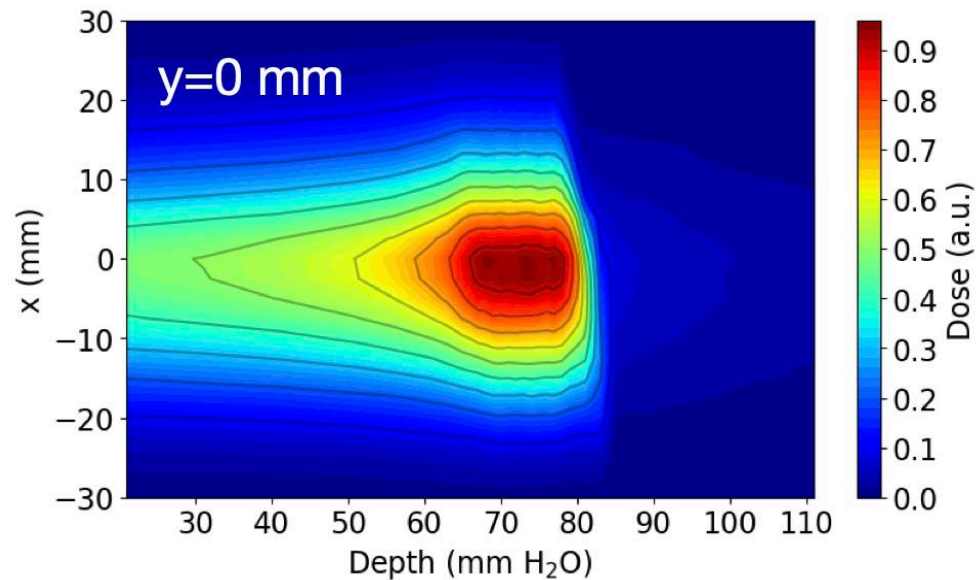
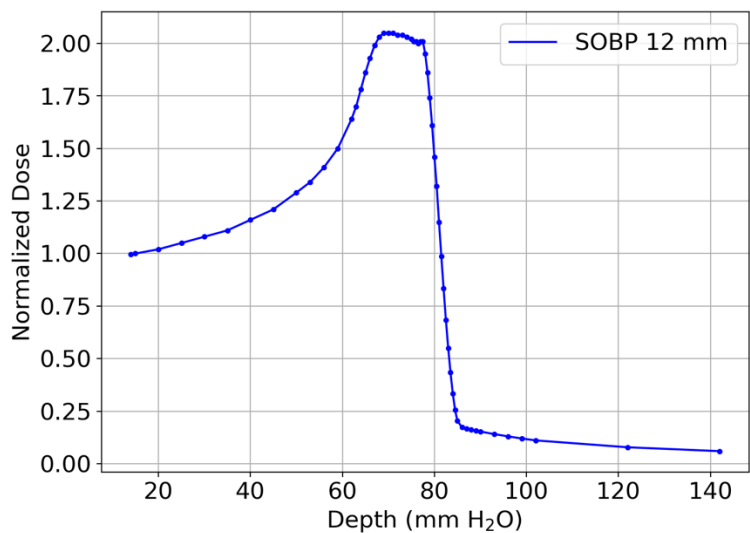


Extended Data Fig. 1

Extended Data Fig. 2

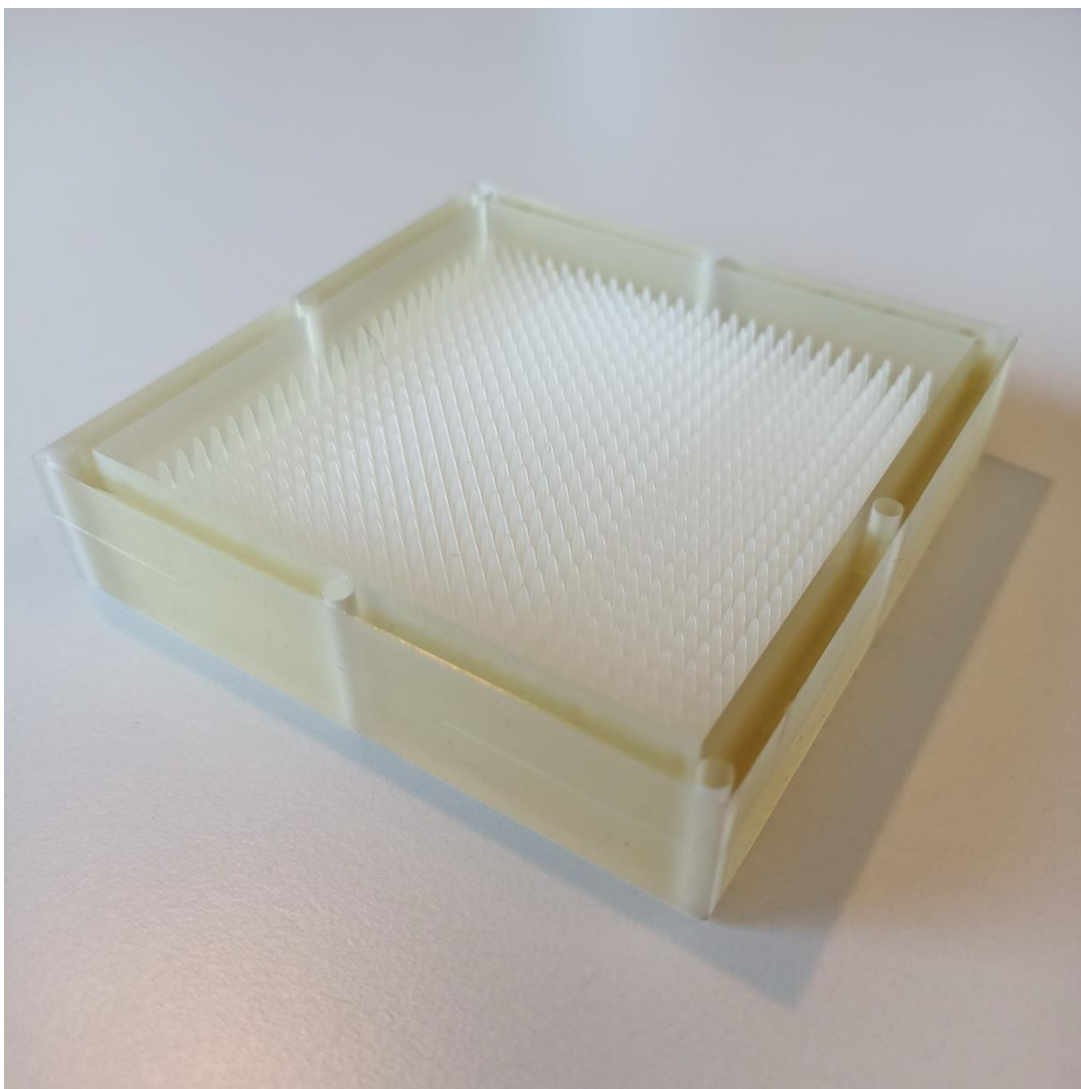


Extended Data Fig. 3

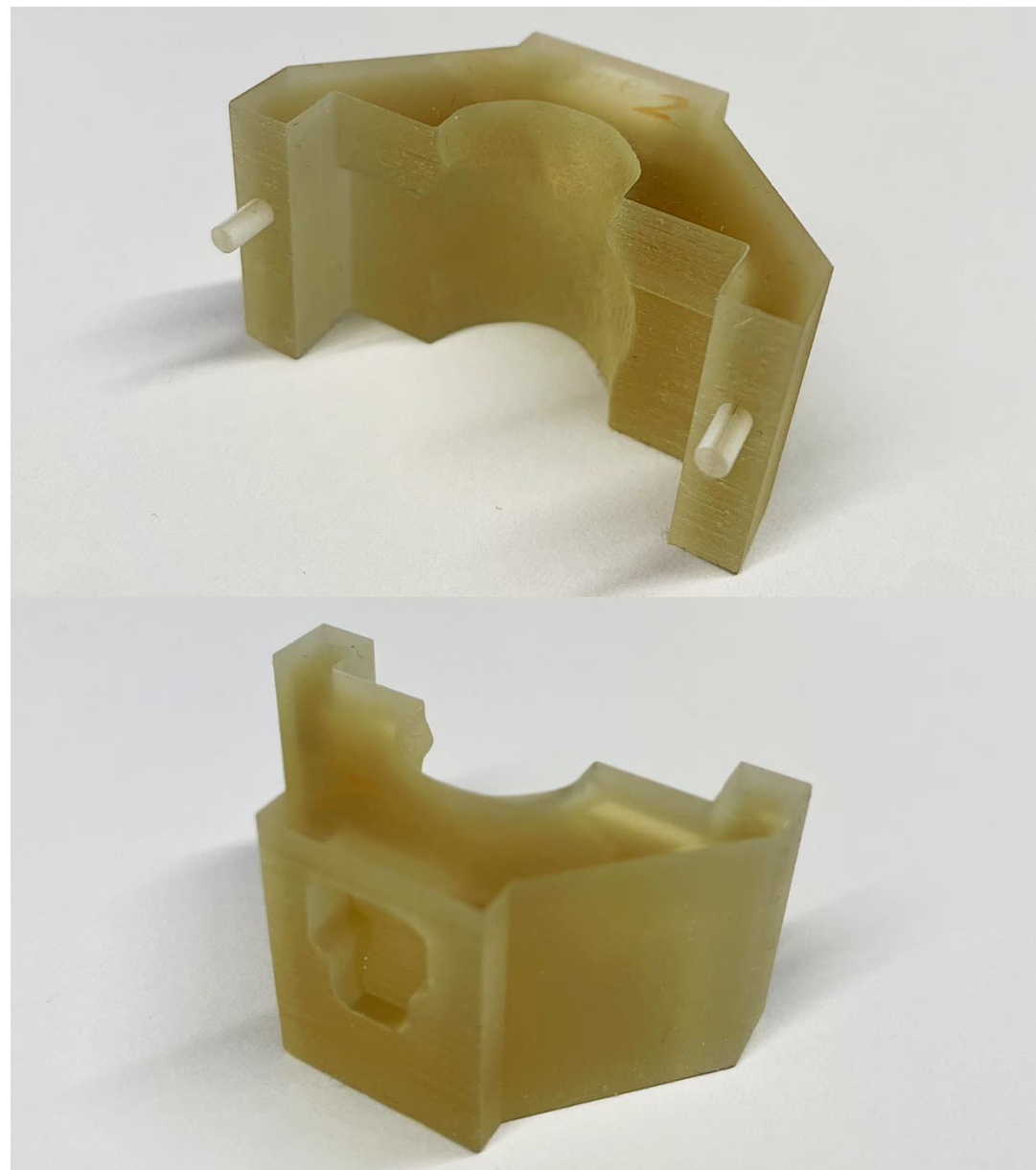


Extended Data Fig. 4

A

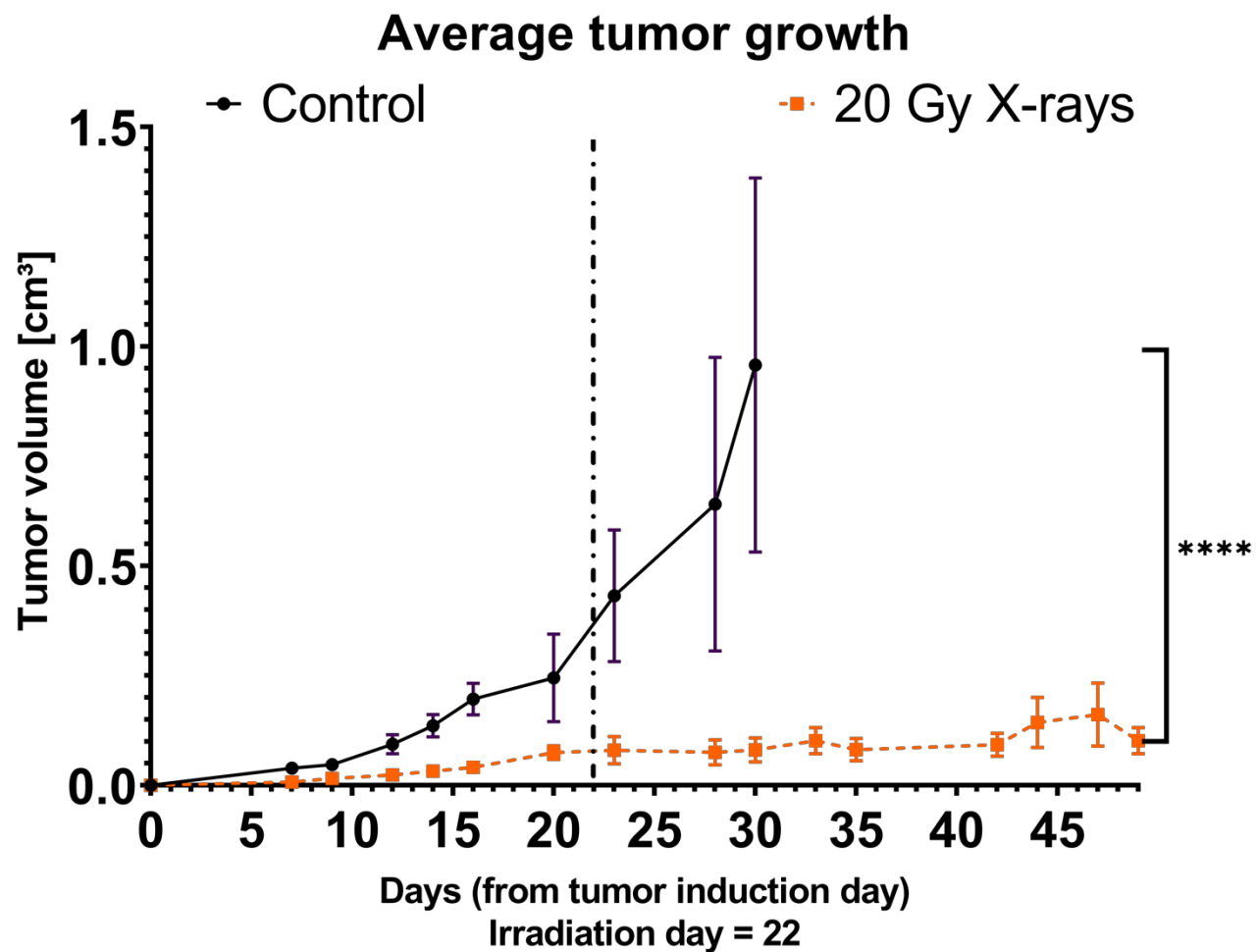


B



Extended Data Fig. 5

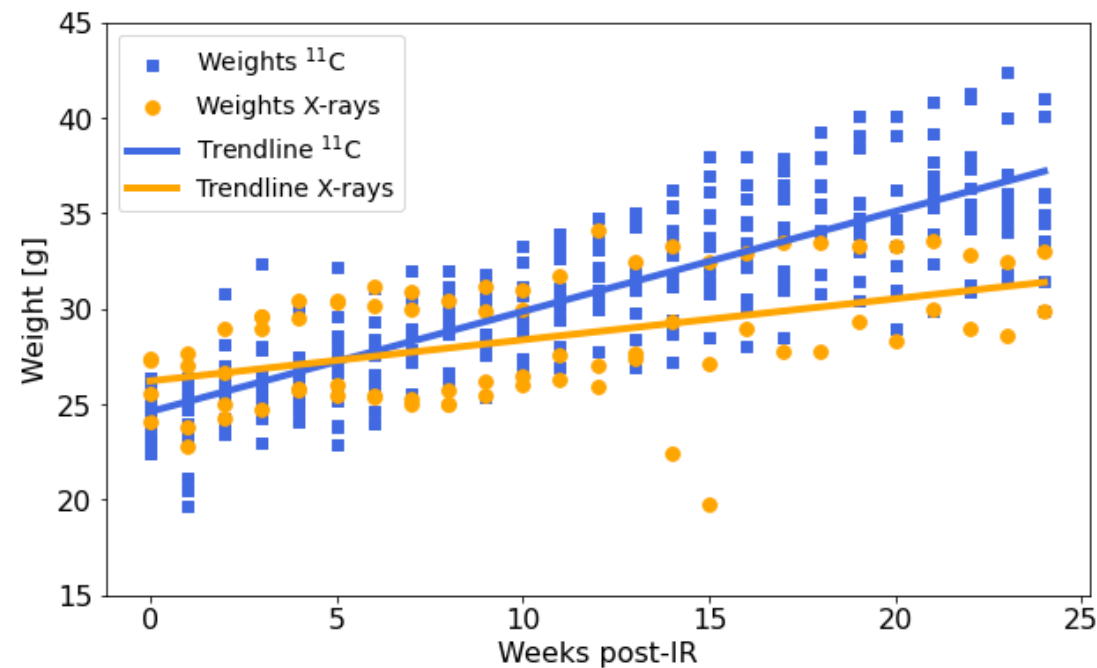
A



B



C

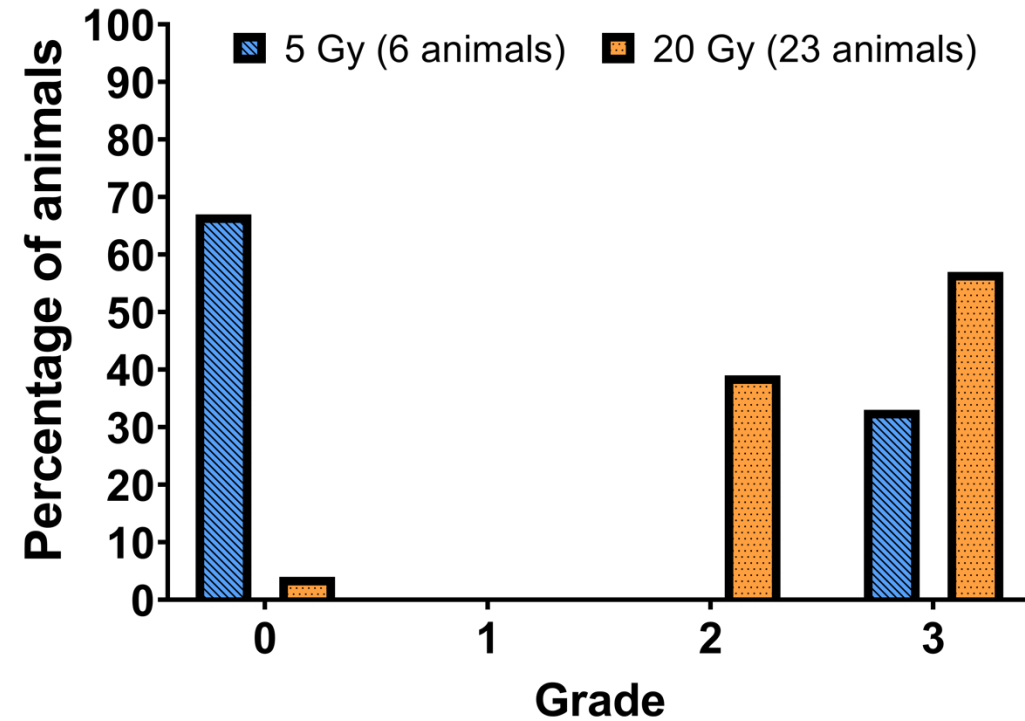


Extended Data Fig. 6



Skin toxicity scoring

Grade 5	Necrosis
Grade 4	Open wound not healing, leading to sacrifice of the animal
Grade 3	Closed wound or small scratch
Grade 2	Dry skin, desquamation
Grade 1	Redness
Grade 0	No effect



Extended Data Fig. 7



Supplementary material

Supplementary Figures

Supplementary Figure 1. PET images of individual mice. Measured activity for all irradiated mice. All images show the final activity. For the time-dependent images, see [Supplementary video 1](#).

Supplementary Figure 2. Grip strength test of individual mice. Grip test ([Extended data Fig. 6](#)) was performed every 2 weeks up to 6 months post-irradiation. **A.** Sham-irradiated mice. All data were used to calculate median grip performance and fraction of time points with $F < 100$ N shown in [Fig. 5](#). **B.** Irradiated mice. Here only data from week 6 were used to calculate median grip strength and fraction of time points with $F < 100$ N, considering that myelopathy has a latency of at least one month. Bars are standard deviations on three separate measurements for each mouse.

Supplementary Figure 3. Washout in individual mice. Washout data for all mice exposed to either 5 or 20 Gy ^{11}C -ions. One mouse from the 5 Gy group was excluded from the analysis because parameters were $>3 \sigma$ far from the pooled data of the others.

Supplementary videos

Supplementary video 1. ^{11}C activity in irradiated mouse. Real-time build-up of the PET signal during mouse irradiation. The image is overlapped to the mouse CT in sagittal (left) and transversal (right) views. Time and dose are also indicated.

Supplementary video 2. X-ray toxicity. Example of kyphosis (cervical myelopathy grade 3) in a mouse treated with 20 Gy X-rays (left). Tumor was controlled, but the neurotoxicity is clearly visible. A control mouse is shown on the right for comparison.

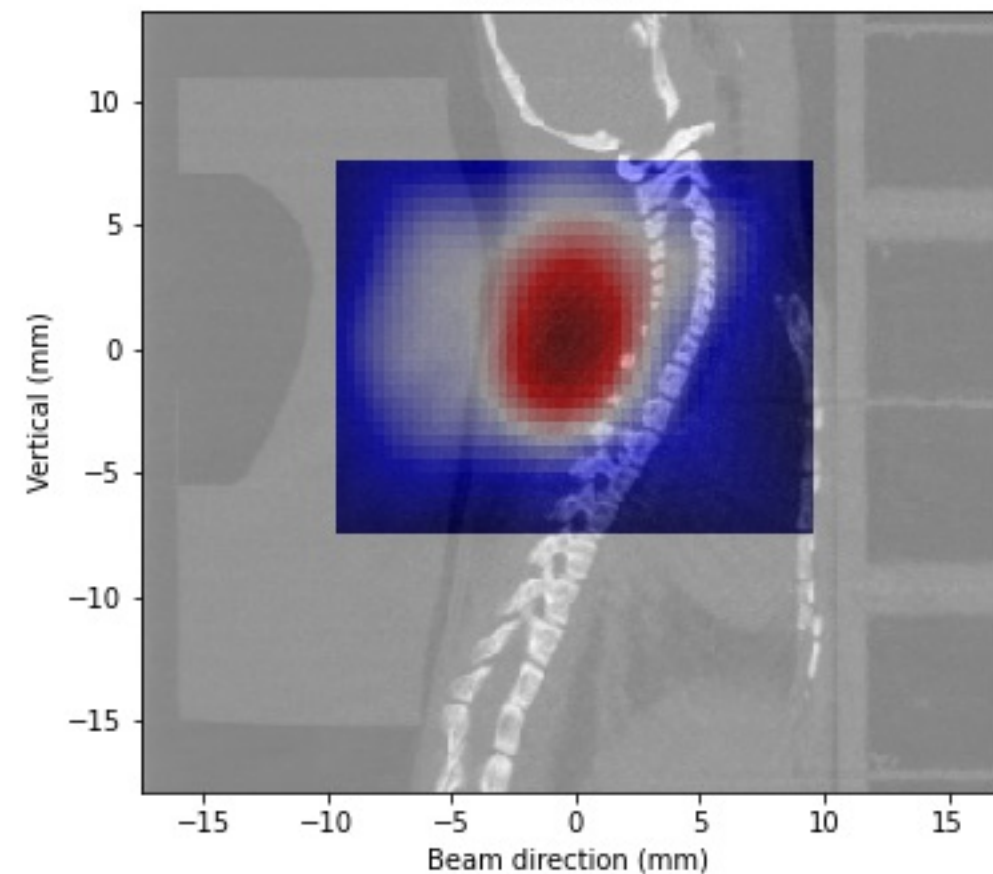
Supplementary video 3. Vascular structure of the tumor. 3D rendering of the vascular structure of the LM8 osteosarcoma tumor as visualized in μCT after staining with Vascupaint. Quantitative values are shown in the table.

Measurement time [s] = 210

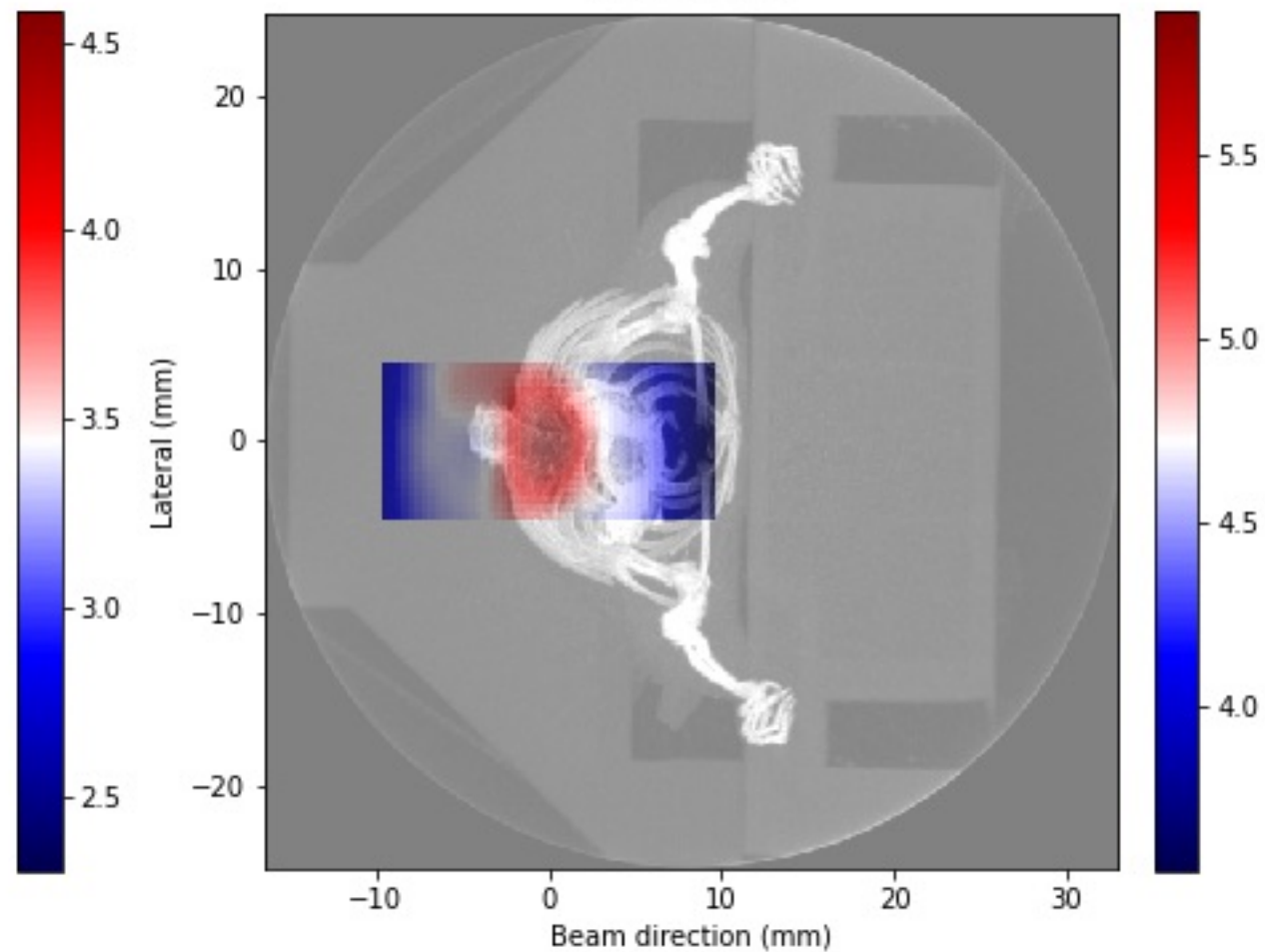
Beam on [s] = 150

Dose [Gy] = 2.50

Mouse: BA88.



Mouse: BA88.

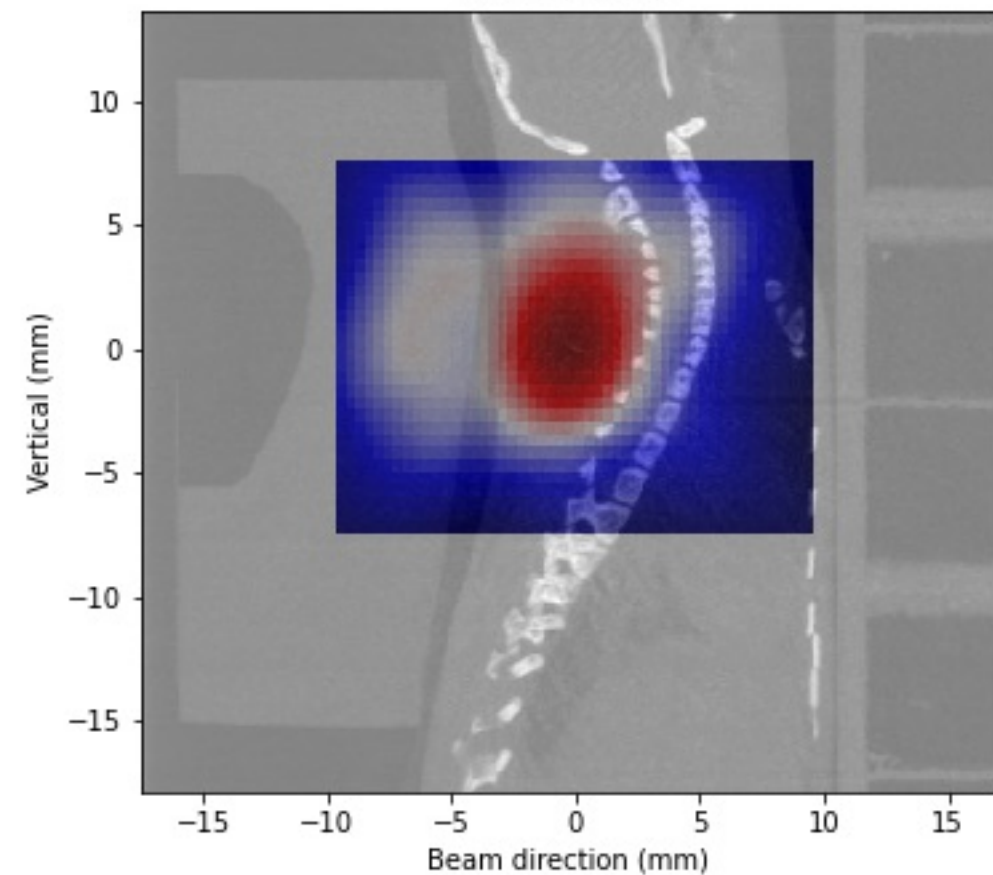


Measurement time [s] = 240

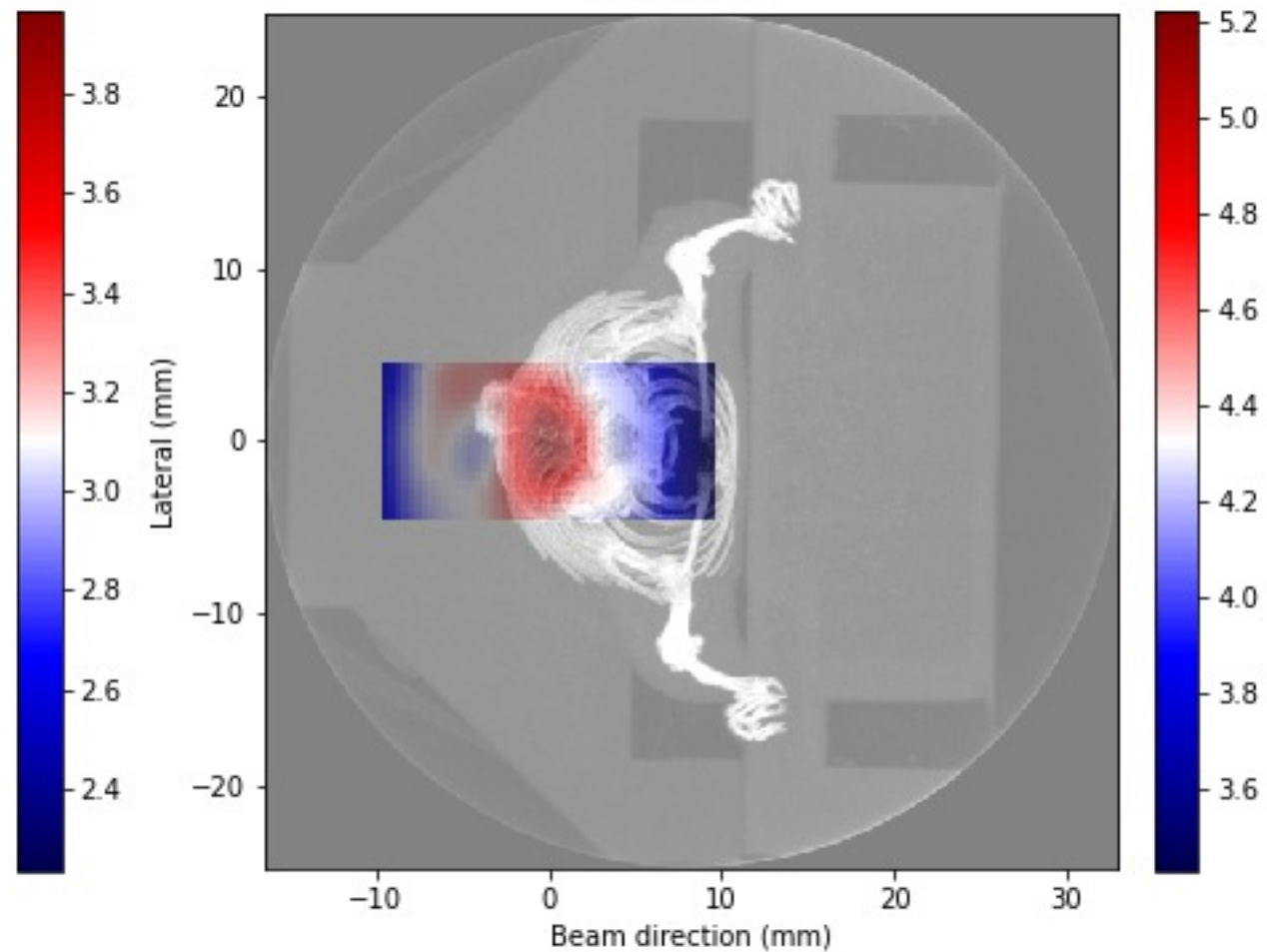
Beam on [s] = 180

Dose [Gy] = 3.00

Mouse: BA93.



Mouse: BA93.

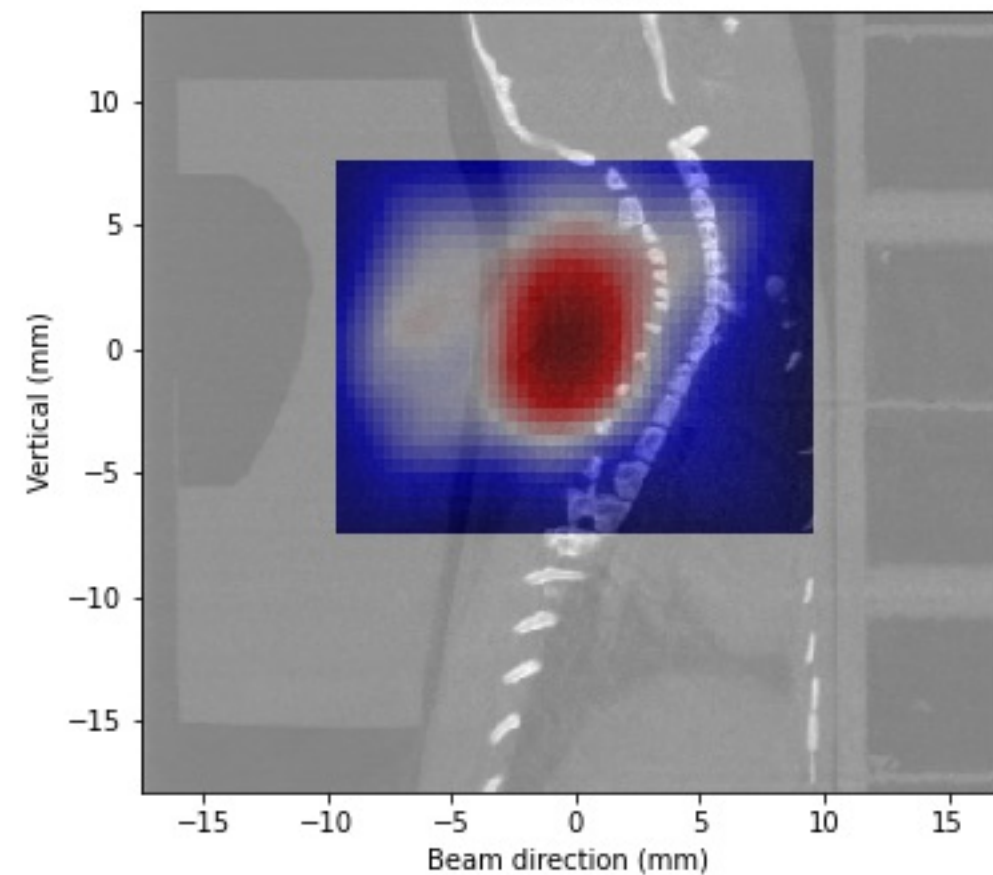


Measurement time [s] = 240

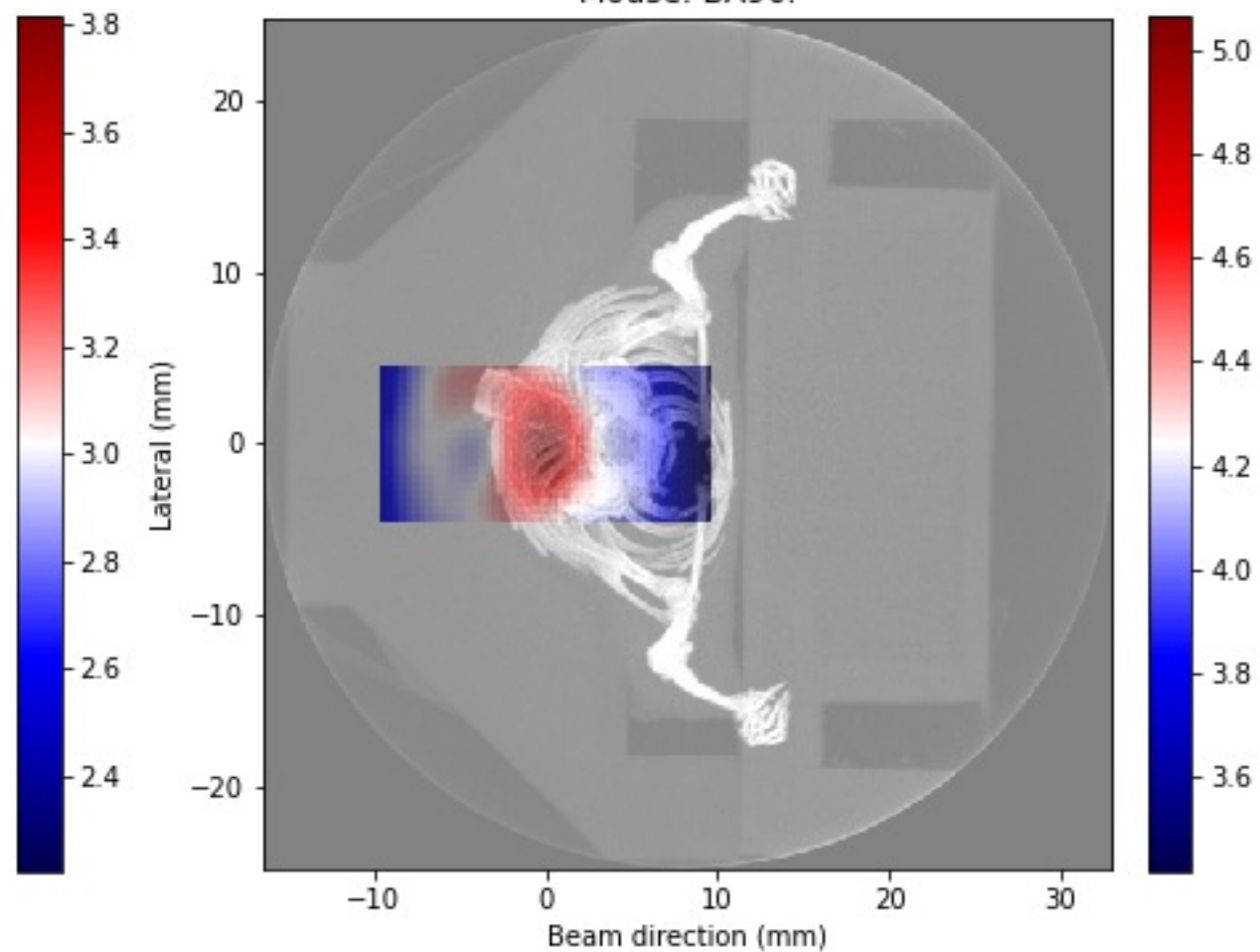
Beam on [s] = 180

Dose [Gy] = 3.00

Mouse: BA96.



Mouse: BA96.

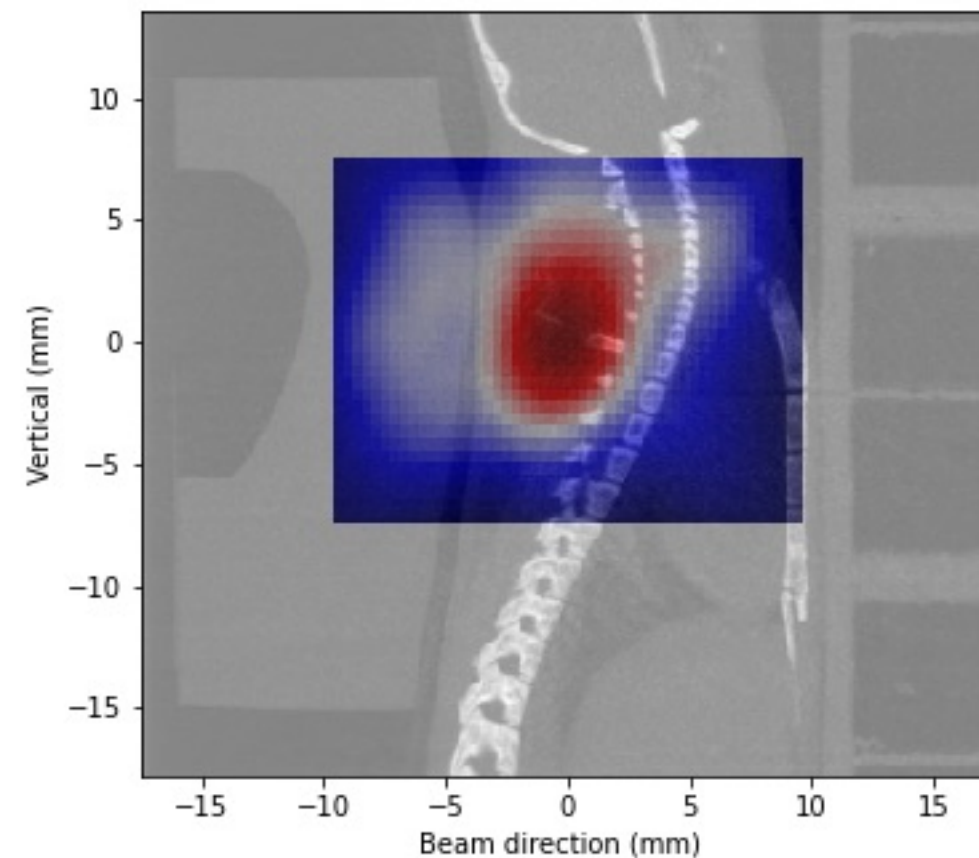


Measurement time [s] = 240

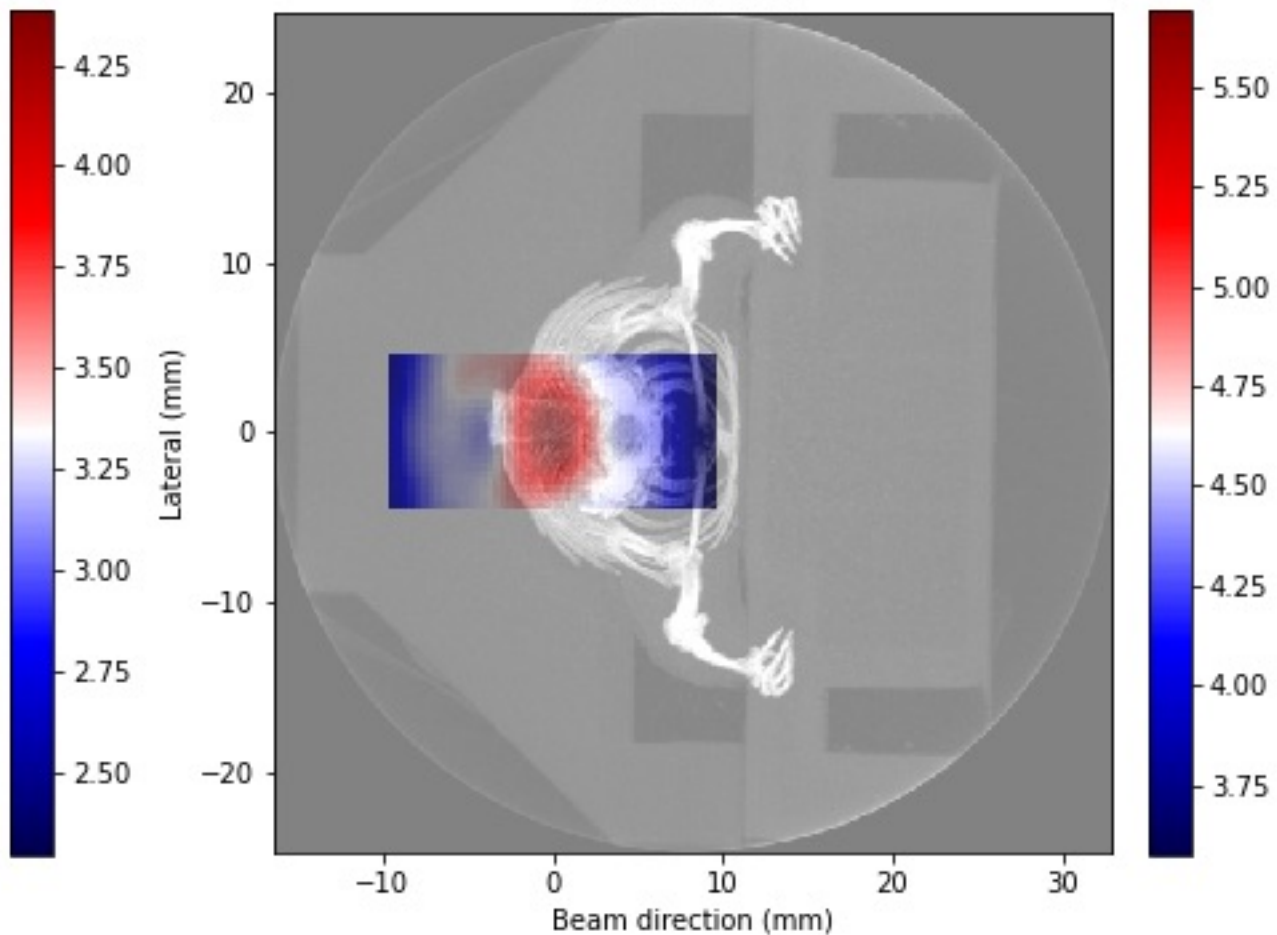
Beam on [s] = 180

Dose [Gy] = 3.00

Mouse: BA99.



Mouse: BA99.

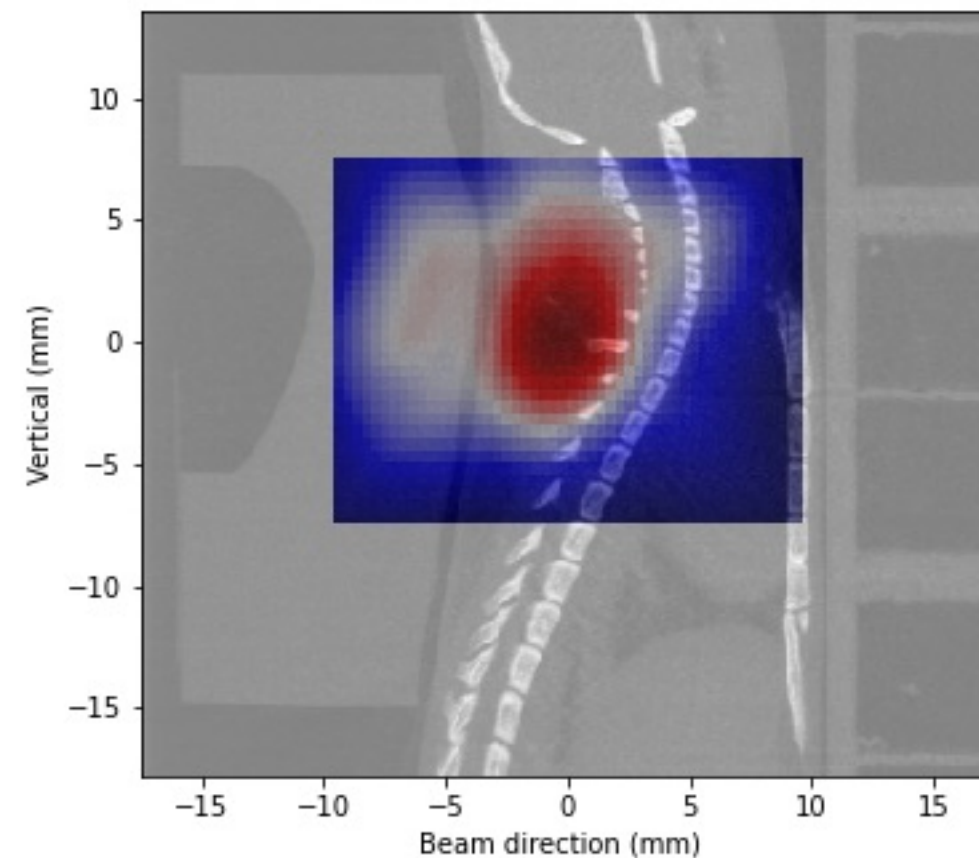


Measurement time [s] = 240

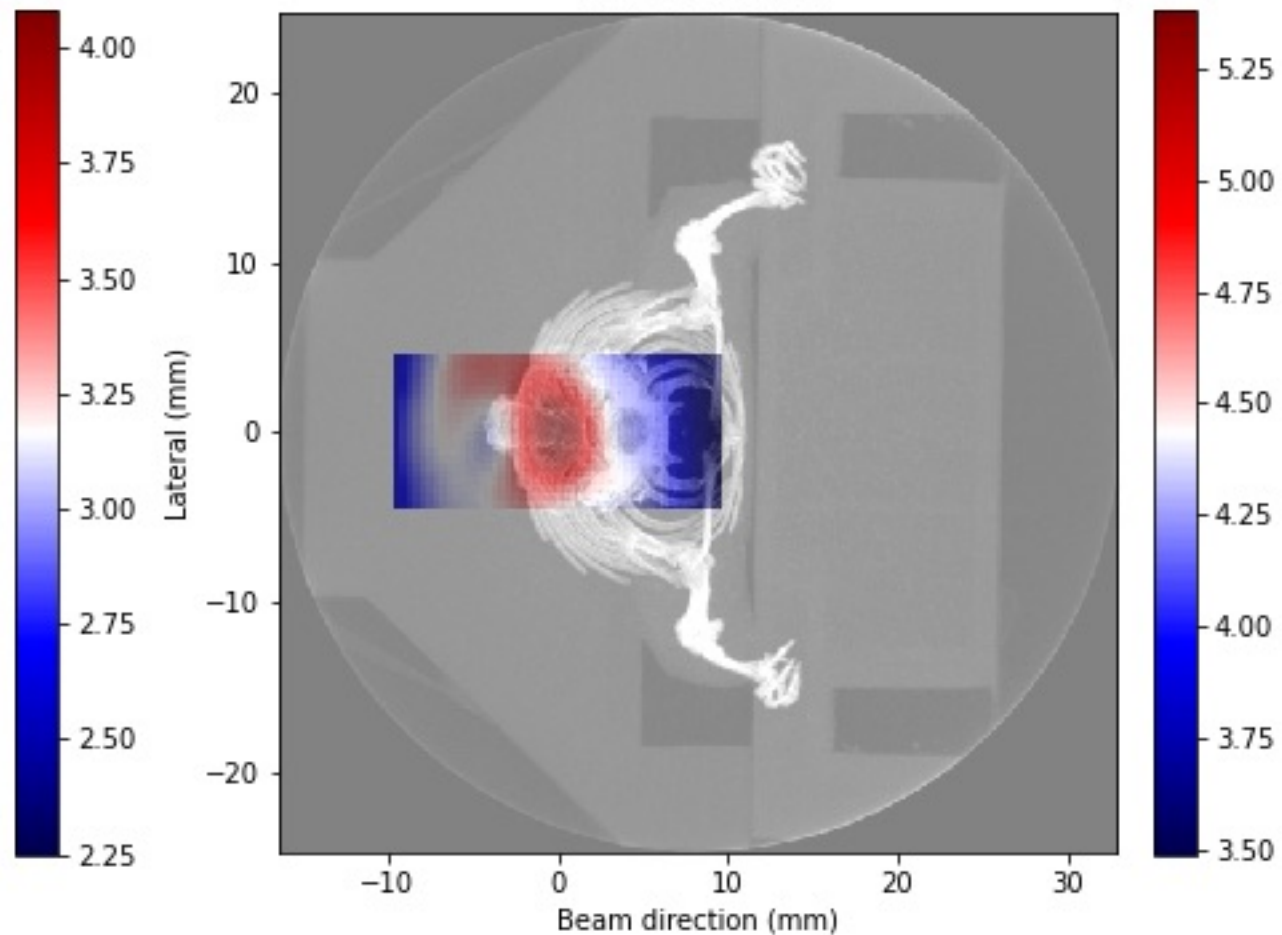
Beam on [s] = 180

Dose [Gy] = 3.00

Mouse: BA100.



Mouse: BA100.



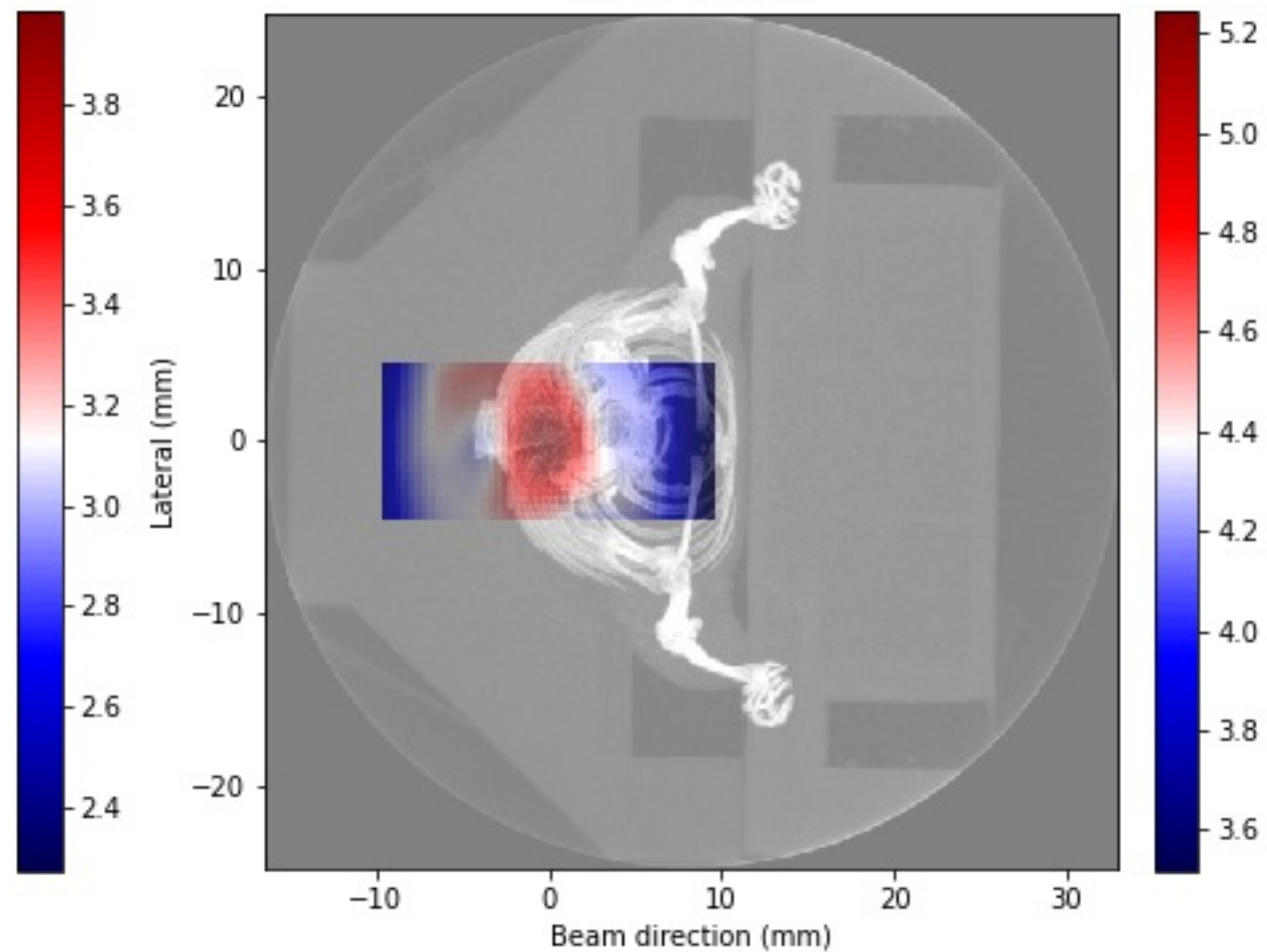
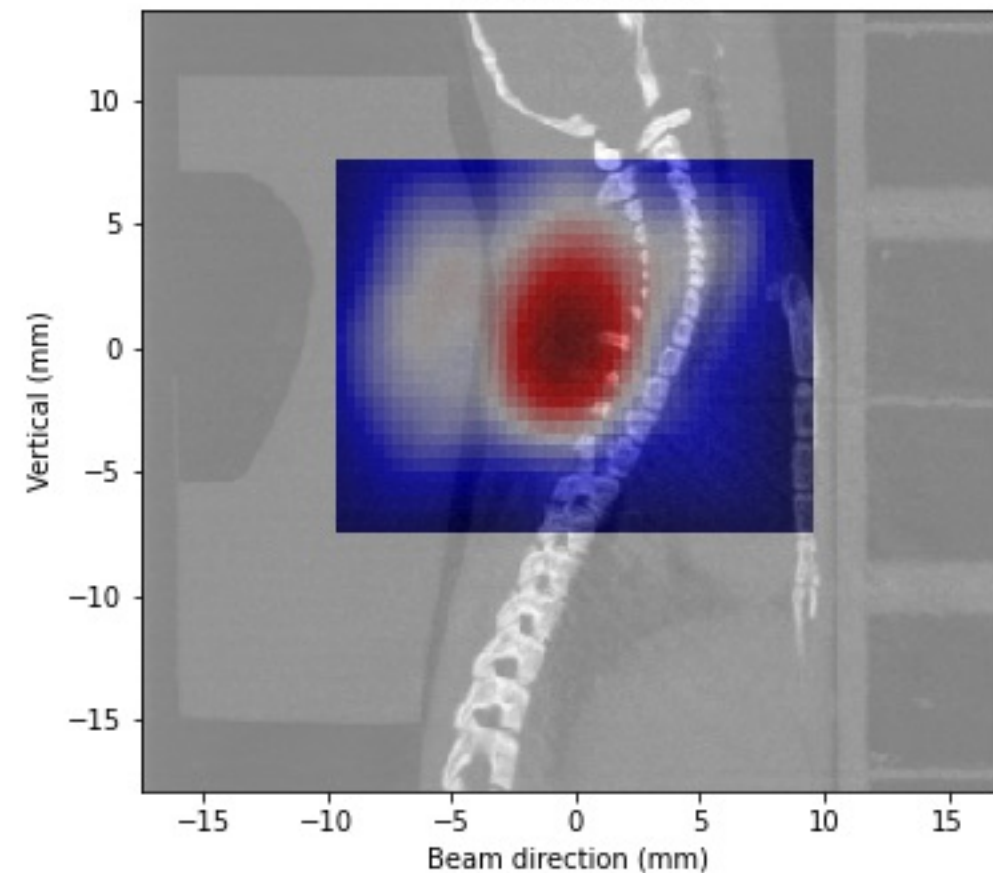
Measurement time [s] = 240

Beam on [s] = 180

Dose [Gy] = 3.00

Mouse: BA101.

Mouse: BA101.



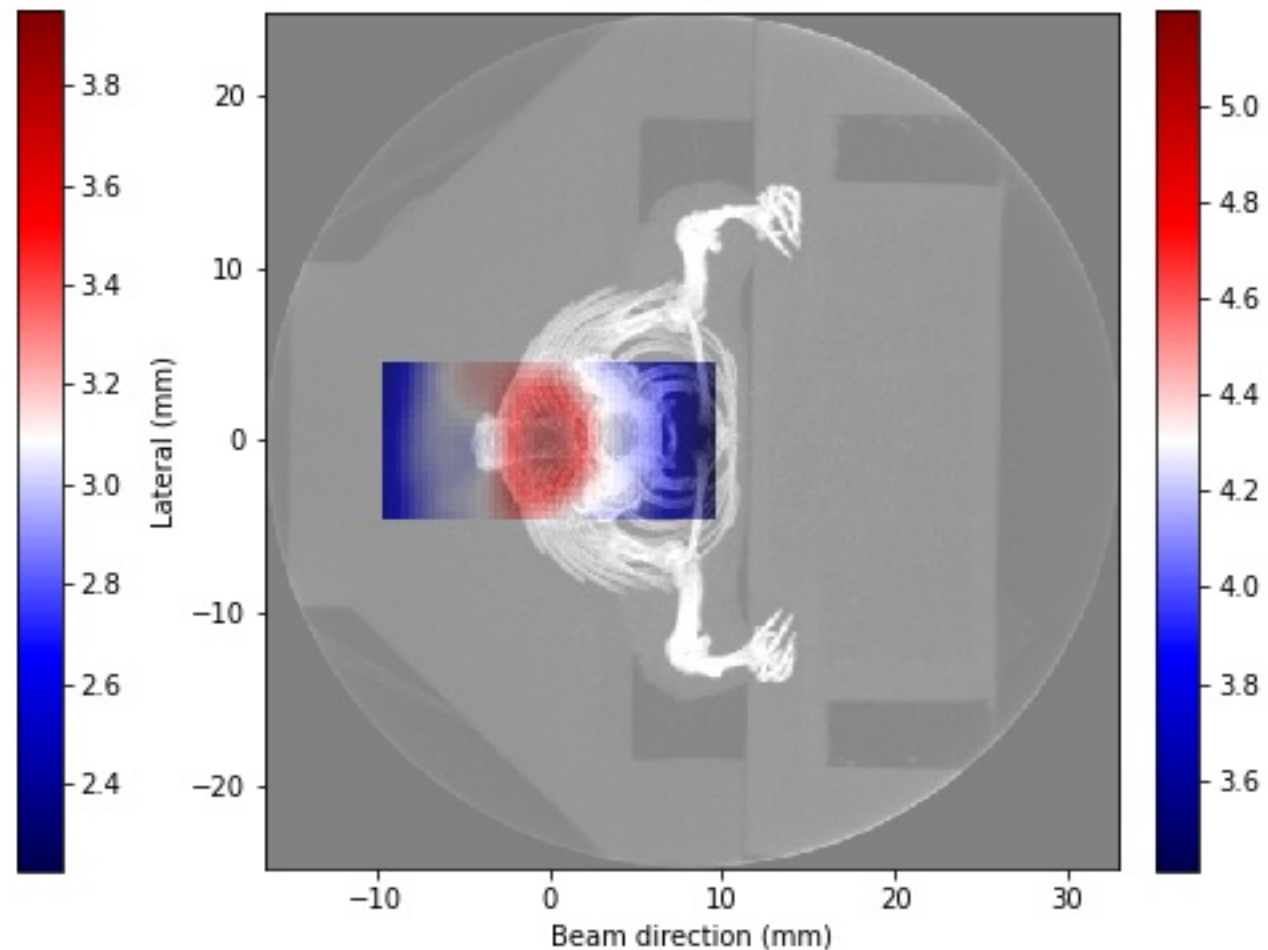
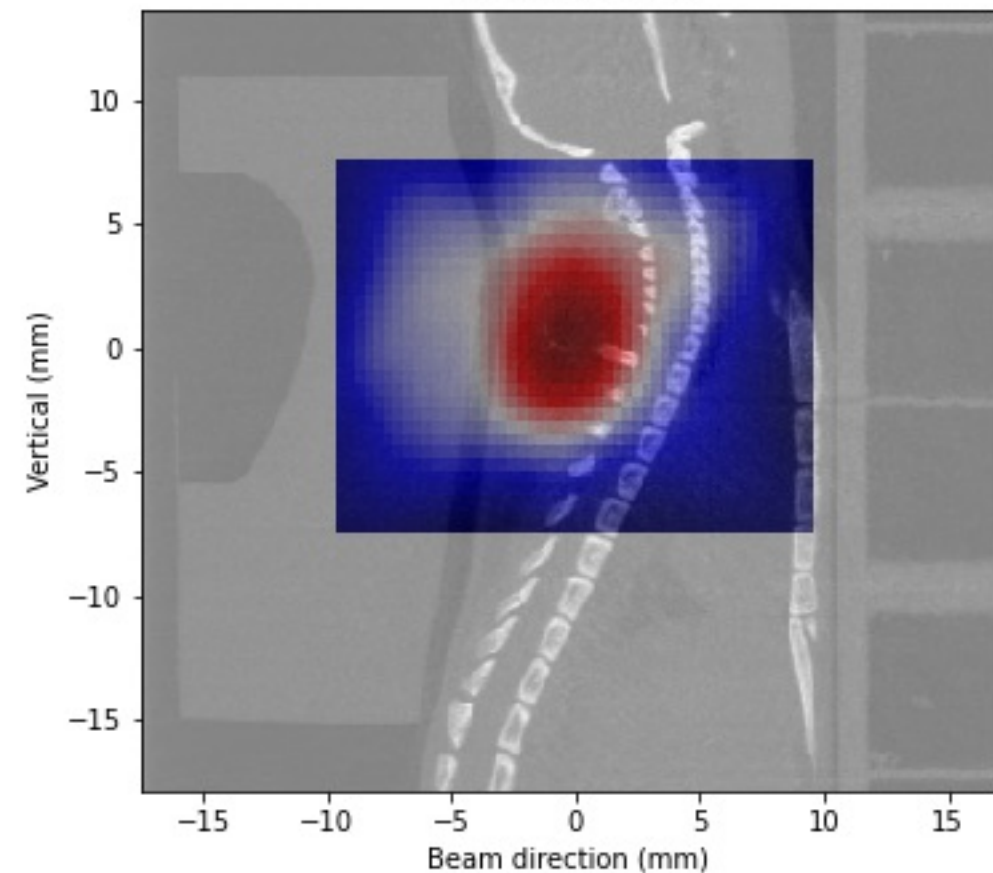
Measurement time [s] = 240

Beam on [s] = 180

Dose [Gy] = 3.00

Mouse: BA108.

Mouse: BA108.

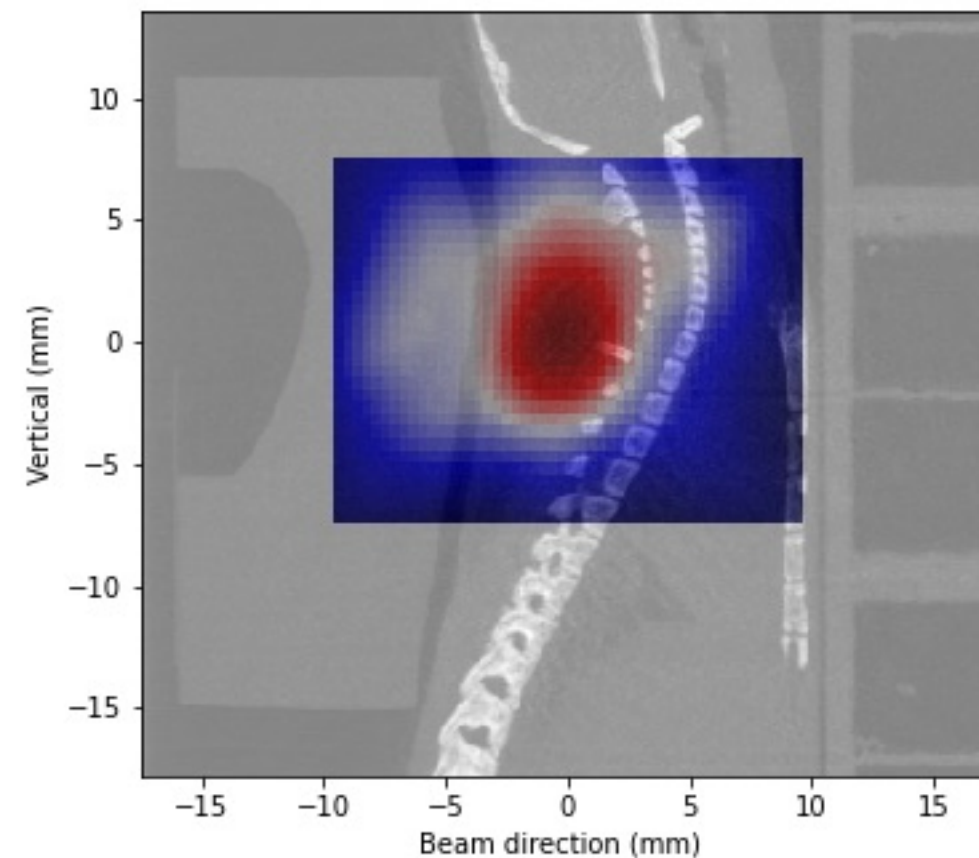


Measurement time [s] = 270

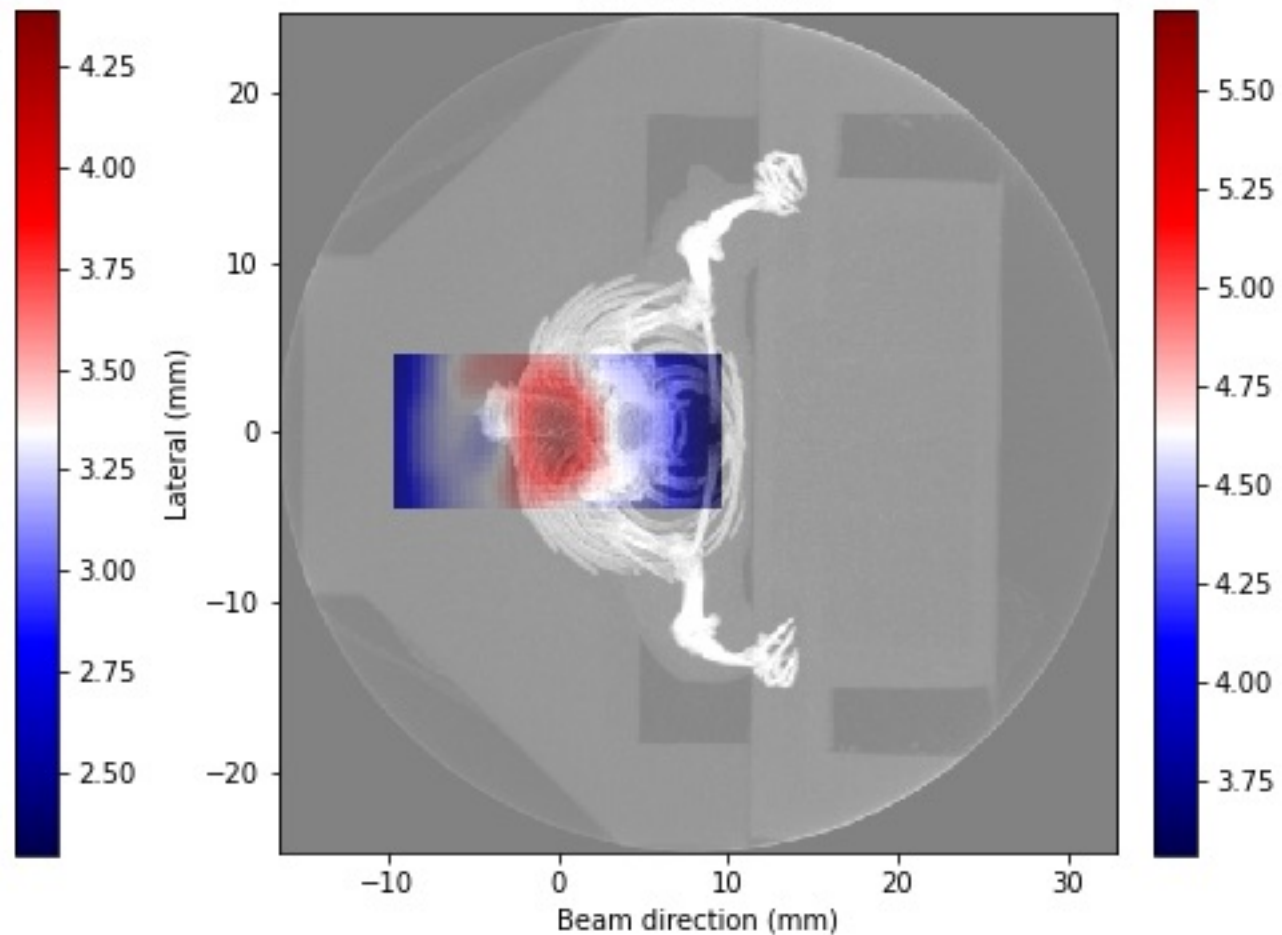
Beam on [s] = 210

Dose [Gy] = 3.50

Mouse: BA119.



Mouse: BA119.

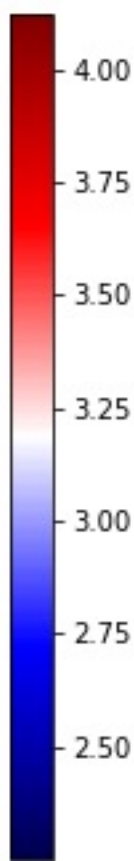
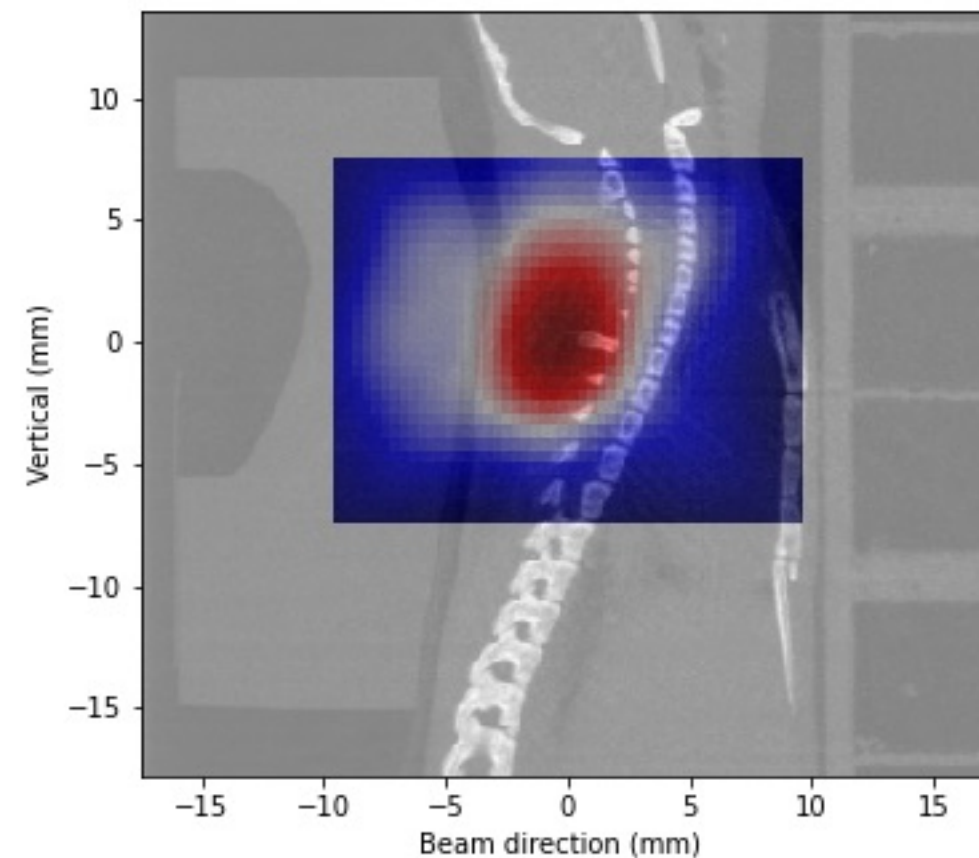


Measurement time [s] = 240

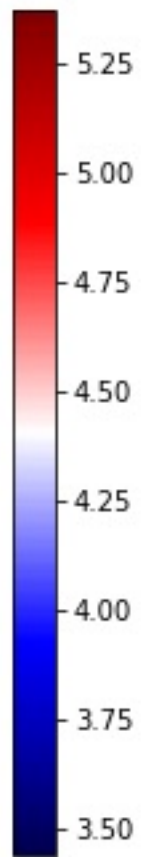
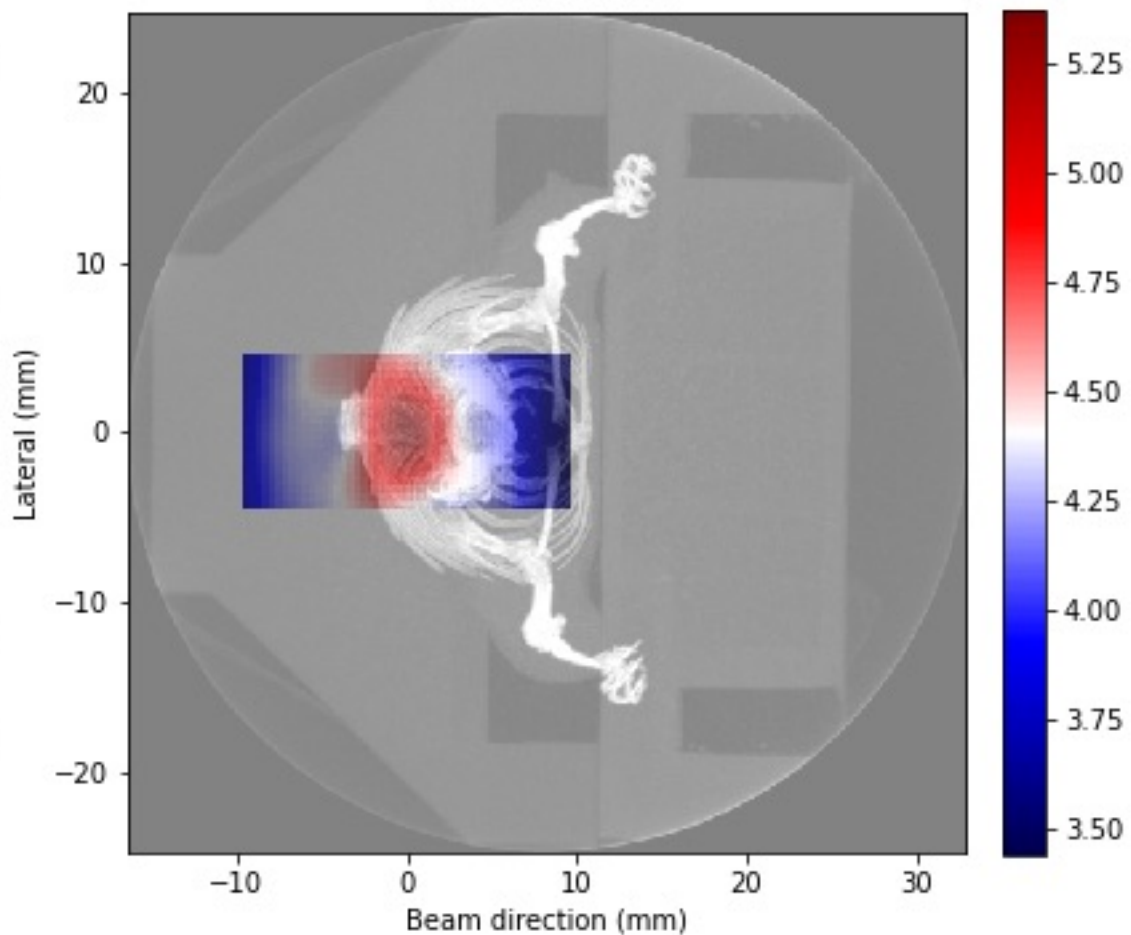
Beam on [s] = 180

Dose [Gy] = 3.00

Mouse: BA120.



Mouse: BA120.



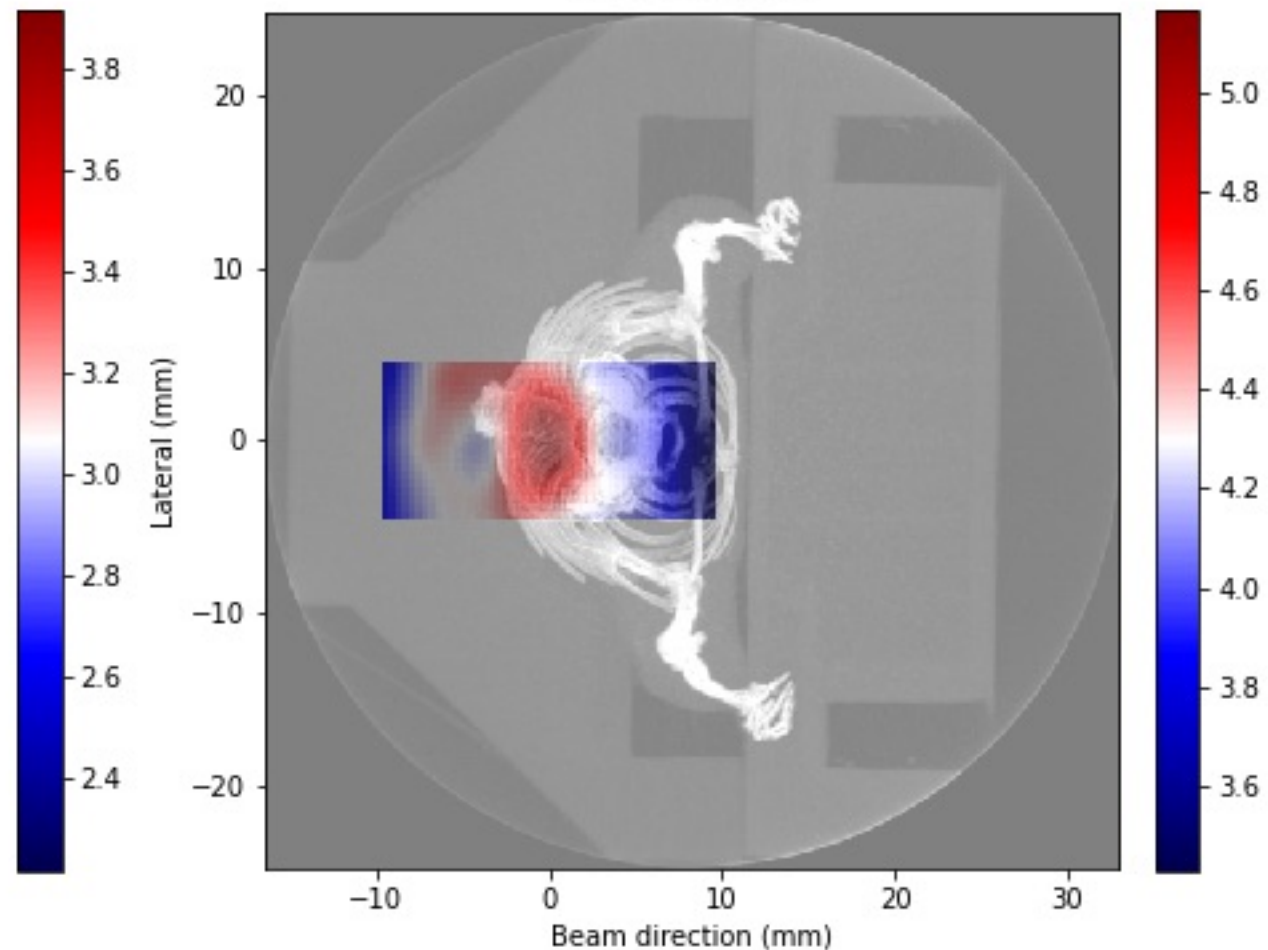
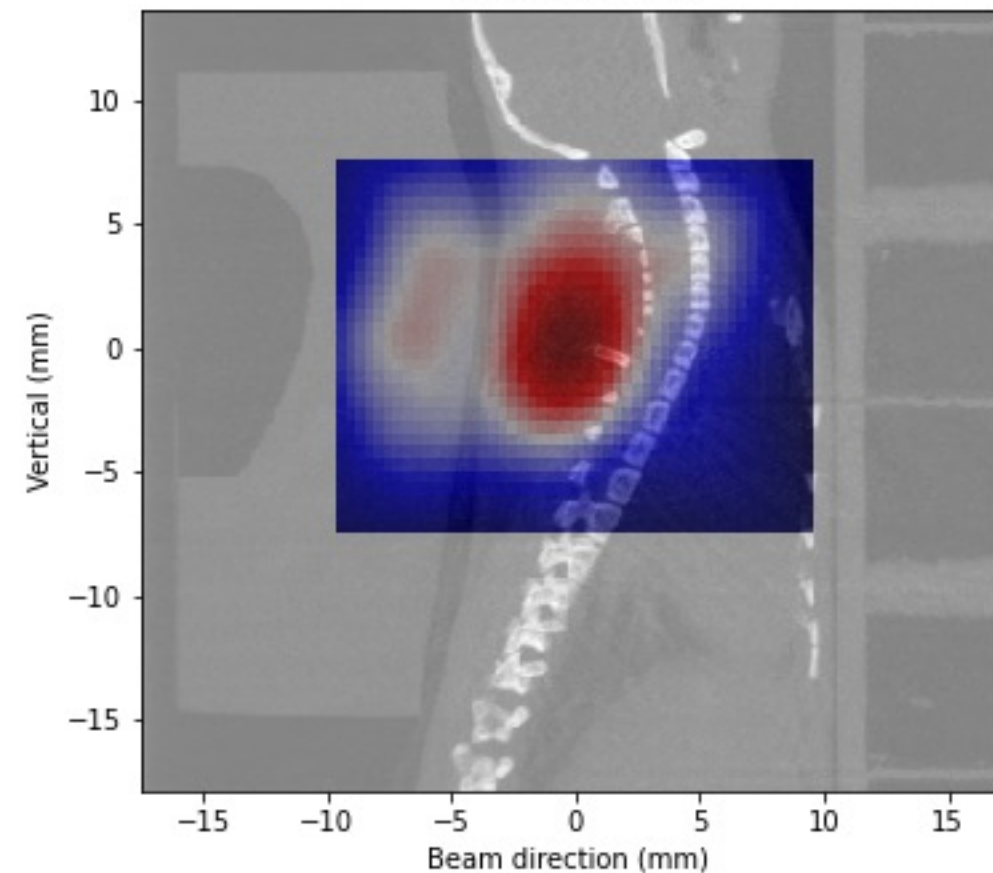
Measurement time [s] = 330

Beam on [s] = 270

Dose [Gy] = 4.50

Mouse: BA125.

Mouse: BA125.



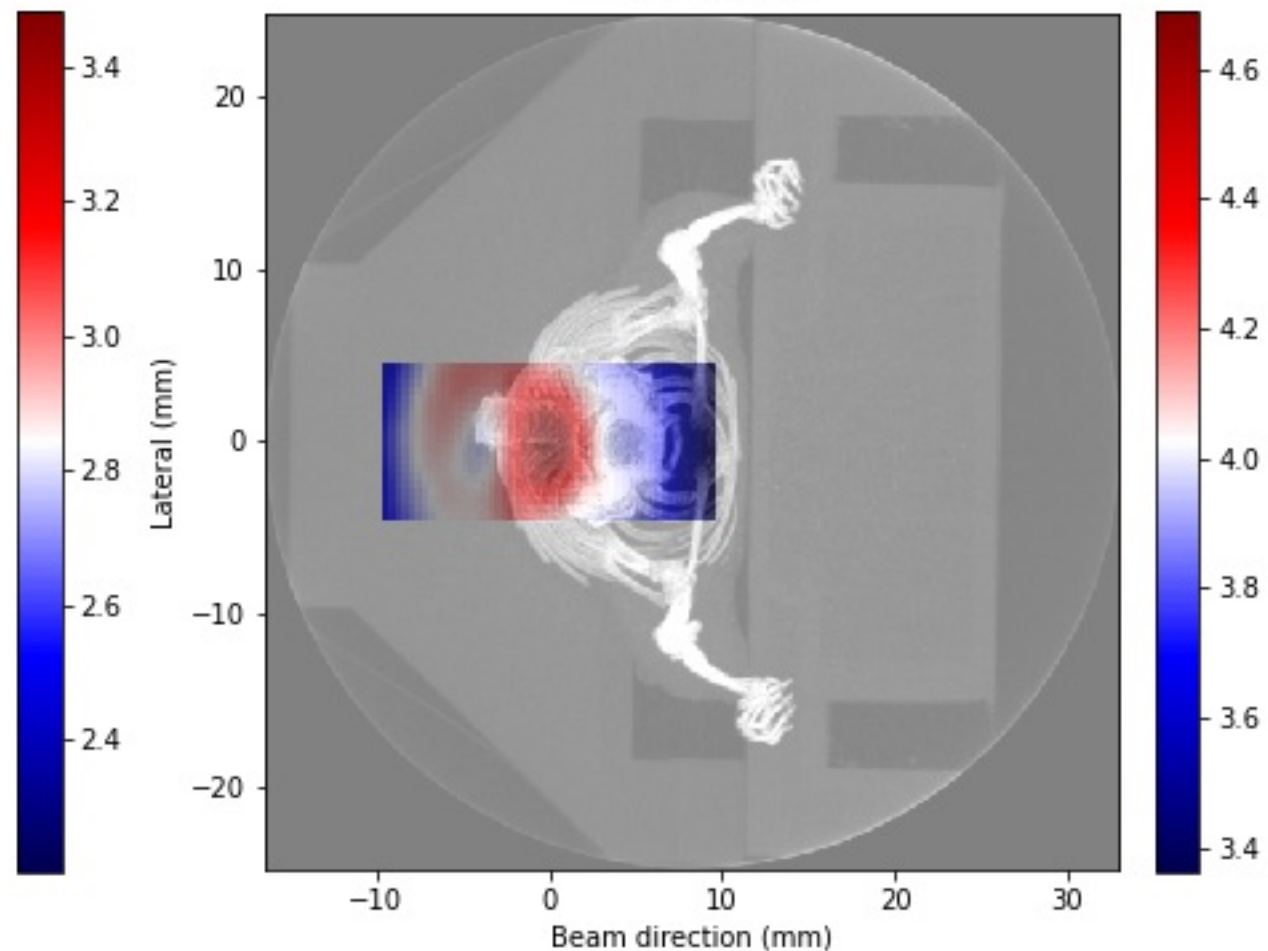
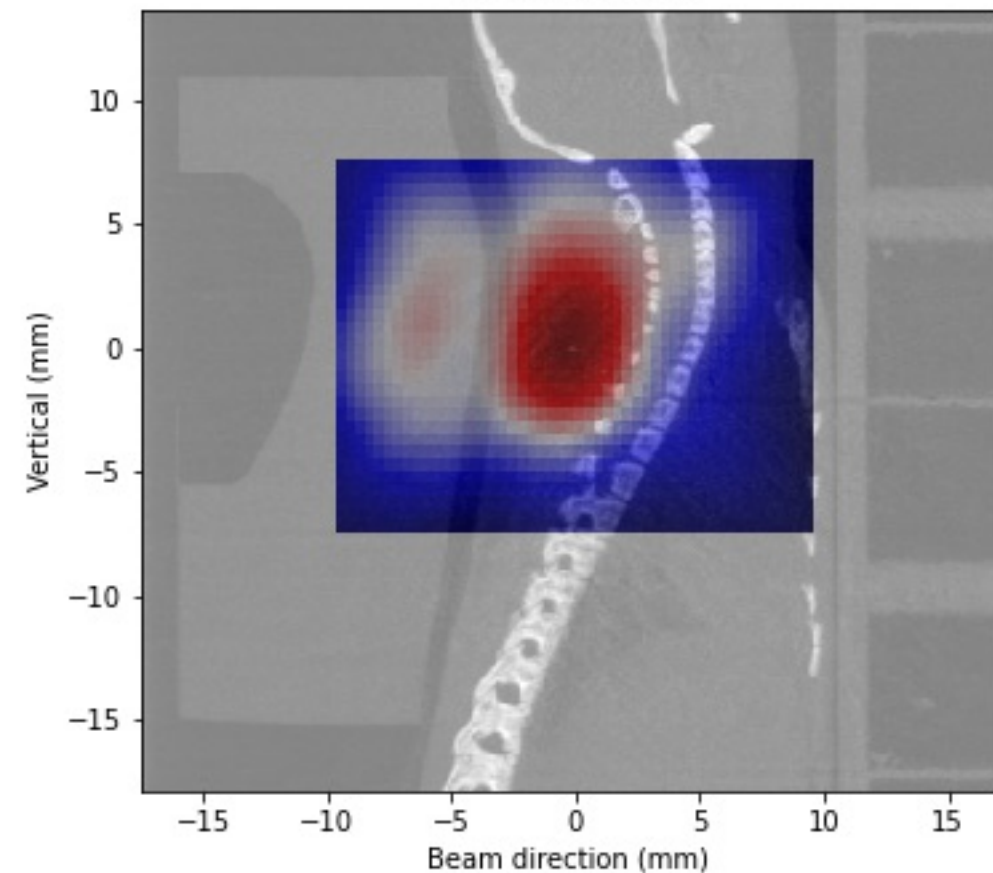
Measurement time [s] = 240

Beam on [s] = 180

Dose [Gy] = 3.00

Mouse: BA126.

Mouse: BA126.

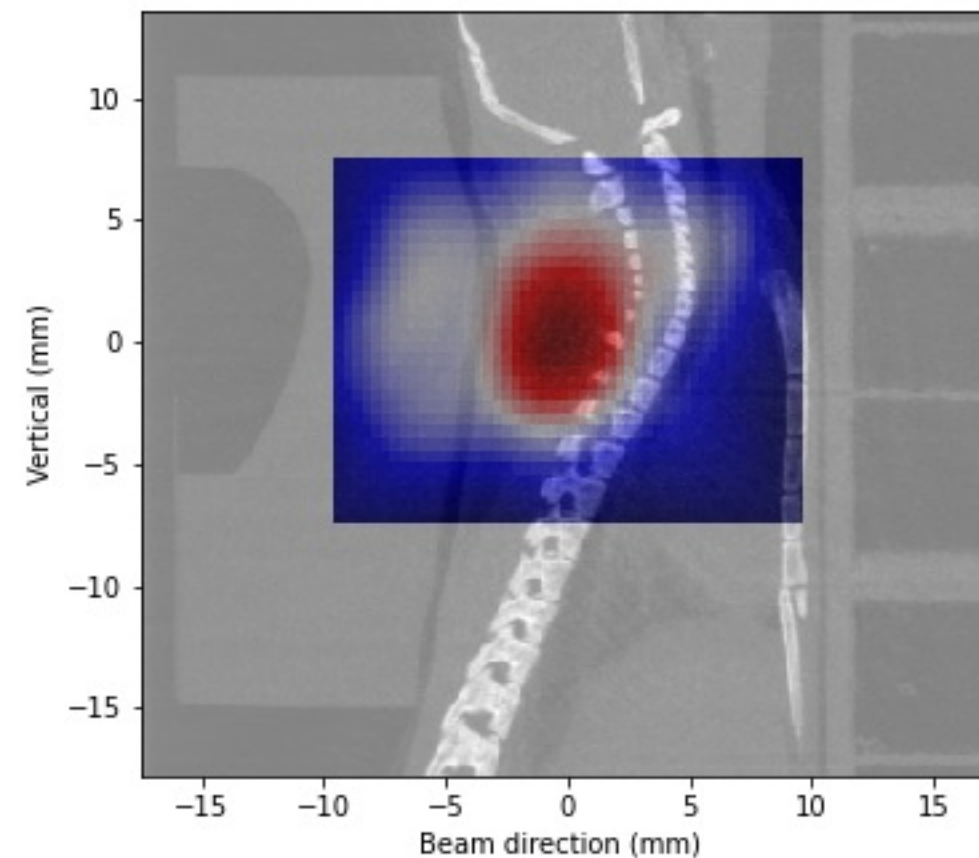


Measurement time [s] = 240

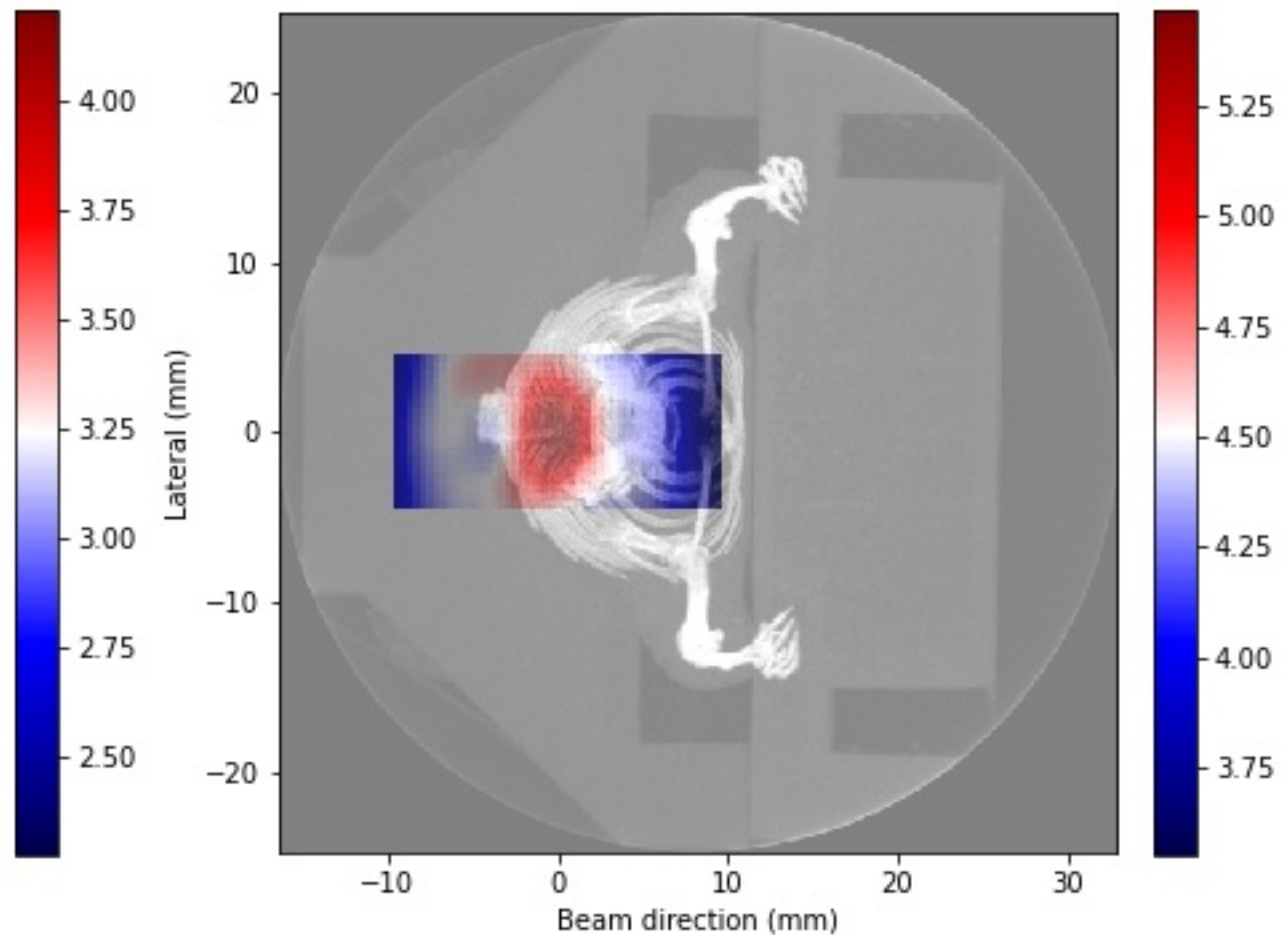
Beam on [s] = 180

Dose [Gy] = 3.00

Mouse: BA129.



Mouse: BA129.

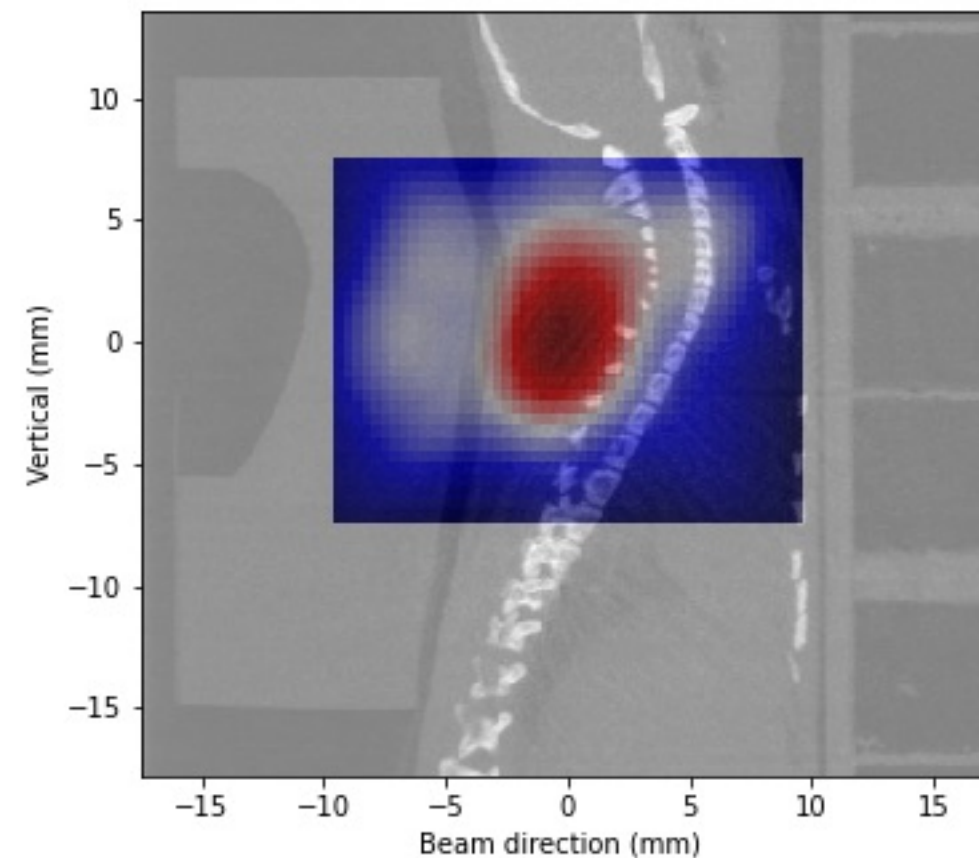


Measurement time [s] = 240

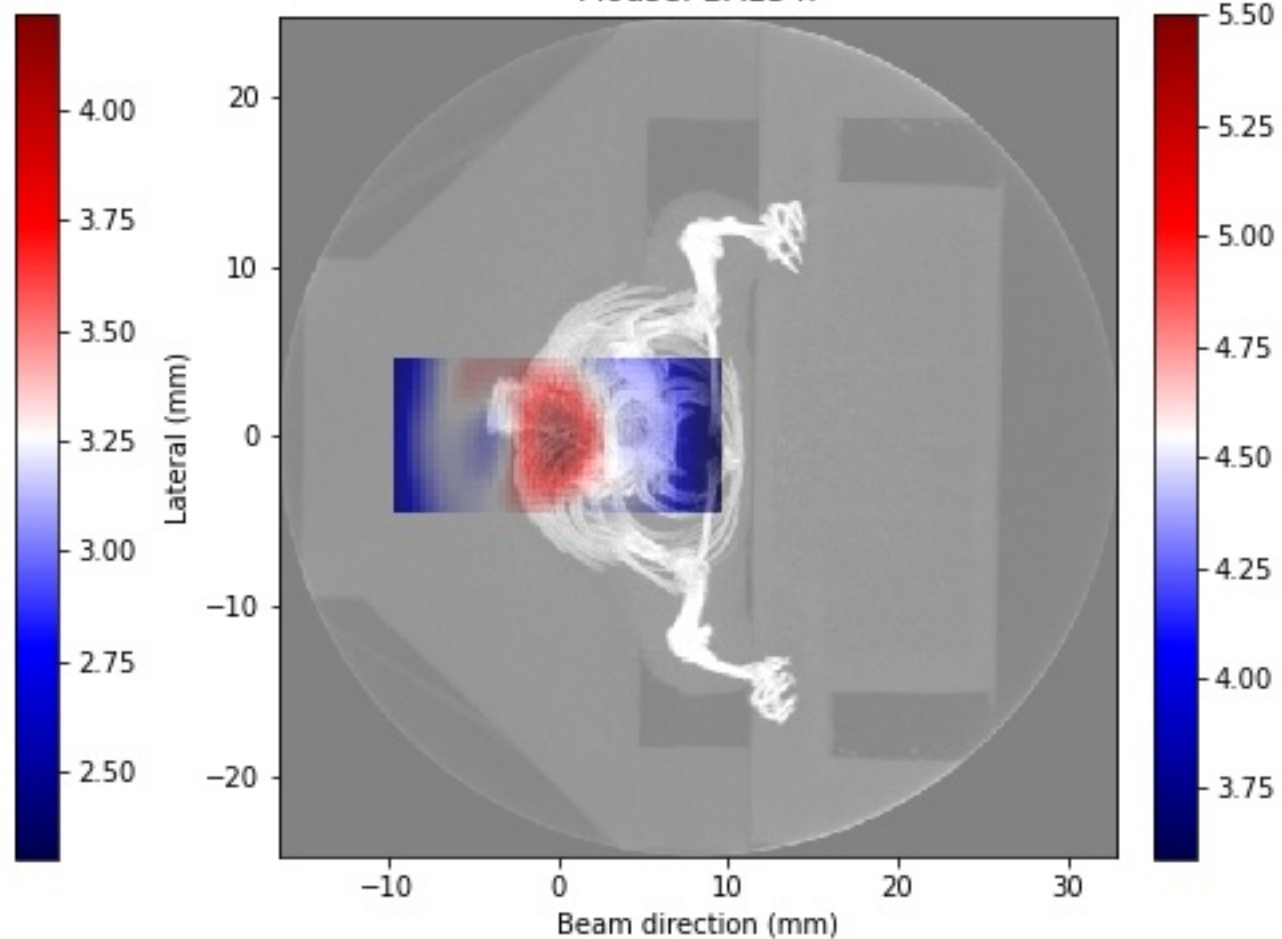
Beam on [s] = 180

Dose [Gy] = 3.00

Mouse: BA134.

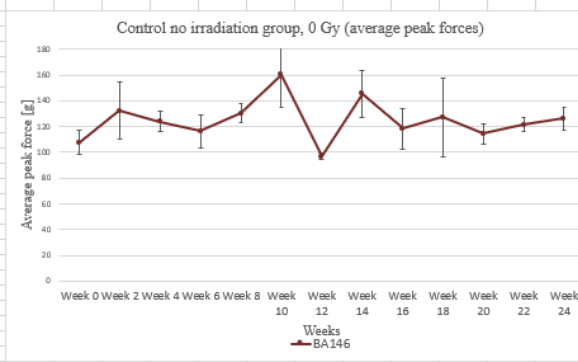
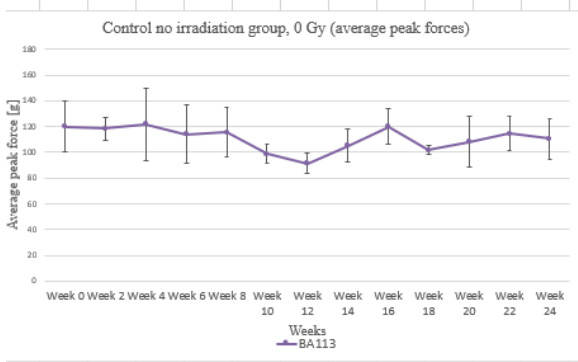
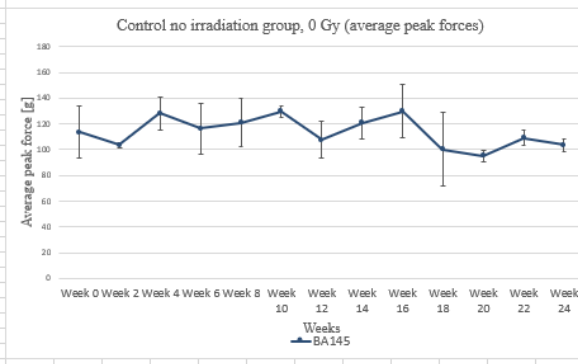
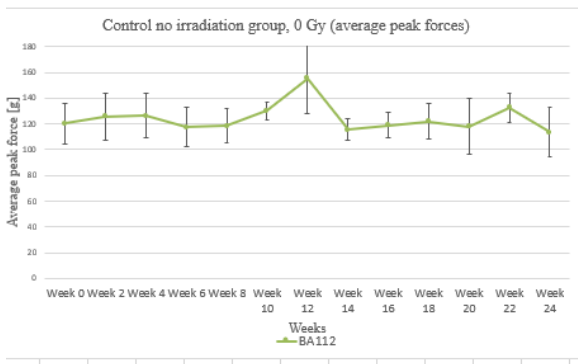
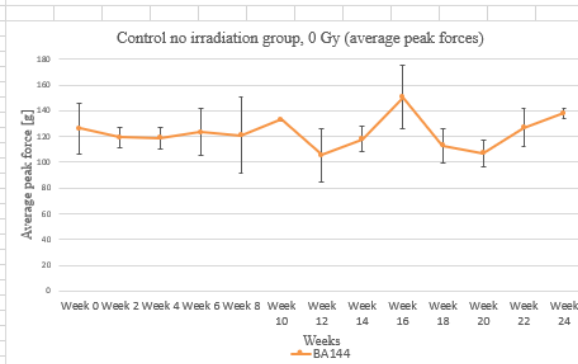
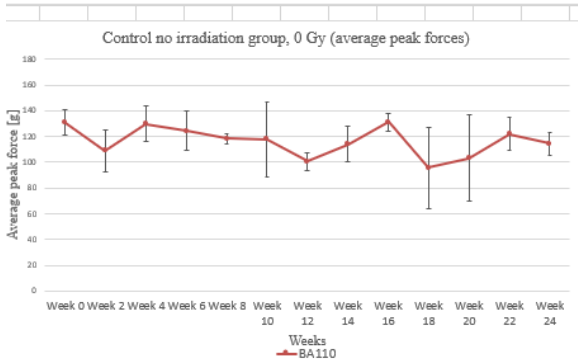
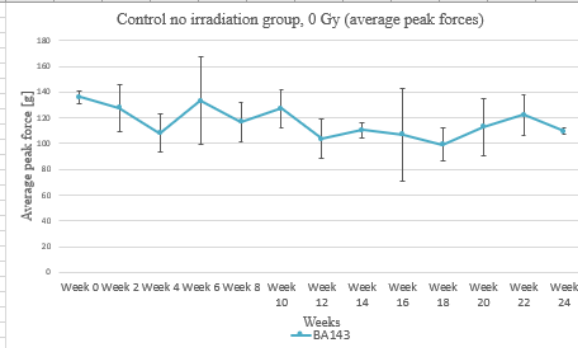
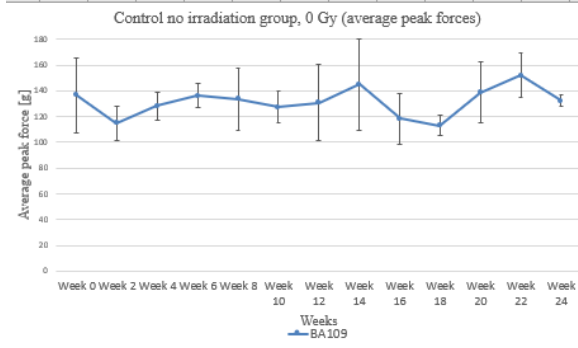


Mouse: BA134.



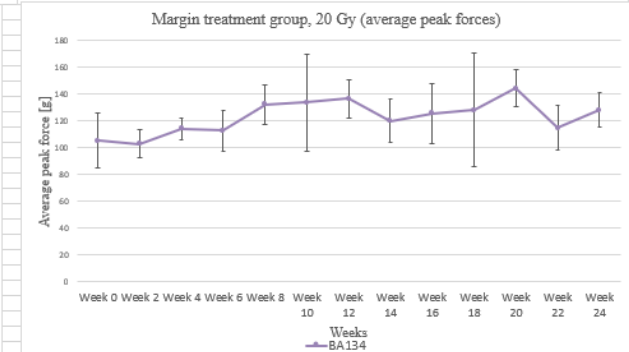
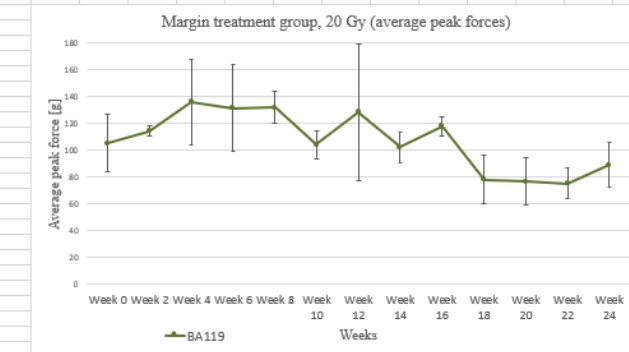
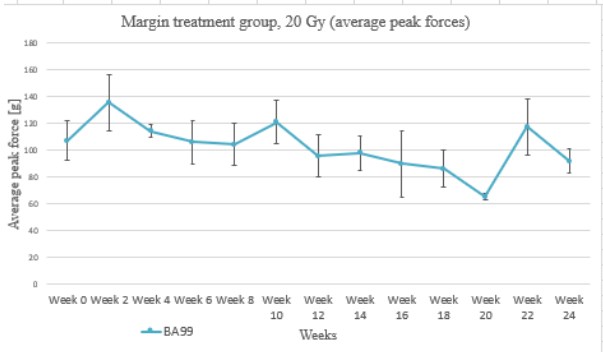
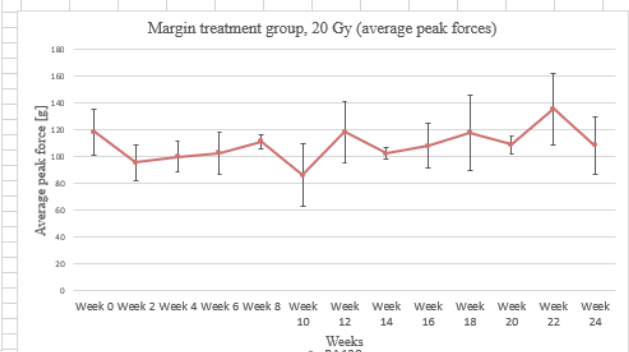
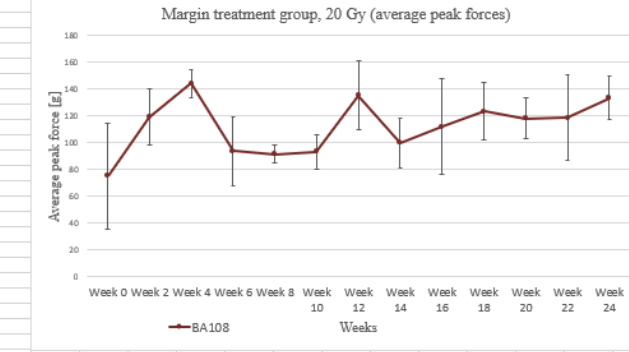
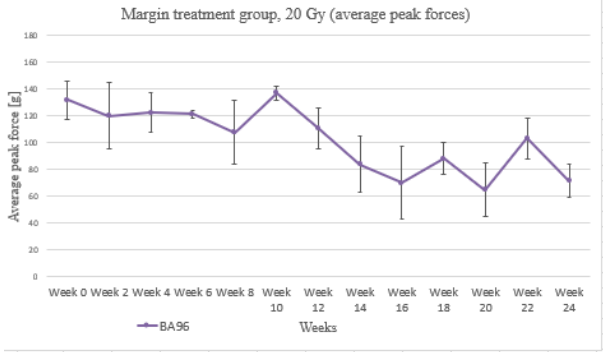
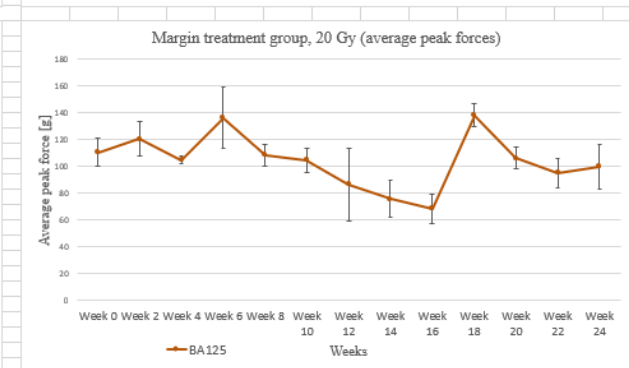
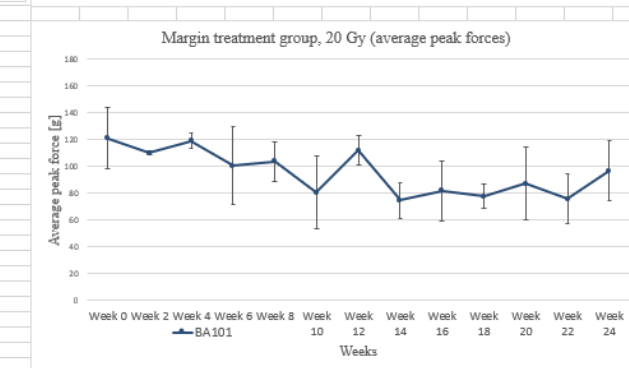
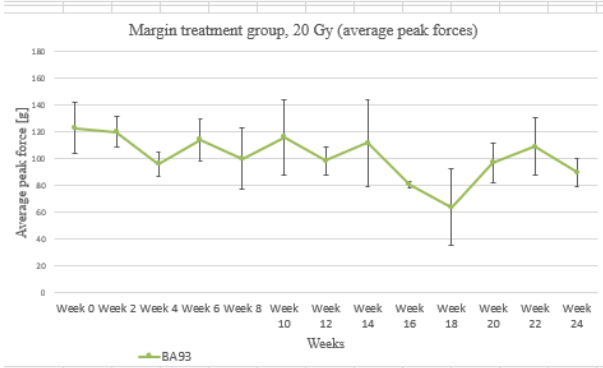
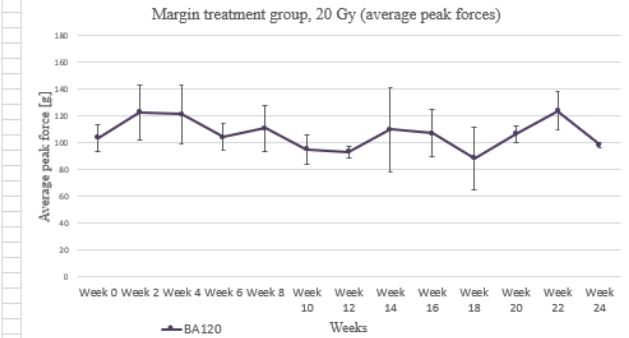
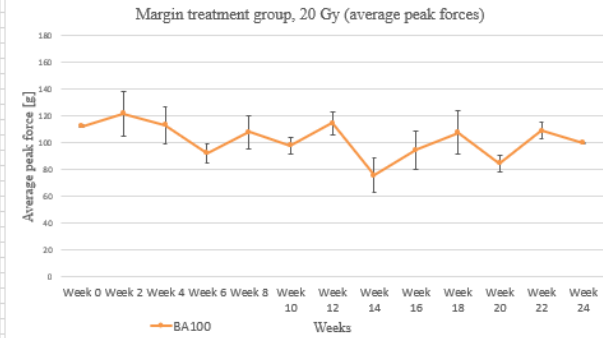
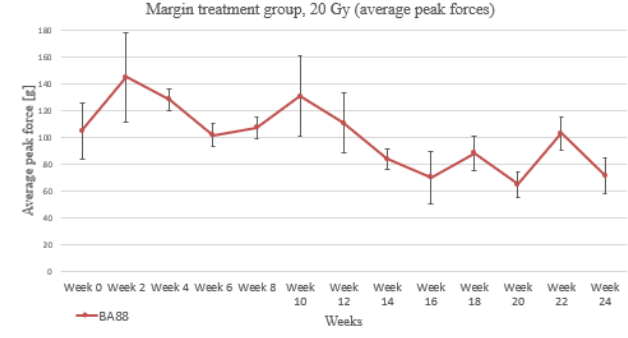
Supplementary Fig. 2A

Single mouse plots
0 Gy



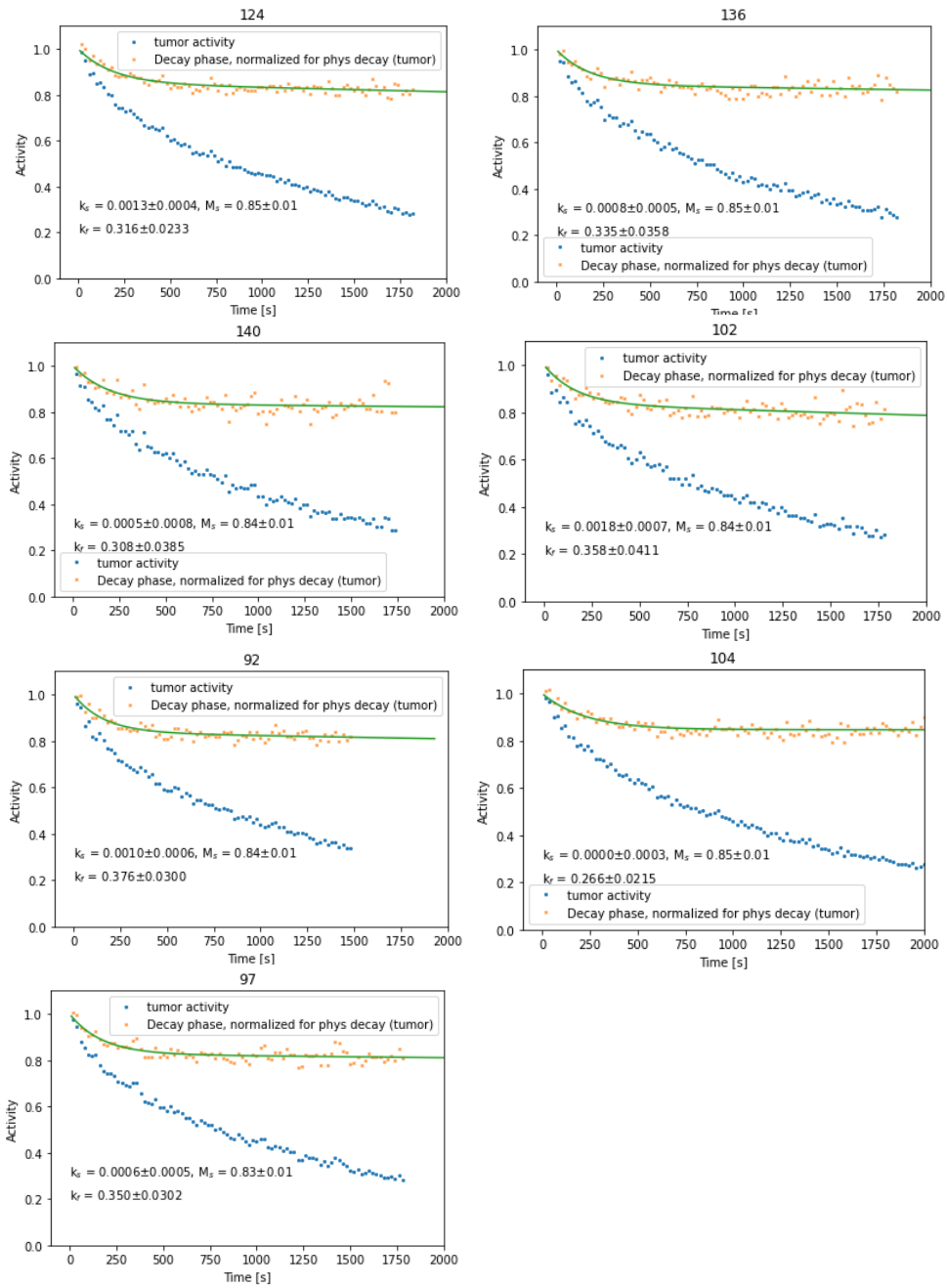
Supp. Fig. 2B

Single
mouse
plots
20 Gy

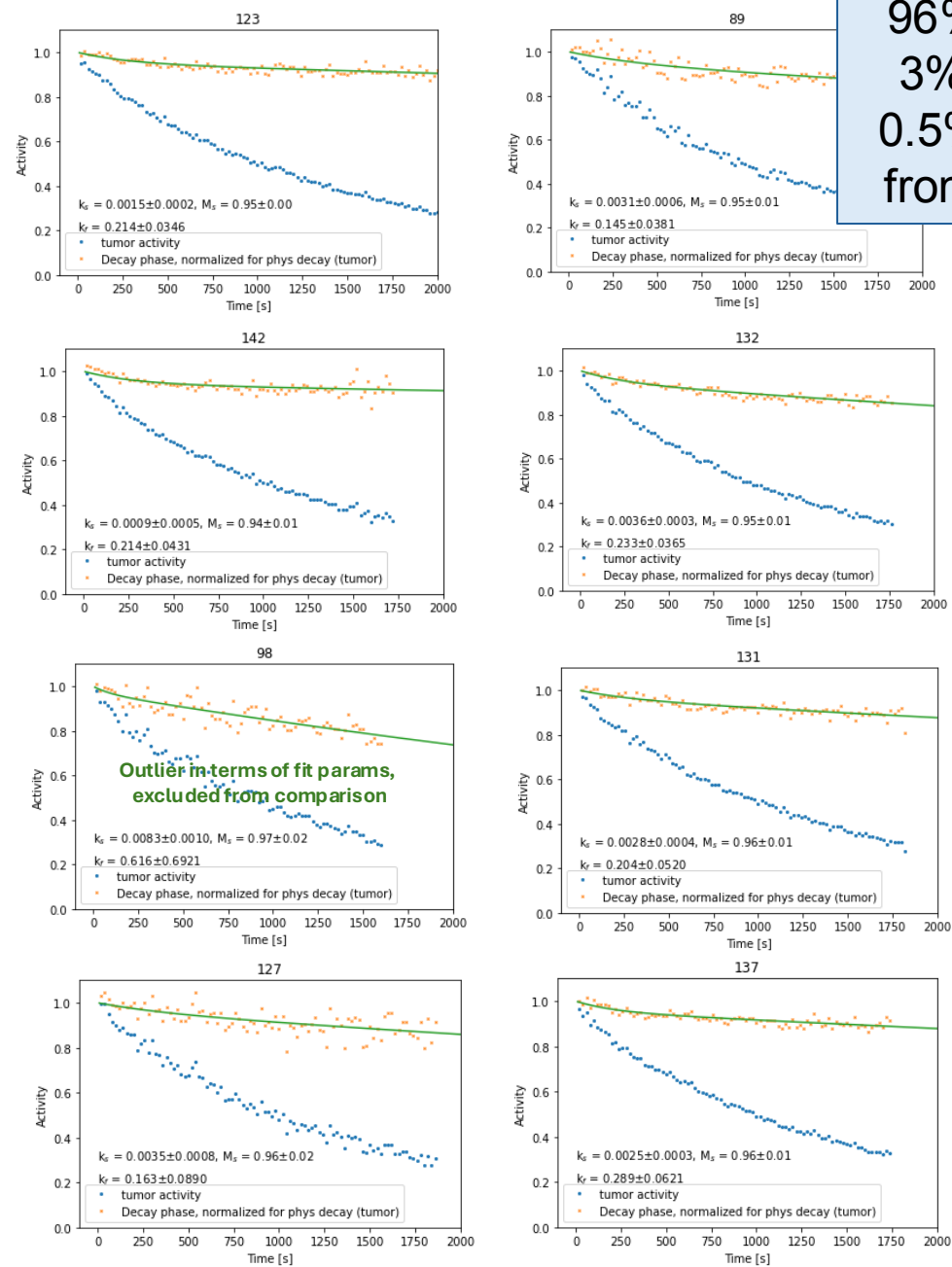


Supplementary Fig. 3

5 Gy, double-exp fit, $t_{\text{long}} = 400$ s



20 Gy, double-exp fit, $t_{\text{long}} = 400$ s



Assuming
 96% ^{11}C
 3% ^{10}C
 0.5% ^{15}O
 from MC